AD-A154 136

REPORT DOCUMENTATION PAGE		READ INSTRUCTIONS BEFORE COMPLETING FORM
1. REPORT NUMBER AFOSR-TR- 85-0388	2. GOVT ACCESSION NO.	3. RECIPIENT'S CATALOG NUMBER
4. TITLE (and Subtitle) Seismic Detection and Discrimination Using Ocean-Bottom Seismographs		5. TYPE OF REPORT & PERIOD COVERED Final Technical Report 10/1/81-9/30/83
		6. PERFORMING ORG. REPORT NUMBER
7. AUTHOR(s) J.A. Orcutt		8. CONTRACT OR GRANT NUMBER(s) F49620-79-C-0019
9. PERFORMING ORGANIZATION NAME AND ADDRESS University of California, San Diego Scripps Institution of Oceanography La Jolla, California 92093		10. PROGRAM ELEMENT, PROJECT, TASK AREA & WORK UNIT NUMBERS Program Element 61101E Program Code 9D60
11. CONTROLLING OFFICE NAME AND ADDRESS Advanced Research Projects Agency 1400 Wilson Blvd. Arlington, Virginia 22209		12. REPORT DATE Sep 83
		13. NUMBER OF PAGES
14. MONITORING AGENCY NAME & ADDRESS(if different from Controlling Office)		15. SECURITY CLASS. (of this report) UNCLASSIFIED
		15a. DECLASSIFICATION/DOWNGRADING SCHEDULE

16. DISTRIBUTION STATEMENT (of this Report)

Approved for public release;
distribution unlimited.

17. DISTRIBUTION STATEMENT (of the abstract entered in Block 20, if different from Report)

DTIC
ELECTE
MAY 24 1985
S   D
A

18. SUPPLEMENTARY NOTES

19. KEY WORDS (Continue on reverse side if necessary and identify by block number)
Marine Seismic System
Ocean Bottom Seismology
Seismic Noise

20. ABSTRACT (Continue on reverse side if necessary and identify by block number)
We have developed a model for the generation of seismic noise at the sea-floor which will enable us to extrapolate measurements made at the seafloor with ocean bottom seismographs to depths within the underlying sediment and basement. This physical model is consistent with seafloor noise measurements we have made at Scripps during the past decade and largely discounts the hypothesis that noise is generated at the seafloor by current motion inducing instrument "rocking" through mechanisms such as vortex shedding. We have never been able to demonstrate a correlation between bottom currents and seismic

DD FORM 1473 EDITION OF 1 NOV 65 IS OBSOLETE
1 JAN 73
S/N 0102-LF-014-6601

DTIC FILE COPY

85 4 23 005

UNCLASSIFIED

noise on the seafloor, or in finely controlled experiments such as the Lopez Island intercomparison test. However, there is a definite correlation between seafloor noise and the general weather in the vicinity of the seismographs. Ambient seismic noise at depths in the oceanic crust is characterized using data from a DARPA-sponsored experiment using the Marine Seismic System (MSS), a vertical-component, digitally-recording, short-period seismograph system which was part of the borehole instrumentation of Deep Sea Drilling Project 78B. The instrument package rested unclamped in Hole 395A, 517 meters within basement rock. Reliable estimates of microseismic noise levels were obtained between 0.16 and 2.2 Hz, instrument noise dominated outside of this band. The observed microseismic noise was quasi-stationary on the time scale of one hour, but not ten. Although spectral shapes were stable, noise amplitudes grew with time over the 26-hour observation period by 3-5 dB. The borehole noise levels increased concurrently with local swell height, suggesting a causal relationship. An estimation of displacement power densities obtained early in the experiment had a peak value of $4 \times 10^6 nm^2/Hz$ at 0.21 Hz, and decreased at 80 dB/decade from $1 \times 10^6 nm^2/Hz$ at 0.33 Hz to 1 nm^2/Hz at 1.9 Hz. Noise levels observed at the seafloor near Site 395A were greater than those observed in the borehole by a factor which increased with frequency from 10dB at 0.2 Hz to 28dB at 2 Hz. This is consistent with noise propagating as a fundamental-mode Stoneley wave trapped near the ocean bottom-seafloor interface. If the relationship observed between noise at and below the seafloor during Leg 78B is a general one, the range of ocean bottom noise levels implies that borehole noise levels could approach those at quiet continental sites.

Accession For

NTIS GRA&I	☑	
DTIC TAB	☐	
Unannounced	☐	
Justification		

By

Distribution/

Availability Codes

Dist	Avail and/or Special
A1	

DTIC COPY INSPECTED 3

UNCLASSIFIED

<u>FINAL TECHNICAL REPORT</u>

1 October 1981 - 30 September 1983

ARPA Order: 3291-21

Program Code: 9D60

Contractor: The Regents of the University of California
                           University of California, San Diego
                           Scripps Institution of Oceanography
                           La Jolla, California 92093

Effective Date: 1 October 1981

Expiration Date: 30 September 1983

Amount of Contract: $188,075

Contract Number: F49620-79-C-0019

Principal Investigators: John A. Orcutt (619) 452-2887
                           Thomas H. Jordan (617) 253-3589

Program Manager: Dr. Henry Radoski

Title: Seismic Detection and Discrimination Using
                           Ocean Bottom Seismographs

Sponsored by: Advanced Research Projects Agency (DOD)
                           ARPA Order No. 3291-21

Monitored by: AFOSR under contract #F49620-79-C-0019

Sponsored by
Advanced Research Projects Agency (DOD)
ARPA Order No. 3291-21
Monitored by AFOSR under Contract # F49620-79-C-0019

CHAPTER I

MODELING SEA-FLOOR SEISMIC NOISE

JOHN A. ORCUTT
RICHARD G. ADAIR
THOMAS H. JORDAN

I.1. Introduction

We have developed a model for the generation of seismic noise at the sea floor which will enable us to extrapolate measurements made at the sea floor with ocean bottom seismographs to depths within the underlying sediment and basement. This physical model is consistent with sea floor noise measurements we have made at Scripps during the past decade and largely discounts the hypothesis that noise is generated at the sea floor by current motion inducing instrument "rocking" through mechanisms such as vortex shedding. We have never been able to demonstrate a correlation between bottom currents and seismic noise on the sea floor or in finely controlled experiments such as the Lopez Island intercomparison test. However, there is a definite correlation between sea floor noise and the general weather in the vicinity of the seismographs. Details of these measurements and experiments are contained in previous Annual and Semi-Annual Technical Reports.

I.2. Power Spectra of Seafloor Noise

The basic assumptions involved in the model are:

(1) Horizontal stratification. To simplify the mathematics involved in the model we consider only the 2-D case, where field variables can generally depend on (r,z,t); the earth structure depends only on z, however.

(2) Noise sources are confined to the water column. The existing data are consistent with the hypothesis that the primary sources of seismic noise on the sea floor are hydrographic disturbances in the water column. We formalize this hypothesis by imposing on the noise model an (unknown) distribution of vertical point loads, $f(r,t)$, at the sediment-water interface (Figure 1). Later, in the fully three-dimensional calculations, we shall let f depend on both r and θ, the azimuth. If we let $p(r,z,t)$ be the incremental pressure field in the water column $(z \leqslant 0)$ and $r(z,z,t)$ be the stress tensor, then the (inhomogeneous) boundary conditions to be applied at $z = 0$ are $r_{zz}(r,0,t) = f(r,t) = -p(r,0,t)$ and $r_{rz}(r,0,t) = 0$. These boundary conditions have the desirable effect of decoupling the problem of noise in

the ocean from noise in the solid medium by the specification of $f(r,t)$. The assumption that noise sources are confined to the water column also fixes the radiation condition for large z to be that of downgoing waves only. In our model this condition is imposed in the half-space underlying the layered stack representing crustal stratification (Figure 1).

(3) The noise field is stationary in time and space and isotropic in horizontal coordinates. In the 2-D problem discussed here this implies that its autocorrelation function depends only on the temporal and spatial lag variables:

$$C_{ff}(r,t) = \; < f(r_o,t_o)f(\mid r+r_o \mid, t+t_o)>$$

$$= \int_{-\infty}^{\infty} dt_o \int_0^{2\pi} d\phi_o \int_0^{\infty} r_o \, dr_o \, f(r_o,t_o), \, f(\mid r+r_o \mid, t+t_o) \qquad (2.1)$$

where $r = \mid r \mid$, $r_o = \mid r_o \mid$, $r \cdot r_o = rr_o \cos\phi_o$, and the brackets $< >$ denote an ensemble average.

These assumptions allow a precise formulation of the inverse problem for C_{ff} given both seismic and acoustic noise observations on the sea floor; they also allow a precise formulation of the problem of predicting the noise field at depth.

Let $u(r,z,t)$ be the vector-valued displacement field at some position $z \geqslant 0$, and let $G(\mid r-r_o \mid, z, t-t_o)$ be the displacement response at (x,y,z,t) to a vertical point load at $(x_o,y_o,0,t_o)$, where $r^2 = x^2+y^2$ and $r_o^2 = x_o^2 + y_o^2$. Then we have

$$U(r,z,t) = G(\mid r-r_o \mid, z, t-t_o) * f(r,t) \qquad (2.2)$$

where the asterisk denotes convolution in both time and horizontal space. Because the source field is presumed to be stationary and isotropic and G depends only on horizontal and temporal coordinate differences, the tensor-valued autocorrelation function for U also depends only on the lag variables:

$$C_{uu}(r,z,t) = \; < U(r_o,z,t_o)U^T(\mid r+r_o \mid, z, t+t_o)> \qquad (2.3)$$

Since f, u and G are all axisymmetric, it can be shown (see Appendix A1.1) that equation (2.3) is equivalent to:

$$C_{uu}(r,z,t) = \Gamma(r,z,t) * C_{ff}(r,t) \qquad (2.4)$$

where Γ is the tensor-valued autocorrelation function for G:

$$\Gamma(r,z,t) = \int_{-\infty}^{\infty} dt_o \int_{0}^{2\pi} d\phi_o \int_{0}^{\infty} r_o\, dr_o\, \mathrm{G}(r_o,z,t) \mathrm{G}^T(|\,r_o+r\,|\,,z,t_o+t) \qquad (2.5)$$

If the Fourier-Bessel transform pair $h(r,t)$ and $h(k,\omega)$ is defined by:

$$h(k,\omega) = \int_{-\infty}^{\infty} dt\ e^{i\omega t} \int_{0}^{\infty} rdr J_o(kr) h(r,t) \qquad (2.6a)$$

$$h(r,t) = \frac{1}{2\pi} \int_{-\infty}^{\infty} d\omega\, e^{-i\omega t} \int_{0}^{\infty} kdk J_o(kr) h(k,\omega) \qquad (2.6b)$$

then the transformation of C_{uu} can be written (see Appendix A1.3) as:

$$C_{uu}(k,z,\omega) = 2\pi\, \Gamma(k,z,\omega) C_{ff}(k,\omega) \qquad (2.7)$$

where $\Gamma(k,z,\omega)$ and $C_{ff}(k,\omega)$ denote the Fourier-Bessel transforms of $\Gamma(r,z,t)$ and $C_{ff}(r,t)$, respectively.

A special case of $C_{uu}(r,\omega)$ is the vertical component power spectrum $P_z(\omega)$, which is the zz-component of $C_{uu}(r,\omega)$ at $r = 0$. We have:

$$P_z(\omega) = 2\pi \int_{0}^{\infty} kdk\, \Gamma_{zz}(k,z,\omega) C_{ff}(k,\omega)$$

$$= 2\pi \int_{0}^{\infty} kdk\ |\, G_z(k,z,\omega)\,|^2 C_{ff}(k,\omega)\ , \qquad (2.8)$$

since the zz component of $\Gamma(k,z,\omega)$ is $G_z^{\dagger}(k,\omega) G_z(k,\omega)$ (see Appendix A1.3).

The spatial variation of C_{ff} is poorly constrained; a simply parameterized form is

$$C_{ff}(r,\omega) = C_{ff}^0(\omega) e^{-K^2(\omega)r^2} \qquad (2.9)$$

where $C_{ff}^0(\omega) = C_{ff}(o,\omega)$ and $K^2(\omega)$ depend on frequency; such a function is frequently used in studying wave propagation through inhomogeneous, random media (Aki and Richards, 1980, p. 741). The Bessel transform of $e^{-K^2 r^2}$ is $\frac{1}{2K^2} e^{-k^2/4K^2}$, so that for such a C_{ff}, the vertical power spectrum is

$$P_z(\omega) = 2\pi\, C_{ff}^0(\omega) \left[\frac{1}{2K^2(\omega)} \int_{0}^{\infty} kdk\ |\, G_z(k,z,\omega)\,|^2 e^{-k^2/4K^2(\omega)} \right] \qquad (2.10)$$

$G_z(k,z,\omega)$ can be computed for a given crustal model using the method outlined in the next section and $P_z(\omega)$ can be measured at the sea floor, $z = 0$; $C_{ff}^0(\omega)$ can then be estimated if reasonable values of $K(\omega)$, the correlation wavenumber, are used. Given this, the noise spectrum at depth $z > 0$ can be predicted.

I.3. Green's Functions

The viscoelastic Green's functions necessary for the correlation calculations are computed for an earth model consisting of a stack of homogeneous layers including a fluid ocean as the uppermost layer. The problem for a point force in a flat earth suggests the use of cylindrical coordinates. In such a system, the displacements can be expanded in terms of vector cylindrical harmonics:

$$V(r,\theta,z,t) = \frac{1}{2\pi}\int_{-\infty}^{\infty}d\omega\, e^{-i\omega t}\sum_m\int_0^{\infty}kdk\Big[U_z(k,z,\omega)\mathbf{R}_k^m$$
$$+\, U_r(k,z,\omega)\mathbf{S}_k^m + U_\theta(k,z,\omega)\mathbf{T}_k^m\Big] \tag{3.1}$$

where r, θ and z are cylindrical coordinates and $\mathbf{R}_k^m$, $\mathbf{S}_k^m$ and $\mathbf{T}_k^m$ are defined:

$$Y_k^m = J_m(kr)e^{im\theta},\ m = 0, \pm 1, \pm 2, \cdots$$

$$\mathbf{R}_k^m(r,\theta) = Y_k^m\hat{e}_z$$

$$\mathbf{S}_k^m(r,\theta) = \frac{1}{k}\frac{\partial Y_k^m}{\partial r}\,\hat{e}_r + \frac{1}{kr}\frac{\partial Y_k^m}{\partial \theta}\,\hat{e}_\theta$$

$$\mathbf{T}_k^m(r,\theta) + \frac{1}{kr}\frac{\partial Y_k^m}{\partial \theta}\,\hat{e}_r - \frac{1}{k}\frac{\partial Y_k^m}{\partial r}\,\hat{e}_\theta \tag{3.2}$$

where $\hat{e}_z$, $\hat{e}_r$ and $\hat{e}_\theta$ are unit vectors in the z, r and θ directions (Takeuchi and Saito, 1972). For a vertical point force the problem is axisymmetric and $m = 0$. The vertical displacement at r, θ and z in equation (3.1) reduces to:

$$U_z(r,\theta,z,\omega) = \int_0^{\infty}kdk\,U_z(k,z,\omega)J_o(kr) \tag{3.3}$$

In performing the numerical computations, we find it convenient to change the variable of integration to horizontal slowness or ray parameter p; $k = \omega p$:

$$U_z(r,\theta,z,\omega) = \omega^2 \int_0^\infty pdp\, U_z(p,z,\omega) J_o(\omega pr)$$

The physical model used in our computations is shown in Figure 1. In this case an ocean overlies a sequence of viscoelastic layers which are, in turn, underlain by a homogeneous half space. Boundary conditions for the solution include a traction-free boundary at the free surface, continuity of traction and displacement between solid layers, continuity of τ_{zz} and U_z at the fluid-solid boundary and a requirement that waves in the half space satisfy the radiation conditions. These conditions simply require that only downward propagating waves exist in the half-space. The vertical force at the sea floor can be thought of as an inhomogeneous boundary condition producing a jump in τ_{zz} at the ocean bottom. In the solid layers the user is required to specify the compressional and shear velocities, the density and compressional and shear Q's. In the fluid, of course, only the acoustic velocity, density and compressional Q can be specified.

We compute the vertical response of this stack, $U_z(p,z,\omega)$, with a technique which combines phase-related reflection and transmission coefficients in an iterative fashion (Apsel, 1978). The method is essentially identical to the work published by Kennett and Kerry (1979) and Kennett (1980). The fundamental advantage of this approach is the achievement of numerical stability at high frequencies and wavenumbers.

We have chosen a suite of four simple models to represent the structure in the northwest Pacific near the proposed MSS sites. The physical properties for the site, see Table I, were taken from the Initial Reports of the Deep Sea Drilling Project for Leg 32, holes 303 and 304 in the northwest Pacific (Figure 2). The models encompass the range of sediment thickness and types noted in the Naval Ocean Research and Development Activity environmental report for the Marine Seismic System (MSS). The models consist of approximately 5.5 km of ocean overlying diatom radiolarian ooze with very low rigidity. This layer, 250-400 meters in thickness, overlies either a hundred-meter thick, rigid chert layer or oceanic, basaltic basement.

$| U_z(p,z,\omega) |$ for a 400-meter sedimentary layer overlying basement is illustrated in Figure 3 with frequency increasing from the background into the foreground and horizontal slowness

increasing from left to right across the foreground. Figure 4 is a blowup of the bracketed section of Figure 3. The dominant pulse in the frequency-slowness spectra corresponds to the fundamental Stoneley or interface wave and, at high frequency, has a slowness slightly greater than $1/0.2 = 5$ s km^{-1}. At low frequencies the Stoneley wave begins to sense the underlying chert and basement and the slowness of the fundamental decreases (phase velocity increases); that is, the mode is normally dispersed. We note, in addition, that at this "knee" below 1 Hz in the fundamental dispersion curve, the amplitudes of the Stoneley wave decrease rapidly as the wave enters increasingly rigid media. At small slownesses or high phase velocities small ridges correspond to the propagation of P and S body waves and leaky modes. In Figure 4, a small ridge at a slowness of 0.25 s km^{-1} corresponds to the compressional head wave propagating along the basement interface. In the low frequency detail plot in Figure 4, we see the fundamental Stoneley wave approaches the shear wave slowness in the rock $(1/2.31 = 0.433$ s km$^{-1})$.

We have found the vertical wavefunctions, $U_z(p,z,\omega)$, for various propagation modes to be very useful in studying the effects of burial of the MSS seismometer. A model for thick sediments including a chert layer overlying basement is shown in Figure 5. The symbols indicate the receiver burial depths at which we shall calculate amplitude spectra. A vertical wavefunction, that is $| U_z(p,z,\omega) |$ as a function of depth, for the fundamental Stoneley mode branch is shown in Figure 6 for a horizontal slowness of 4.5 s km^{-1} and a frequency of 0.2 Hz. The maximum displacement occurs at the sea floor where a discontinuity marks the source depth. The wavefunction decays exponentially into the overlying water and into the underlying chert and basement. The mode of propagation within the water column is, of course, purely acoustical. For this particular important mode of propagation, the effect of burial is clearly to rapidly reduce vertical displacement and, by implication, seismic noise. Figure 7 is a vertical wavefunction for the first overtone of the fundamental Stoneley wave at a frequency of 1 Hz and a horizontal slowness of 4 s km^{-1}. In this case there are two oscillations within the sediment and exponential decay into the overlying chert and basement. In this case, the amplitude of this mode is actually larger toward the bottom of the sediments, but, because of the position of the source, the mode is

not a significant contributor to the propagation of sea floor seismic noise. This is easily seen in Figure 3 where the fundamental mode clearly dominates any of the overtones.

We have studied the effect of burial depth at all frequencies for all propagation modes by performing the zero-order Hankel Transform in equation 3. The complete frequency-slowness spectrum is transformed to yield frequency-distance spectra such as the one shown in Figure 8 for a range of 10 km. The squares correspond to a receiver at the sea floor or a depth of 5.4 km, the triangles are 200 meters into the sediment, the diamonds are 50 meters into the chert, the +'s 50 meters into the basalt and finally the X's are 200 meters into the basalt. These depths are shown graphically on the model in Figure 5. For this particular case, the broad peak associated with the fundamental Stoneley mode propagation disappears as the depth of burial increases from within the sedimentary column to within the crystalline basement. Generally, the vertical amplitudes decrease monotonically with burial depth except for frequencies in excess of 1-2 Hz where the pattern is more variable. The most dramatic effect of burial depth is to remove the broad Stoneley peak when the receivers enter the more rigid chert layer. However, we are reluctant to advocate burying the MSS instrument in chert as a solution to the noise problem. We have modeled the chert as a homogeneous, fairly rigid sedimentary layer. In fact, the chert exists as flat-lying, platy deposits within a less rigid sedimentary matrix. That is, the chert layer is most properly modeled as a composite medium in which the rigidity of the composite may vary rapidly in both horizontal and vertical directions. Furthermore, chert is extremely difficult to drill and may prevent penetration to depths necessary to provide "shielding" from the large amplitude, overlying sedimentary Stoneley waves.

We have conducted an exhaustive search of the characteristics of wave propagation in the four representative models in Table I with a vertical point force at the sea floor as a source. Figures 9-35 are amplitude spectra for various combinations of models at different source-receiver separations and receiver depths. The figures are quite consistent although many of the major conclusions can be illustrated by an examination of a few of the figures. Figure 9 shows amplitude spectra for thick and thin sediments (400 and 250 m respectively) each with a hundred-meter

thick chert layer below the sediment and above the basement. We have chosen a range of 10 km in this case and the receivers are at the sea floor and buried 50 meters into the chert. We see the effect of burial noted before in the discussion of Figure 8. That is, burial of the receiver generally removes the broad peak between 0.1 and 2 Hz. In this figure we note the peak occurs at lower frequencies and is greater in breadth for thick sediments as compared to the thin sediments. This is certainly reasonable since the fundamental Stoneley mode vertical wavefunction will begin to sense the rigid chert and basement at higher frequencies in the case of the thin sediments.

Figure 20 is computed for the same pair of models except the deep receiver, in this case, is 200 meters into the basalt. Again the broad Stoneley wave peak disappears with burial in the rigid media below the sediments. We note, interestingly, there is little difference in the spectra for the two receivers buried within the basement. We might expect, therefore, that the thickness of the unconsolidated sediment or ooze should play no appreciable role in the selection of a drilling site if we are considering the seismic noise problem alone. The would not be true of an OBS experiment in which the thinner sediments might be preferred in order to reduce the breadth of the Stoneley peak.

Figure 28 shows the effect of source-receiver separation on the point force amplitude spectra. The models are, again, identical to those already discussed and the receivers are at the sea floor. As the range increases in this case from 10 to 1100 km the Stoneley peak disappears and the overall amplitude drops by more than 2 decades. We have used a fairly low Q for the sediments which inevitably leads to the loss of the sedimentary Stoneley waves as propagation distance increases. Geometrical spreading alone would decrease amplitudes, but not distort the shape so severely as we see here. Unfortunately, we know very little of the shear Q in sea floor sediments and the predictions of these models must be studied with this difficulty in mind. Certainly, low group velocity (0.6 km s^{-1}) sedimentary Stoneley waves have been observed over distances of 1000 km on the sea floor (Okal and Talandier, 1980). Further research on this phenomenon is absolutely necessary and will be considered in detail in our future work.

Finally, in Figure 13 we see the effect of the chert layer in this problem. The sedimentary layer is 250 m in thickness and the receivers are at the sea floor and 50 m below the unconsolidated sediments. Very clearly, the presence or absence of chert in the bottom of the sedimentary section makes little difference in the propagation problem.

I.4. CONCLUSIONS

We have completed a thorough examination of the Green's functions used to propagate noise in our ocean bottom seismic noise model. Almost certainly, the fundamental model Stoneley wave is responsible for transport of the bulk of seismic noise energy. We can make a number of recommendations at this point with respect to the siting of the MSS system.

1) The thickness of the sedimentary layer is not important in site selection with the understanding the instrument will be installed within the oceanic basement.

2) The presence or absence of a thin chert layer does not play a large role in the noise levels we expect to see at a buried receiver. However, as noted in the text, even though the fundamental Stoneley wave is severely attenuated in the chert, we do not recommend siting at a location over smooth bottom where chert is likely to be present. The drilling ship, certainly, will have an unpredictable amount of difficulty in penetrating the chert layer.

3) Burial of the seismic sensor in the basement will likely reduce seismic noise as observed at the sea floor in the microseism band, 0.1-2 Hz, by as much as 3 decades in displacement and 6 decades (60 db) in power.

4) Because surface weather controls the forcing of microseismic noise, the sensor should be sited in an area with weather as mild as possible.

We must also mention some precautions:

1) A lack of understanding of the shear Q could affect these results somewhat. However, because the role of the sedimentary Stoneley waves is fairly unimportant if the sensor is buried in the basement, we don't expect the effect to be large.

Table I. Model Parameters

MODEL I:

Description	V_p	Vs	Thickness	Density	Q_p	Q_J
Ocean	1.5	0.	5.4	1.0	10,000	0
Ooze	1.63	0.2	0.4	1.3	200	50
Chert	2.7	1.56	0.1	2.24	200	50
Basement	4.0	2.31	∞	2.5	300	150

MODEL II

Ocean	1.5	0.	5.4	1.0	10,000	0
Ooze	1.63	0.2	0.25	1.3	200	50
Chert	2.7	1.56	0.1	2.24	200	50
Basement	4.0	2.31	∞	2.5	300	150

MODEL III:

Ocean	1.5	0.	5.4	1.0	10,000	0
Ooze	1.63	0.2	0.4	1.3	200	50
Basement	4.0	2.31	∞	2.5	300	150

MODEL IV:

Ocean	1.5	0.	5.4	1.0	10,000	0
Ooze	1.63	0.2	0.25	1.3	200	50
Basement	4.0	2.31	∞	2.5	300	150
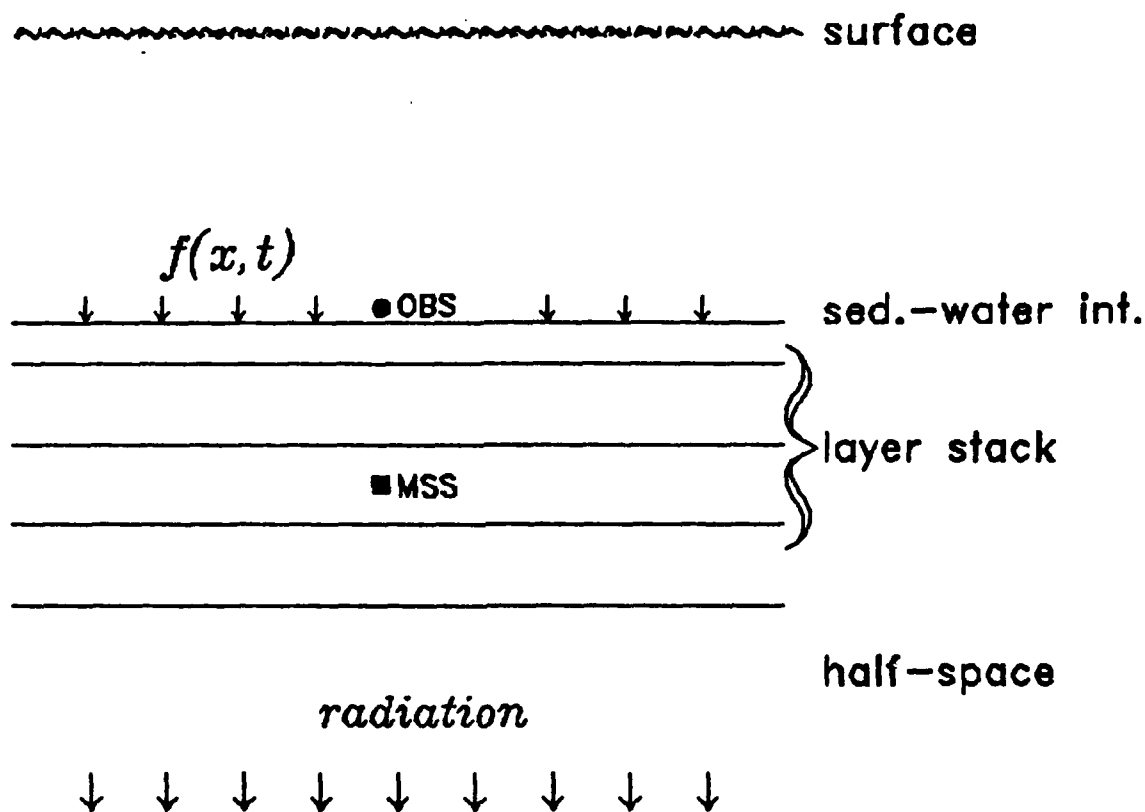
Figure 1. An illustration depicting some of the assumptions we propose to use in formulating a hypothetical noise model. Noise sources within the water column are represented by the vertical load distribution they impose on the sea floor, $f(x,t)$. In the half-space, only downgoing waves are allowed. The problem is, given observations of seismic and acoustical noise on the sea floor recorded by an OBS, to predict the noise spectrum at a proposed MSS site at depth.
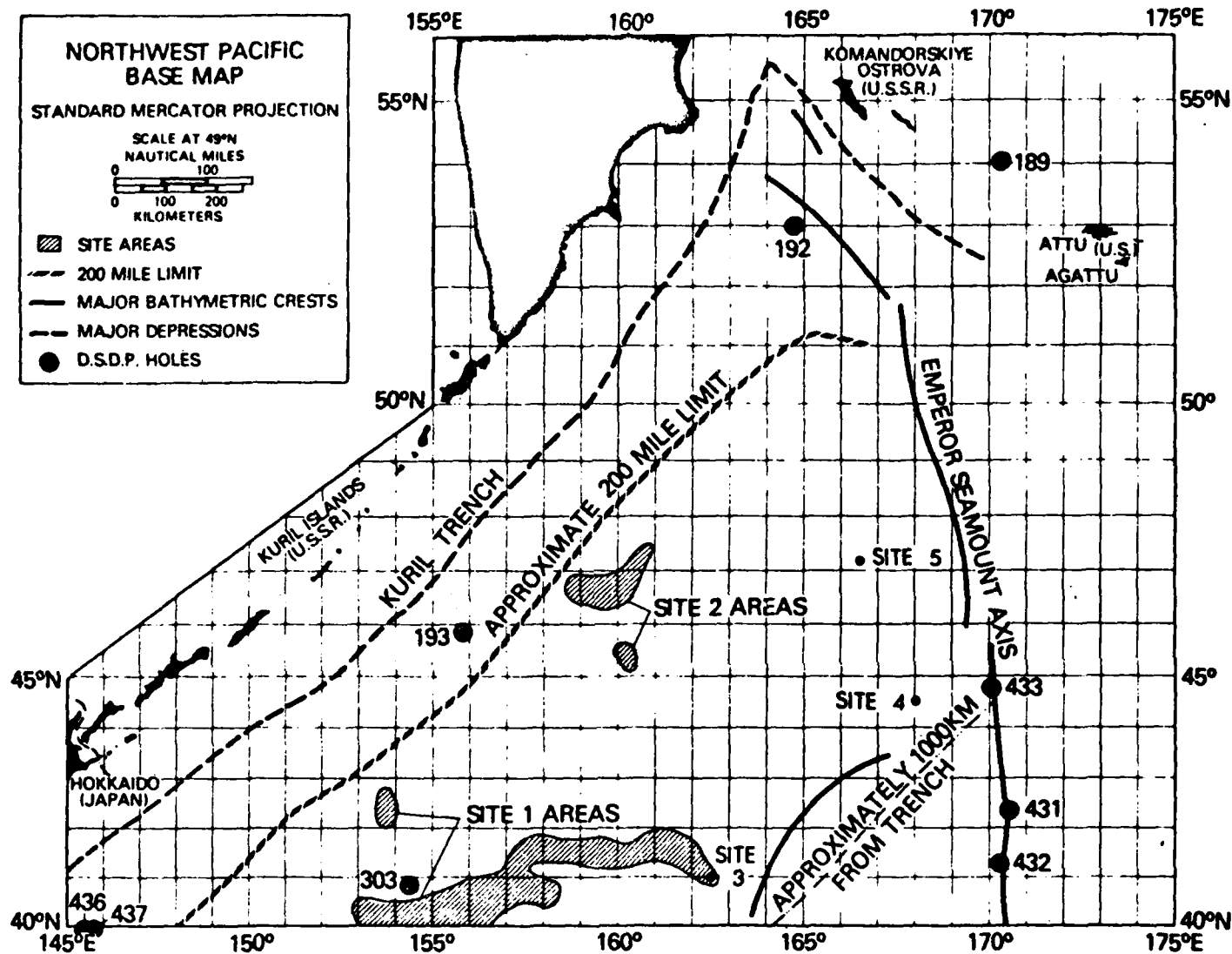
Figure 2. Chart of northwest Pacific and contiguous masses showing proposed Sites 1 and 2 for MSS emplacement. Sedimentary thicknesses are greater at Site 2 although the presence of chert is not as ubiquitous as at Site 1. The weather is generally better at Site 2 although wave heights, an important consideration for seismic noise, are generally quite large year around in this part of the Pacific.

TRANSFORMED VERTICAL DISPLACEMENT DUE TO A VERTICAL POINT FORCE
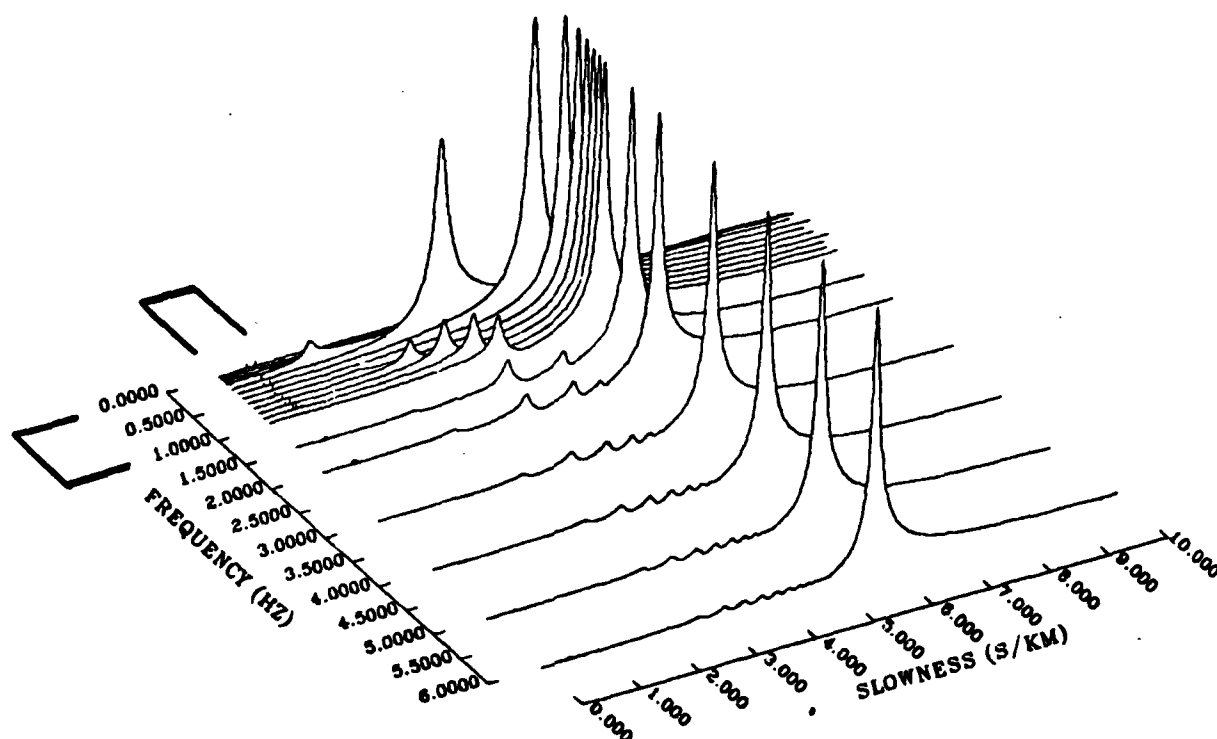
SOURCE AND RECEIVER AT THE SEDIMENT−WATER INTERFACE

Figure 3. Frequency vs. horizontal slowness for vertical displacement at the sea floor due to a vertical point force at that depth. The function depicted is, in fact, the modulus of the complex vertical displacement.

TRANSFORMED VERTICAL DISPLACEMENT DUE TO A VERTICAL POINT FORCE
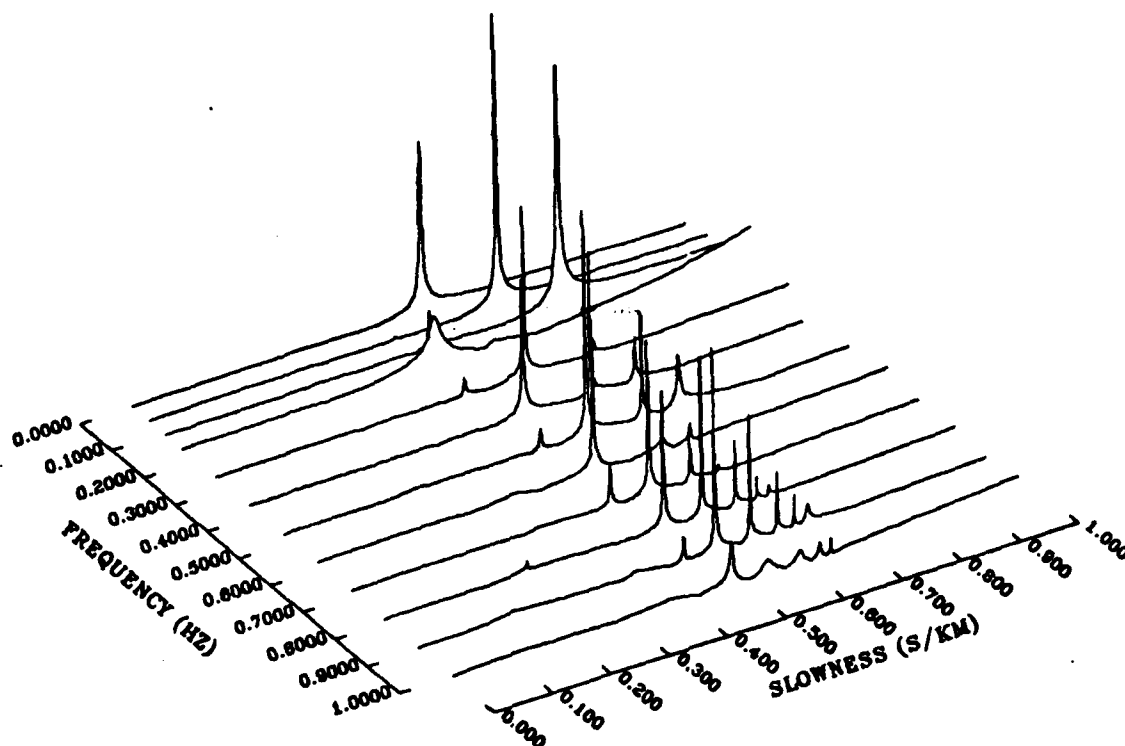
SOURCE AND RECEIVER AT THE SEDIMENT-WATER INTERFACE

Figure 4. Blowup of low frequency, low horizontal slowness for the modulus of vertical displacement at the sea floor due to a vertical point force at that depth. The area of this plot corresponds to the area of the brackets in Figure 3.
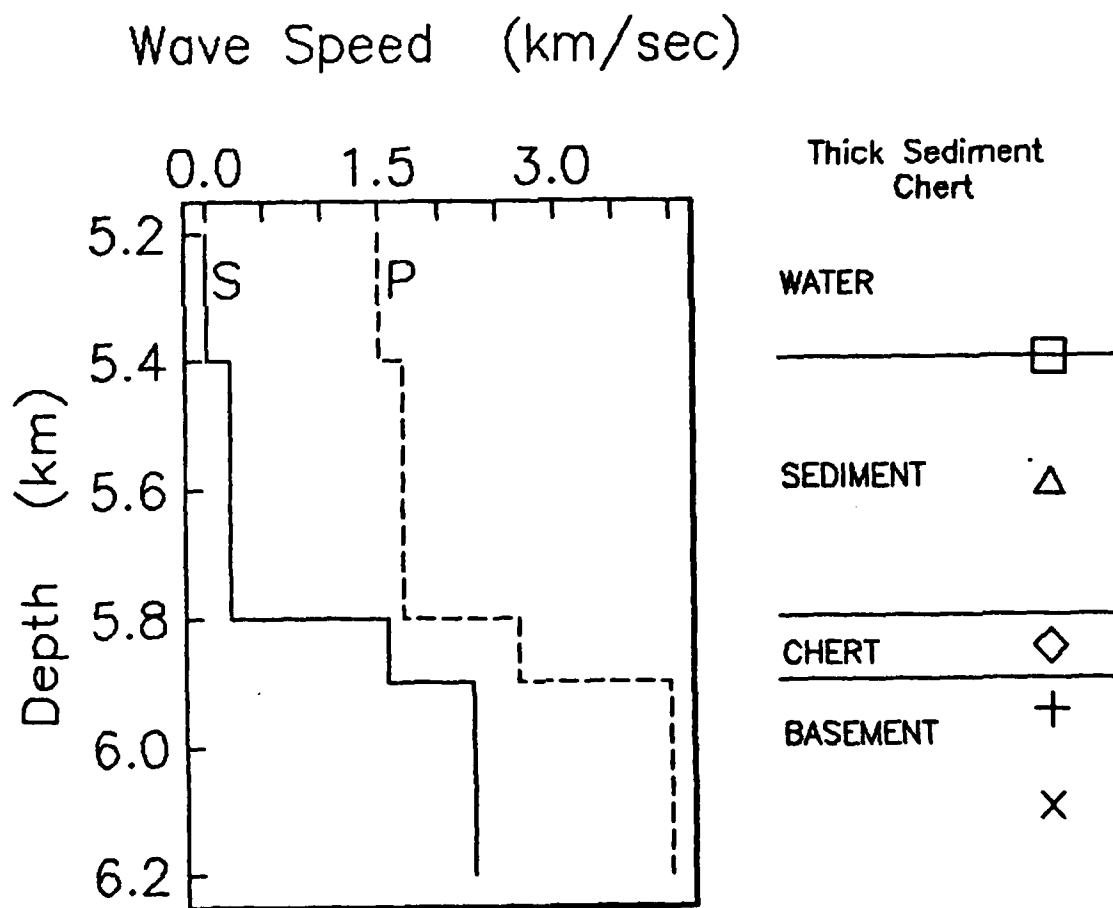
Figure 5. Compressional (dashed line) and shear velocity (solid line) structure for a typical MSS site. 400 meters of ooze with very low rigidity (shear velocity = 200 ms^{-1}) overlies 100 meters of fairly competent, high-velocity chert. The chert, finally, overlies ocean basement rocks with a compressional velocity of 4 km s^{-1}. The density of ooze is only slightly greater than that of the overlying ocean. The arrows and symbols denote receiver depths for which vertical displacement amplitude spectra were computed (see Figure 8) for a source at the sea floor.

Vertical point force at sea floor. Freq=0.2 hz Slow=4.5 sec/km
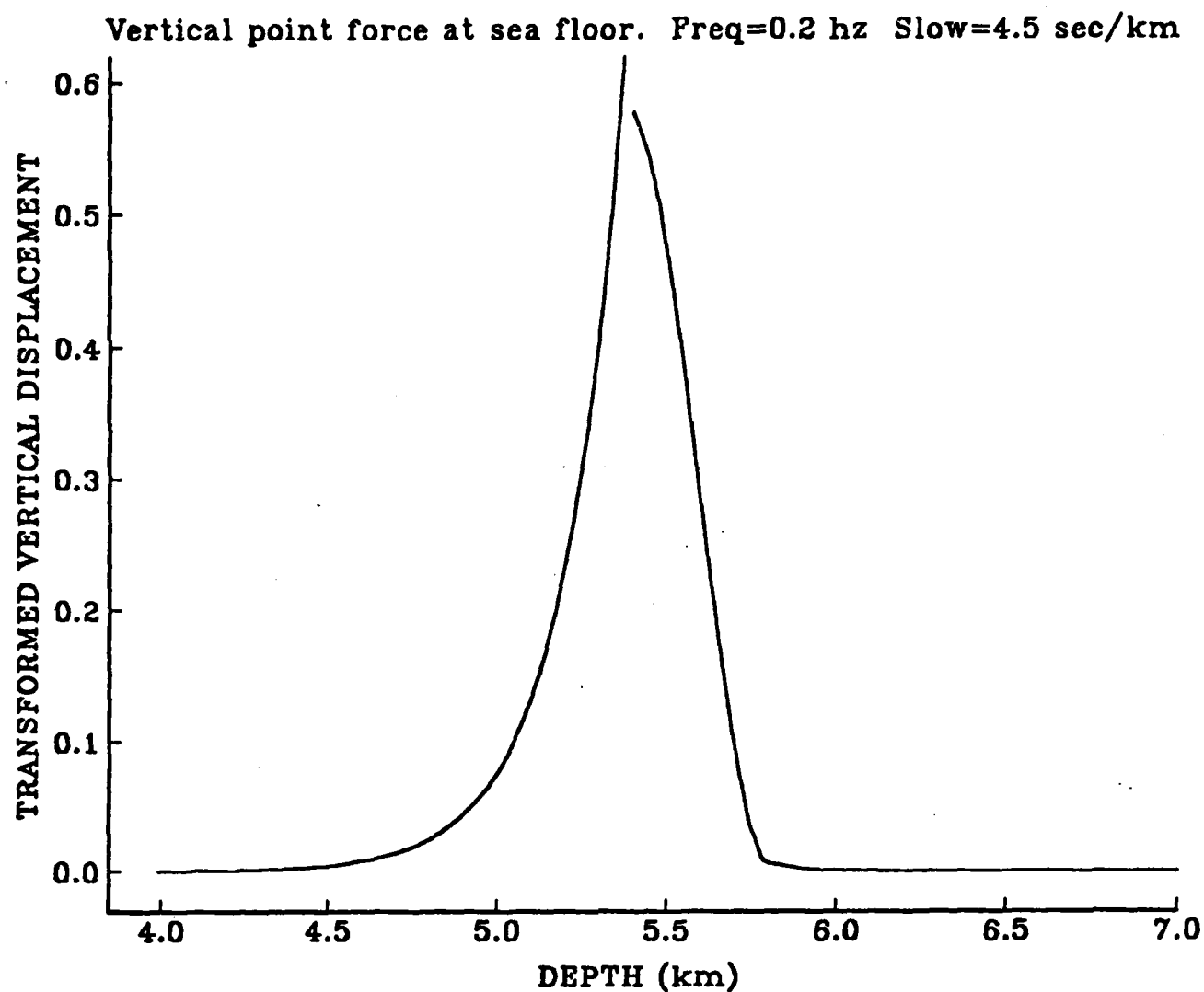
Figure 6. $| U_r(p, \omega, z) |$ plotted versus depth for a frequency of 0.2 Hz and a horizontal slowness of 4.5 s km^{-1}. This point in Figure 3 corresponds to the fundamental Stoneley mode. The discontinuity at a depth of 5.4 km is due to the presence of the source at the sea floor.

FIRST HIGHER STONELEY MODE

VERTICAL POINT FORCE AT WATER–SEDIMENT INTERFACE. FREQ=1.0 hz,SLWNS=4.0 sec/km
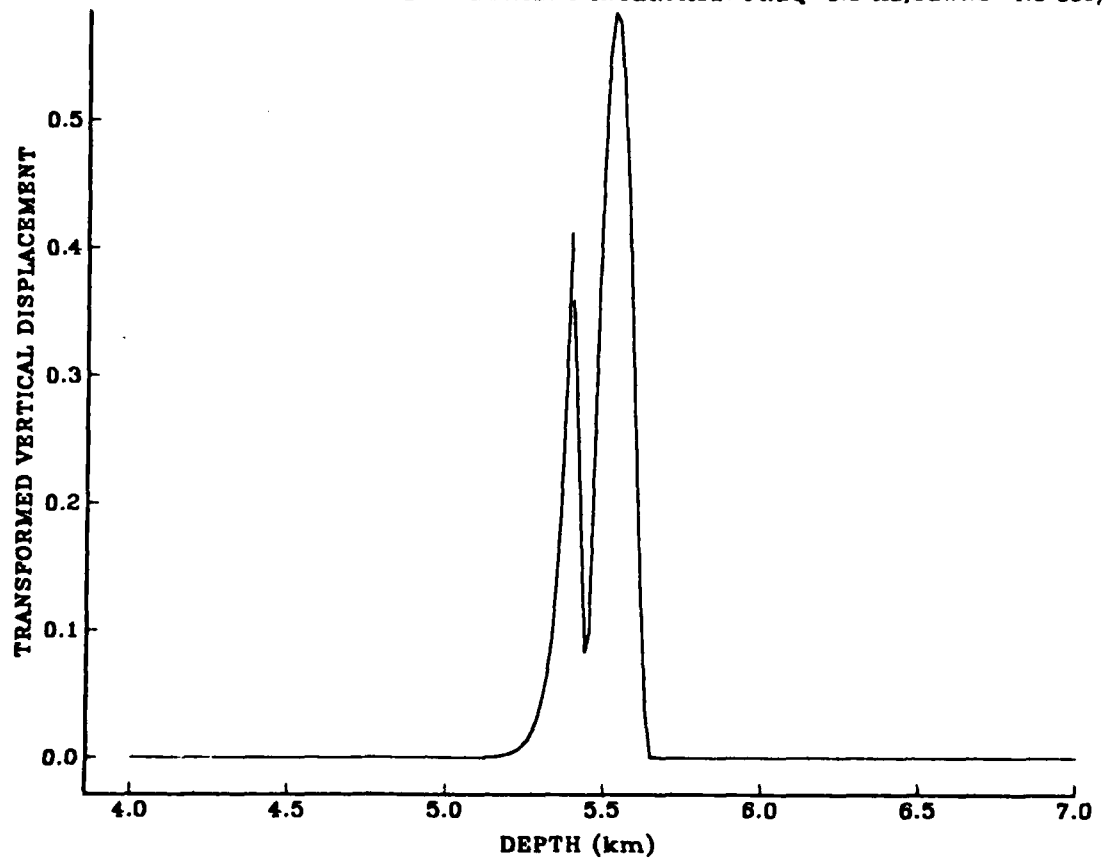
Figure 7. $|\ U_s(p,\omega,z)\ |$ plotted versus depth for a frequency of 1.0 Hz and a horizontal slowness of 4 s km^{-1}. This point, in Figure 3, corresponds to the first overtone of the fundamental Stoneley mode. In this case two oscillations occur in the wavefunction while propagating in the sediments.

Thick Sediment
Chert
Range=10 km

WATER ☐

SEDIMENT △

CHERT ◇

BASEMENT +

×
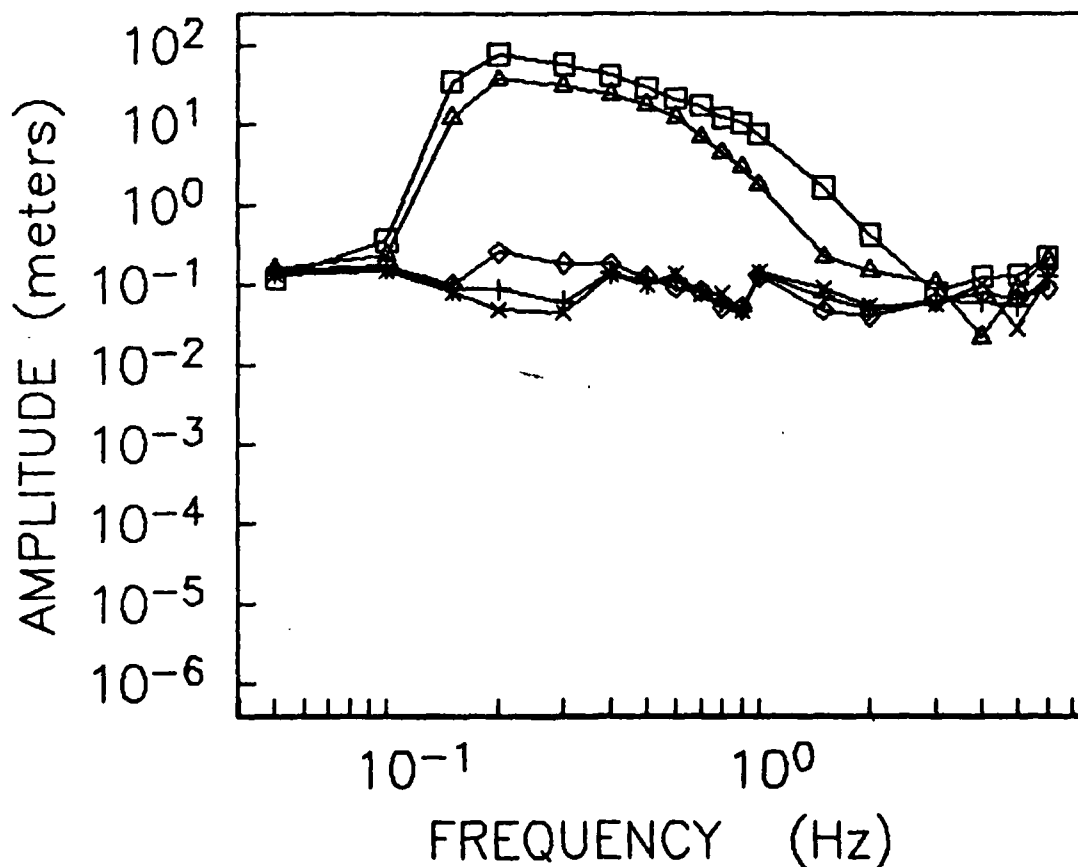
Figure 8. Spectra at a source-receiver separation of 10 km for all modes of propagation. The receiver depths are keyed to the arrows and symbols in Figure 5. The two deepest receivers are within the oceanic basement rocks. The broad peaks for the sea floor and mid-sedimentary receivers are caused almost solely by the propagation of low phase and group velocity Stoneley waves. We note the dramatic decrease in amplitude as the receiver moves below the sedimentary ooze layer into the chert and underlying basement. The spectra for the shallow receivers is obviously very band-limited and, although not shown here, the peak frequency increases as the sedimentary thickness decreases. The spectra were obtained by computing a zero-order Hankel transform of several depth points on vertical wavefunctions such as that in Figure 6.

Figure 9. Amplitude spectra at 10 km range for two crustal models consisting of a 100-meter thick chert layer over a basement and below either a thick (400 m) or a thin (250 m) layer of sediments; overlying the sediments is 5.4 km of fluid. The source is a vertical point force at the sea floor and receivers are at the sea floor and 50 meters into the chert.
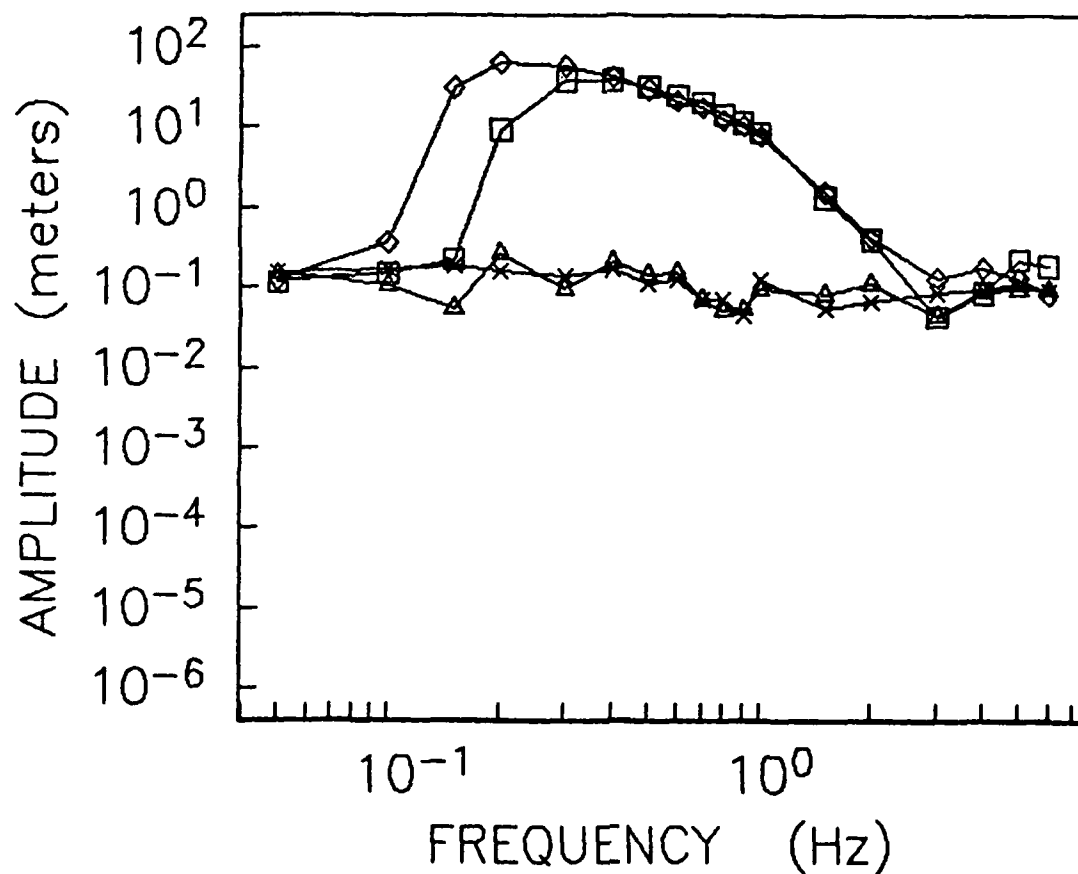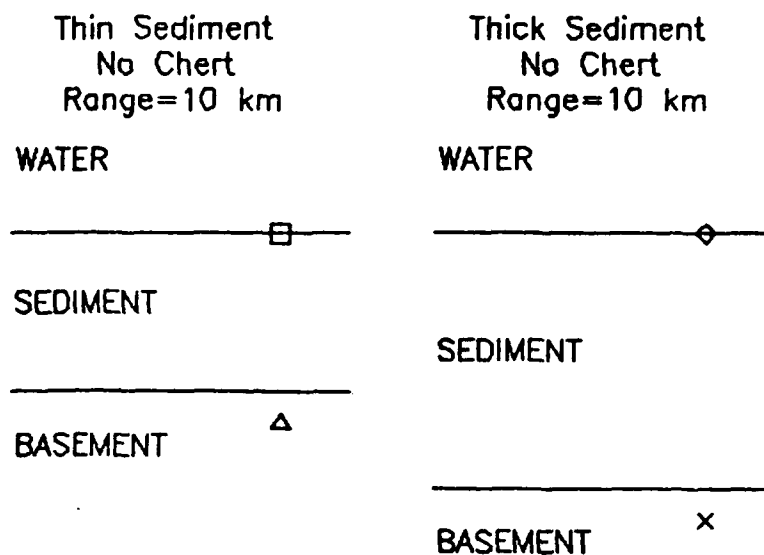
Thin Sediment
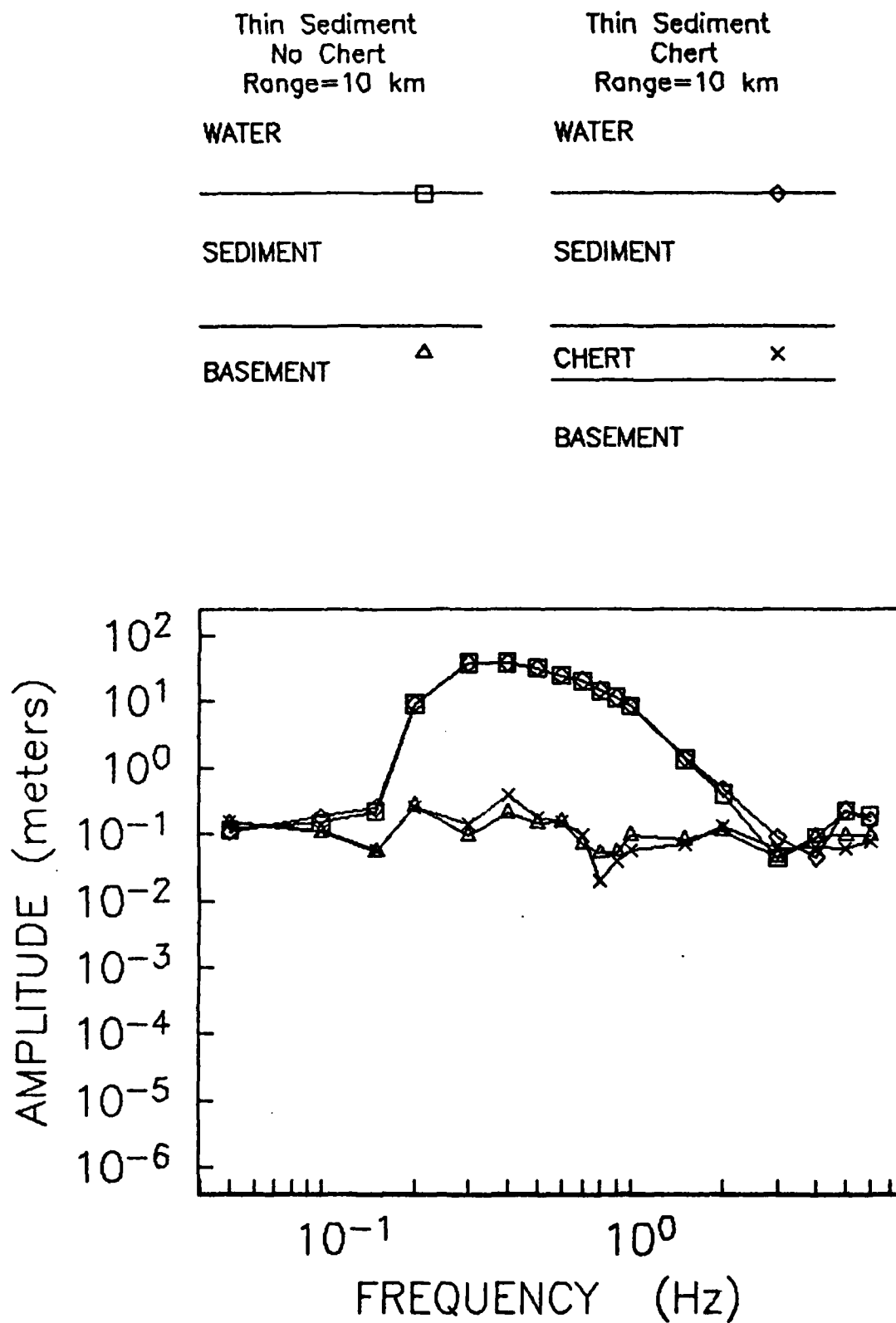Chert
Range=1100 km

WATER

————————————□————

SEDIMENT

CHERT   △

BASEMENT

Thick Sediment
Chert
Range=1100 km

WATER

————————————◇————

SEDIMENT

CHERT   ×

BASEMENT

10^2
10^1
10^0
10^{-1}
10^{-2}
10^{-3}
10^{-4}
10^{-5}
10^{-6}

AMPLITUDE (meters)

10^{-1} 10^0

FREQUENCY (Hz)
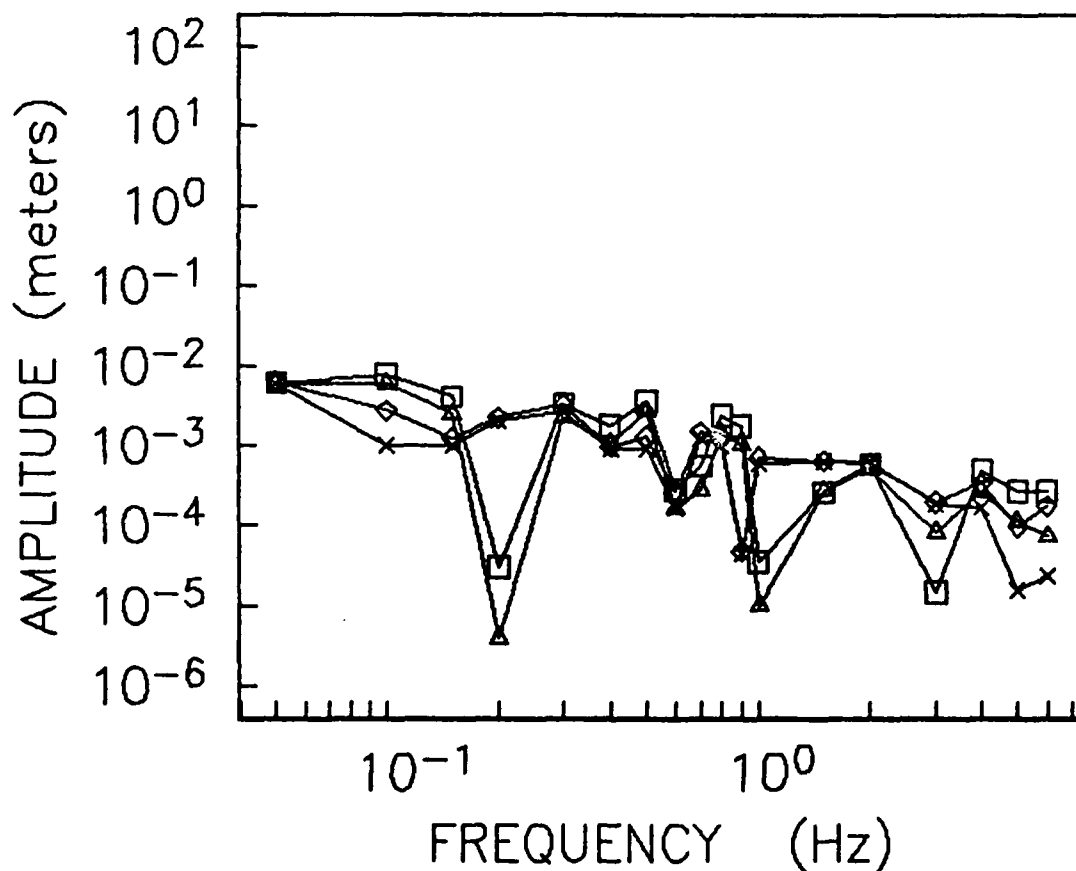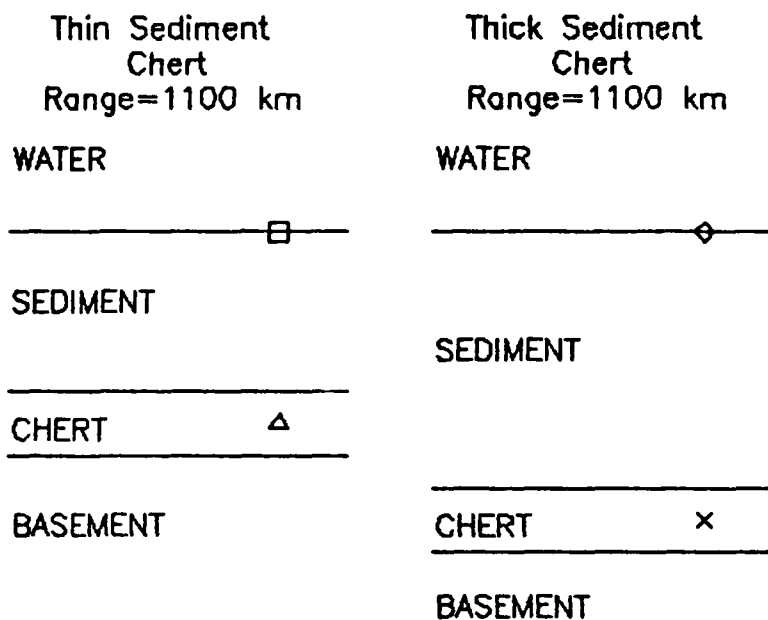
Figure 10. Amplitude spectra at 1100 km range for two crustal models consisting of a 100-m
thick chert layer over a basement and below either a thick (400 m) or a thin (250 m) layer
of sediments; overlying the sediments is 5.4 km of fluid. The source is a vertical point force
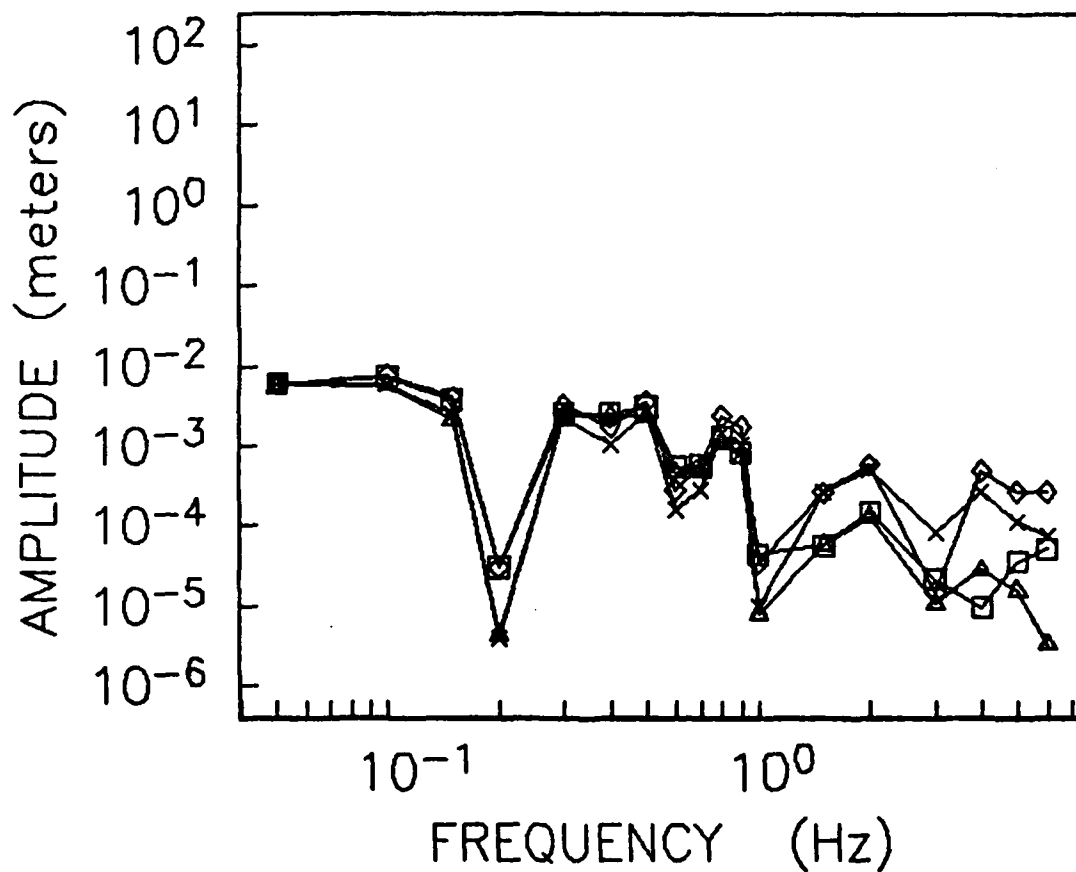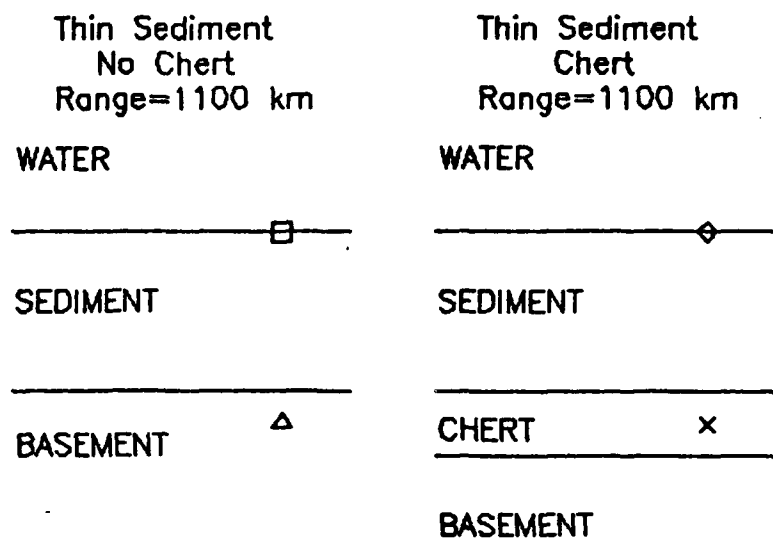at the sea floor and receivers are at the sea floor and 50 meters into the chert.

Figure 11. Amplitude spectra at 10 km range for two crustal models consisting of either a thick (400 m) or thin (250 m) sediment layer above a more rigid basement and below 5.4 km of fluid. The source is a vertical point force at the sea floor and receivers are at the sea floor and 50 meters into the basement.
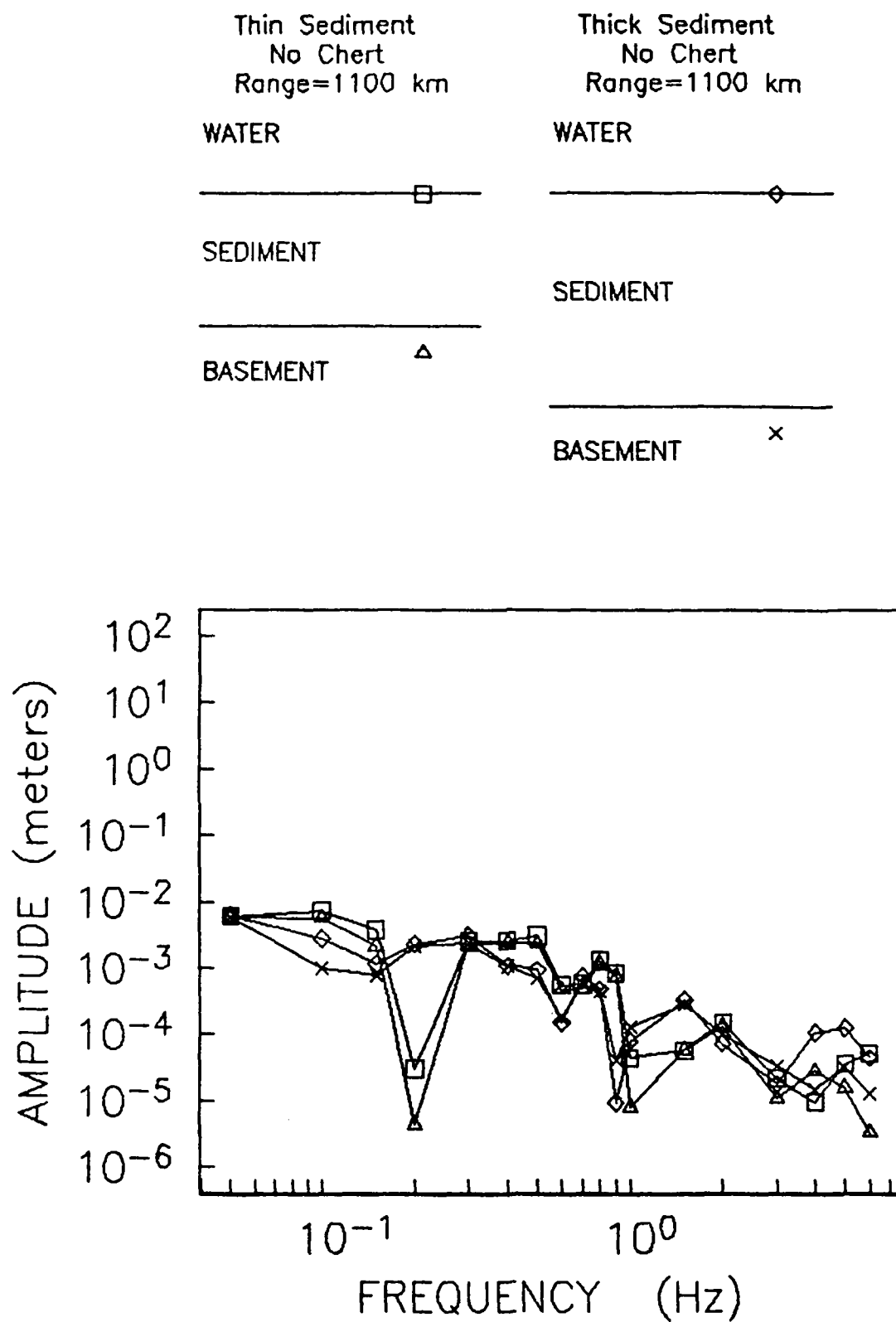
Figure 12. Amplitude spectra at 1100 km range for two crustal models consisting of either a thick (400 m) or thin (250 m) sediment layer above a more rigid basement and below 5.4 km of fluid. The source is a vertical point force at the sea floor and receivers are at the sea floor and 50 meters into the basement.
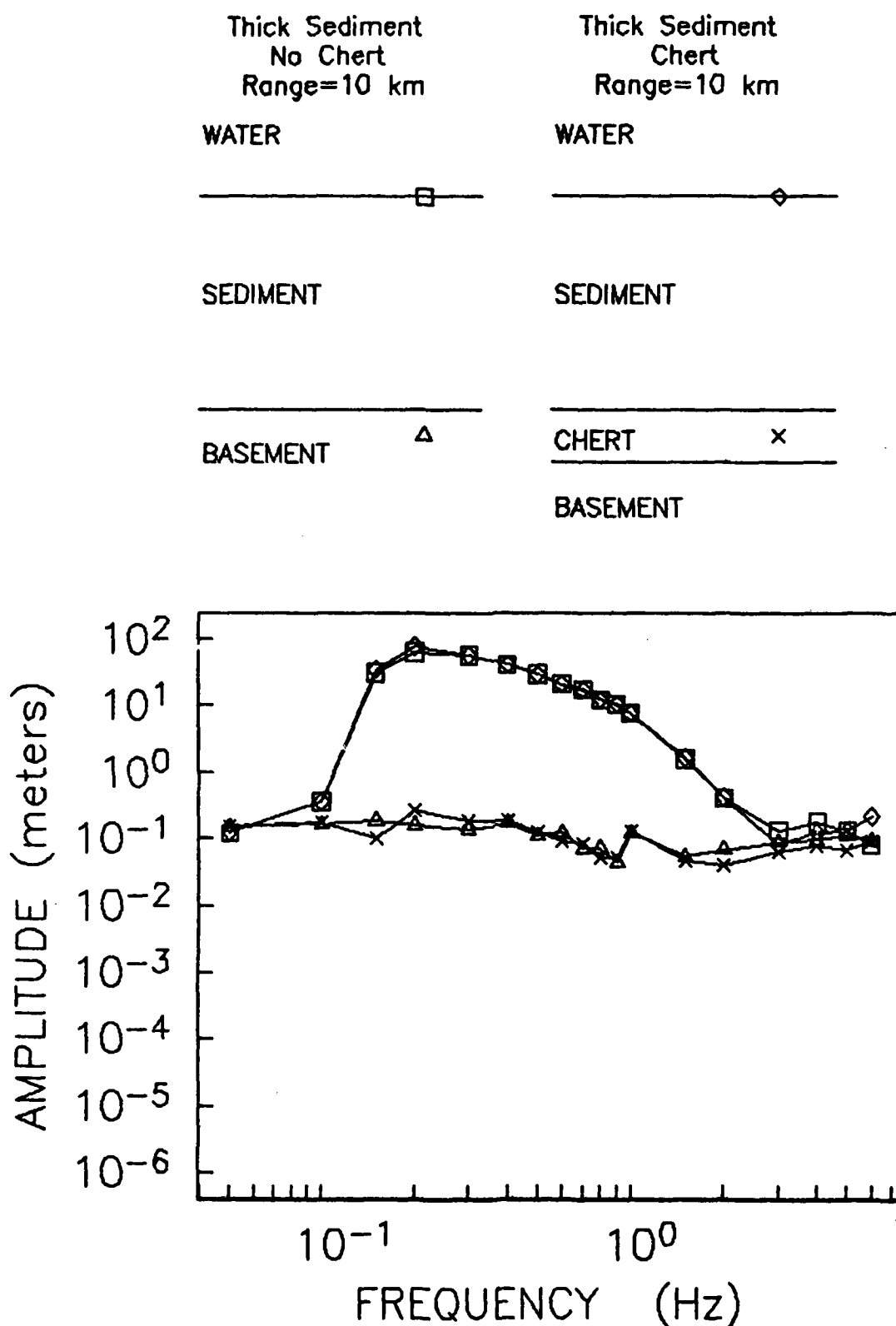
Figure 13. Amplitude spectra at 10 km range for two crustal models consisting of a thin (250 m) sediment layer overlain by 5.4 km of fluid and above either a basement or 100 meters of chert and a basement. The source is a vertical point force at the sea floor and receivers are at the sea floor and 50 meters below the sediments.
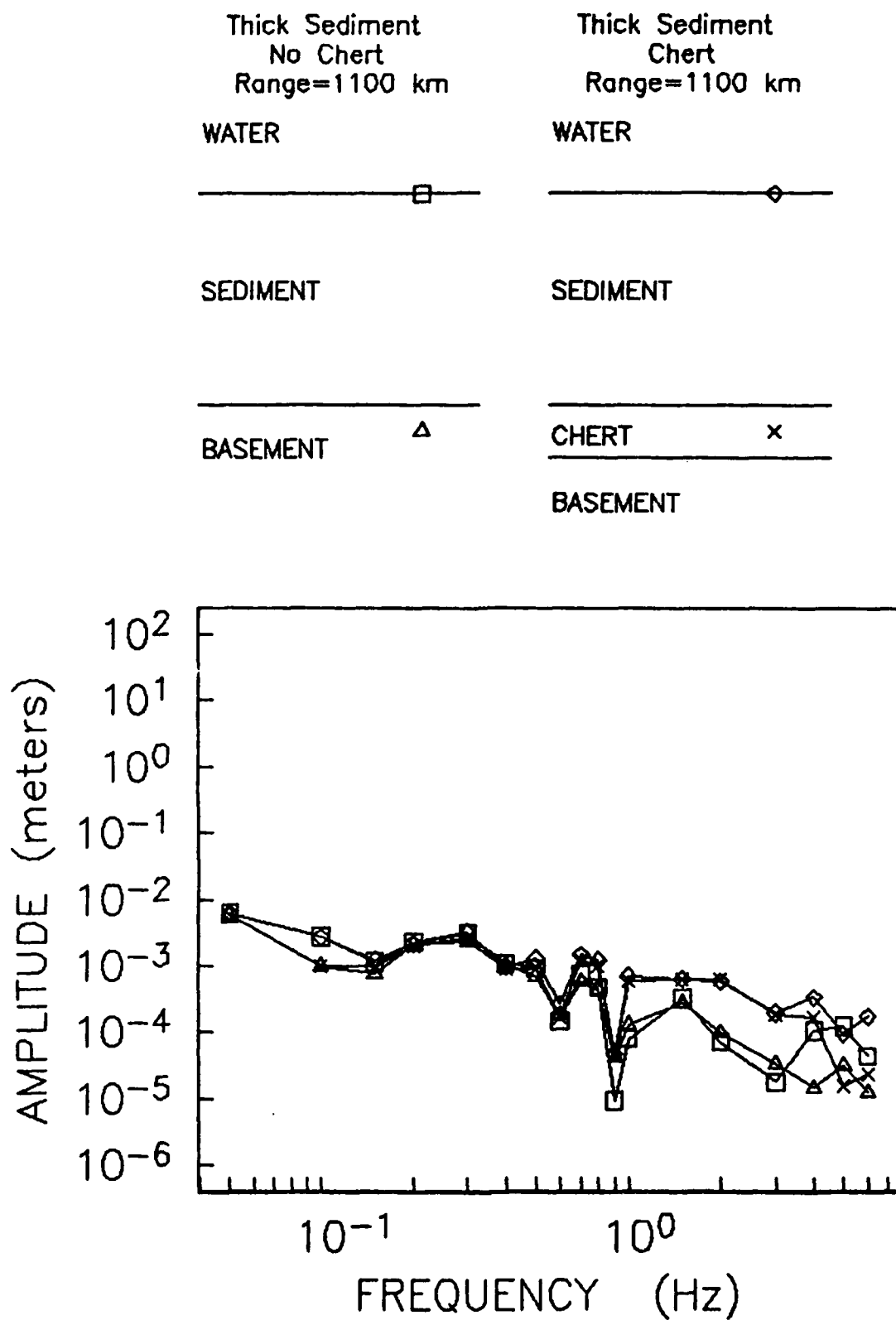
Figure 14. Amplitude spectra at 1100 km range for two crustal models consisting of a thin (250 m) sediment layer overlain by 5.4 km of fluid and above either a basement or 100 meters of chert and a basement. The source is a vertical point force at the sea floor and receivers are at the sea floor and 50 meters below the sediments.

Thick Sediment
No Chert
Range=10 km

WATER

────────────□────────────

SEDIMENT

─────────────────────────   △

BASEMENT

Thick Sediment
Chert
Range=10 km

WATER

────────────◇────────────

SEDIMENT

─────────────────────────

CHERT   ×

─────────────────────────

BASEMENT

Figure 15. Amplitude spectra at 10 km range for two crustal models consisting of a thick (400 m) sediment layer overlain by 5.4 km of fluid and above either a basement or 100 meters of chert and a basement. The source is a vertical point force at the sea floor and receivers are at the sea floor and 50 meters below the sediments.

Thick Sediment
No Chert
Range=1100 km

WATER

SEDIMENT

BASEMENT

Thick Sediment
Chert
Range=1100 km

WATER

SEDIMENT

CHERT

BASEMENT
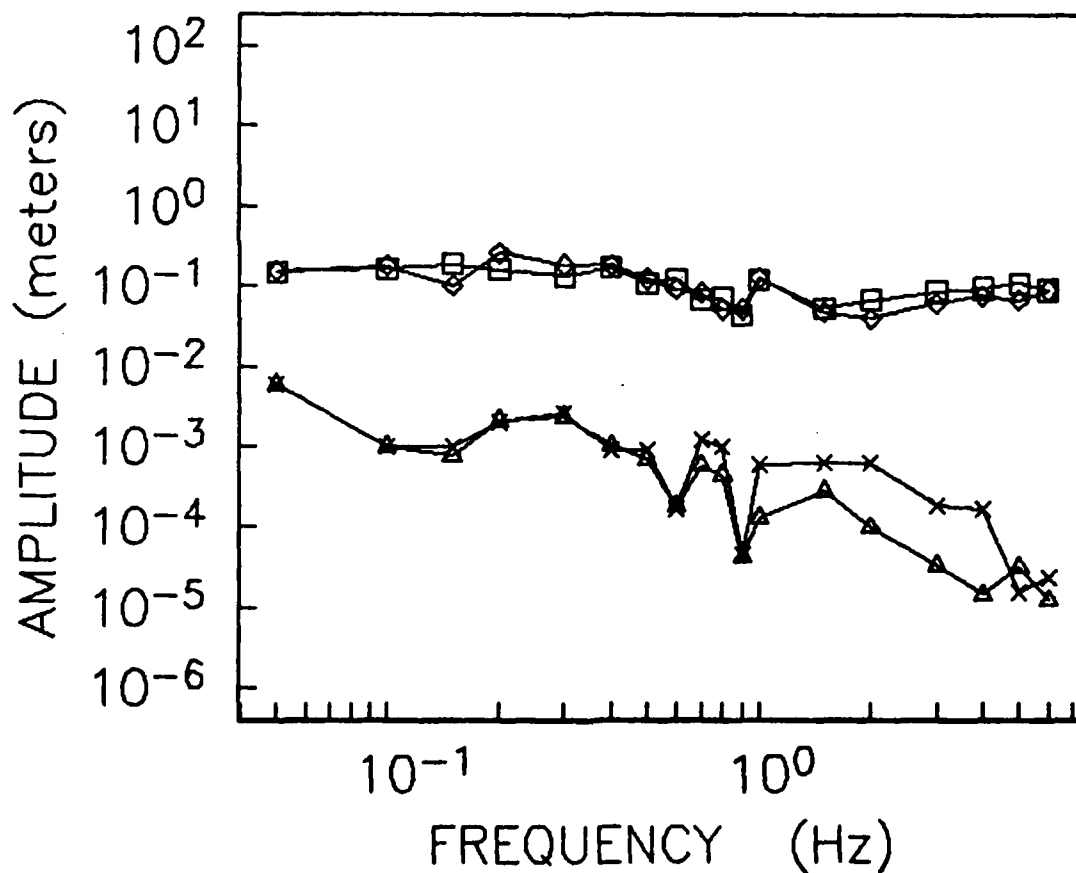
Figure 16. Amplitude spectra at 1100 km range for two crustal models consisting of a thick (400 m) sediment layer overlain by 5.4 km of fluid and above either a basement or 100 meters of chert and a basement. The source is a vertical point force at the sea floor and receivers are at the sea floor and 50 meters below the sediments.

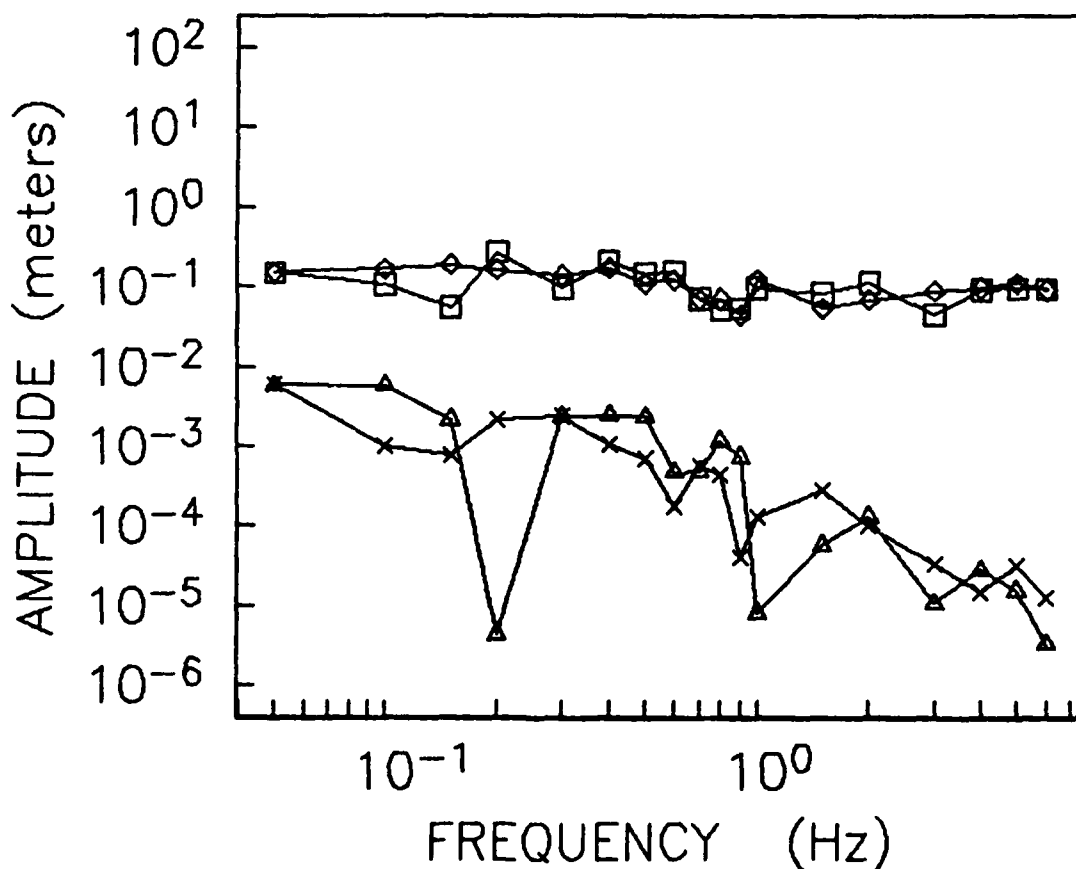| Thin Sediment No Chert Range=10 km	Thin Sediment No Chert Range=1100 km	Thin Sediment Chert Range=10 km	Thin Sediment Chert Range=1100 km
WATER	WATER	WATER	WATER
SEDIMENT	SEDIMENT	SEDIMENT	SEDIMENT
BASEMENT □	BASEMENT △	CHERT ◇	CHERT ×
		BASEMENT	BASEMENT

Figure 17. Amplitude spectra at ranges 10 and 1100 km for two crustal models consisting of a thin (250 m) layer of sediments overlain by 5.4 km of fluid and above either a basement or 100 meters of chert and a basement. The source is a vertical point force at the sea floor and the receivers are 50 meters below the sediments.

Thick Sediment No Chert Range=10 km	Thick Sediment No Chert Range=1100 km	Thick Sediment Chert Range=10 km	Thick Sediment Chert Range=1100 km
WATER	WATER	WATER	WATER
SEDIMENT	SEDIMENT	SEDIMENT	SEDIMENT
BASEMENT □	BASEMENT △	CHERT ◇	CHERT ×
		BASEMENT	BASEMENT

Figure 18. Amplitude spectra at ranges 10 and 1100 km for two crustal models consisting of a thick (400 m) layer of sediments overlain by 5.4 km of fluid and above either a basement or 100 meters of chert and a basement. The source is a vertical point force at the sea floor and the receivers are 50 meters below the sediments.

Figure 19. Amplitude spectra at ranges 10 and 1100 km for two crustal models consisting of either a thin (250 m) or thick (400 m) sediment layer above a basement and below 5.4 km of fluid. The source is a vertical point force at the sea floor and the receivers are 50 meters below the sediments.
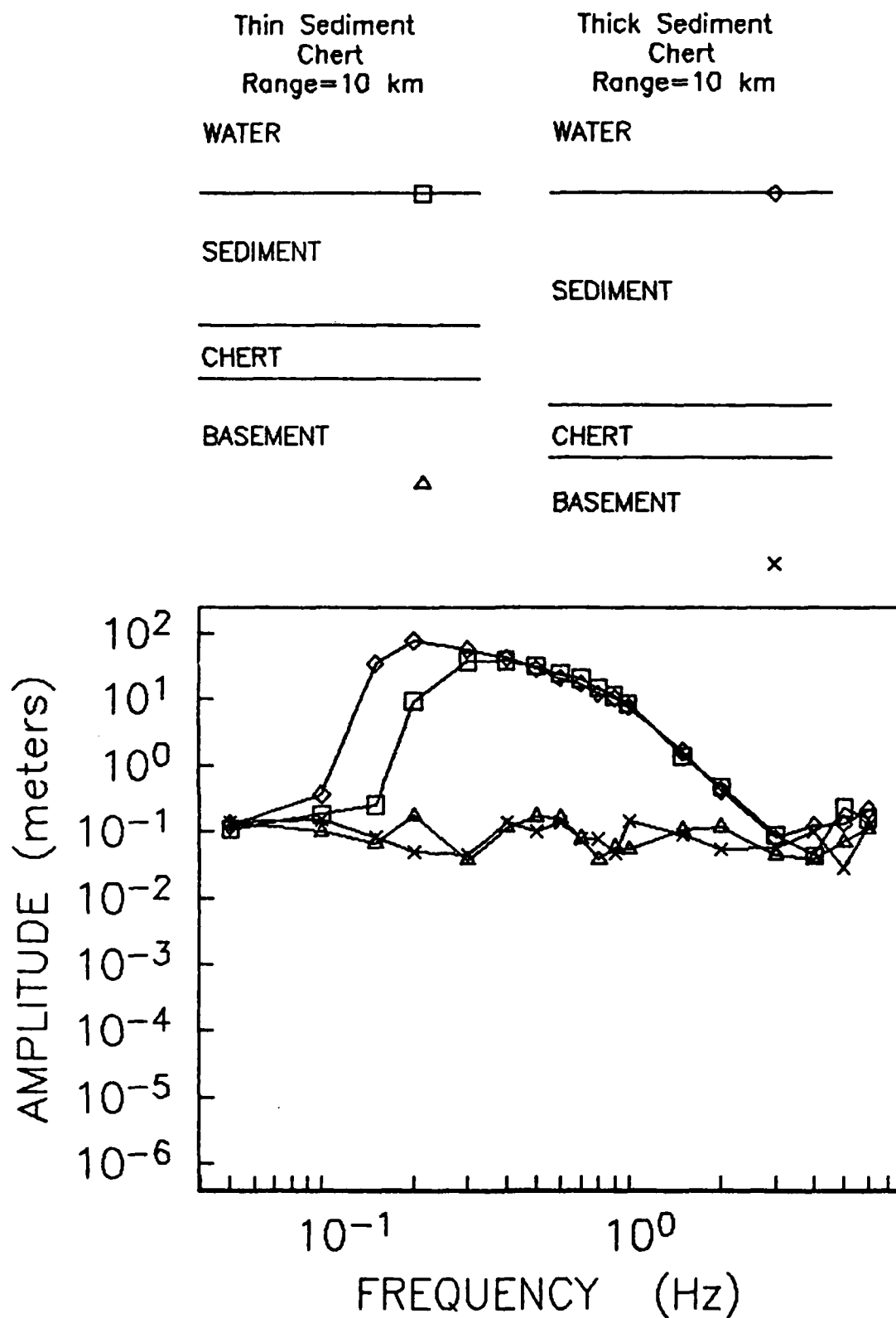
Figure 20. Amplitude spectra at 10 km range for two crustal models consisting of a 100-meter thick chert layer over a basement and below either a thick (400 m) or a thin (250 m) layer of sediments; overlying the sediments is 5.4 km of fluid. The source is a vertical point force at the sea floor and receivers are at the sea floor and 200 meters into the basement.
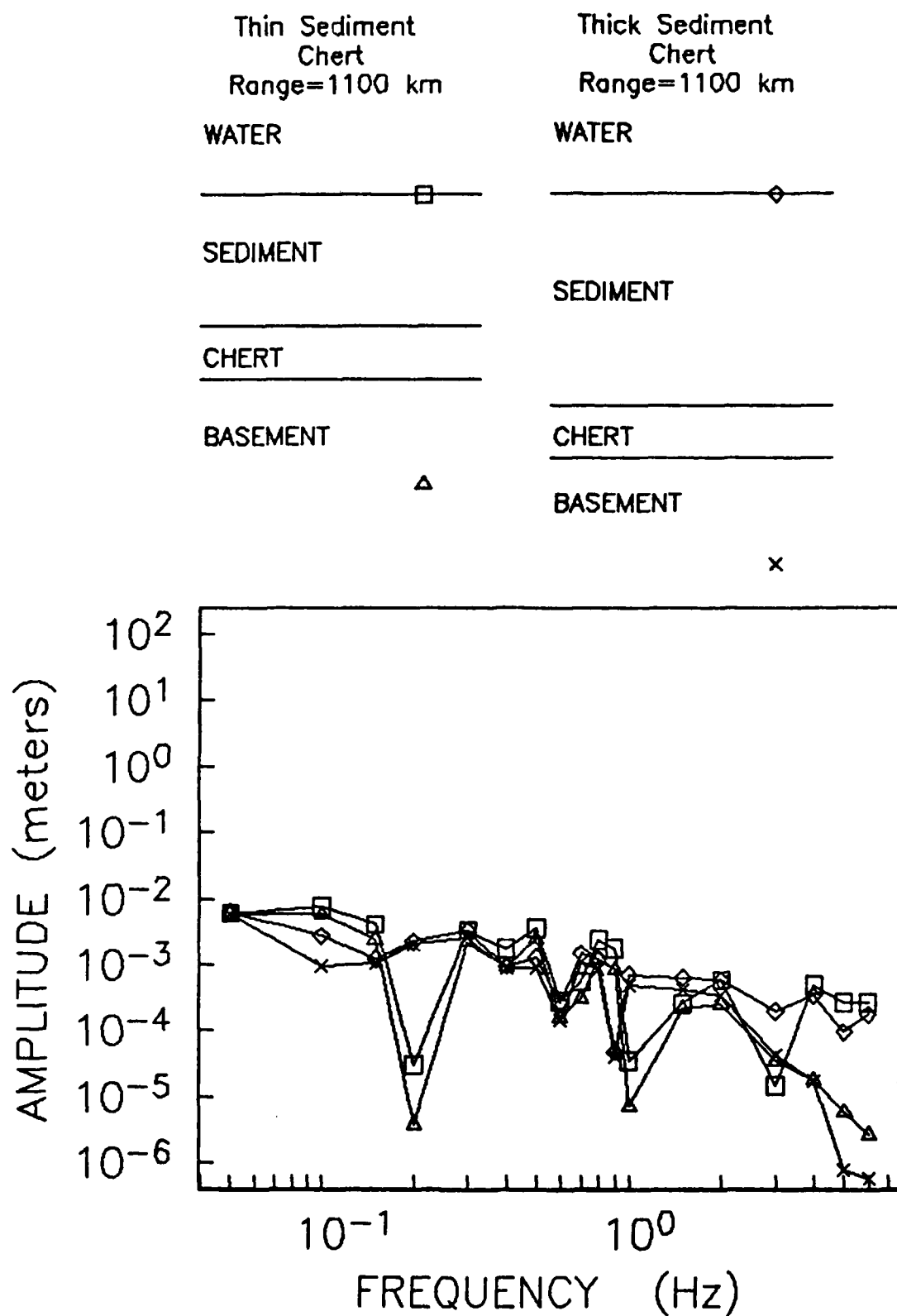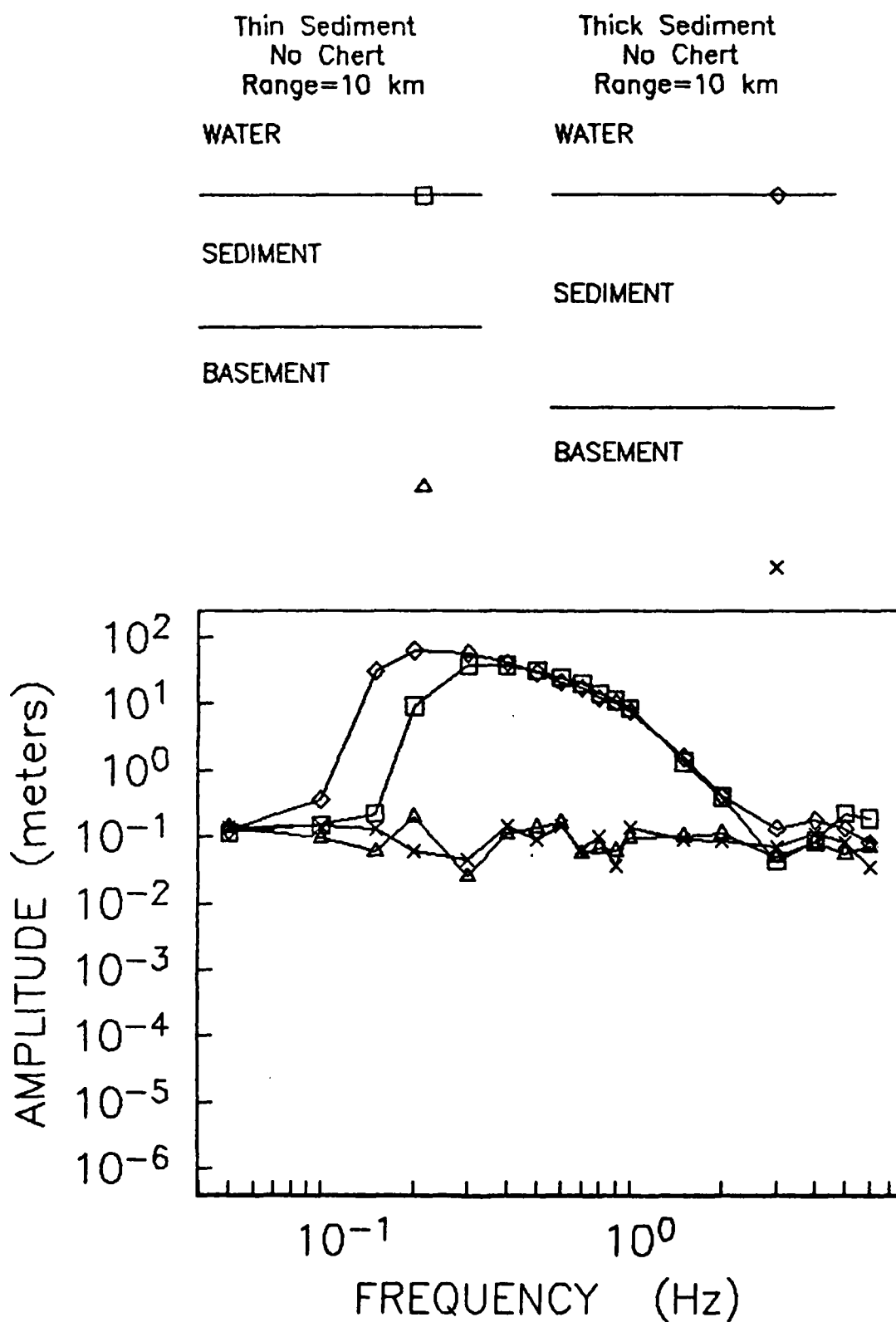
Figure 21. Amplitude spectra at 1100 km range for two crustal models consisting of a 100-meter thick chert layer over a basement and below either a thick (400 m) or a thin (250 m) layer of sediments; overlying the sediments is 5.4 km of fluid. The source is a vertical point force at the sea floor and receivers are at the sea floor and 200 meters into the basement.

Thin Sediment
No Chert
Range=10 km

Thick Sediment
No Chert
Range=10 km
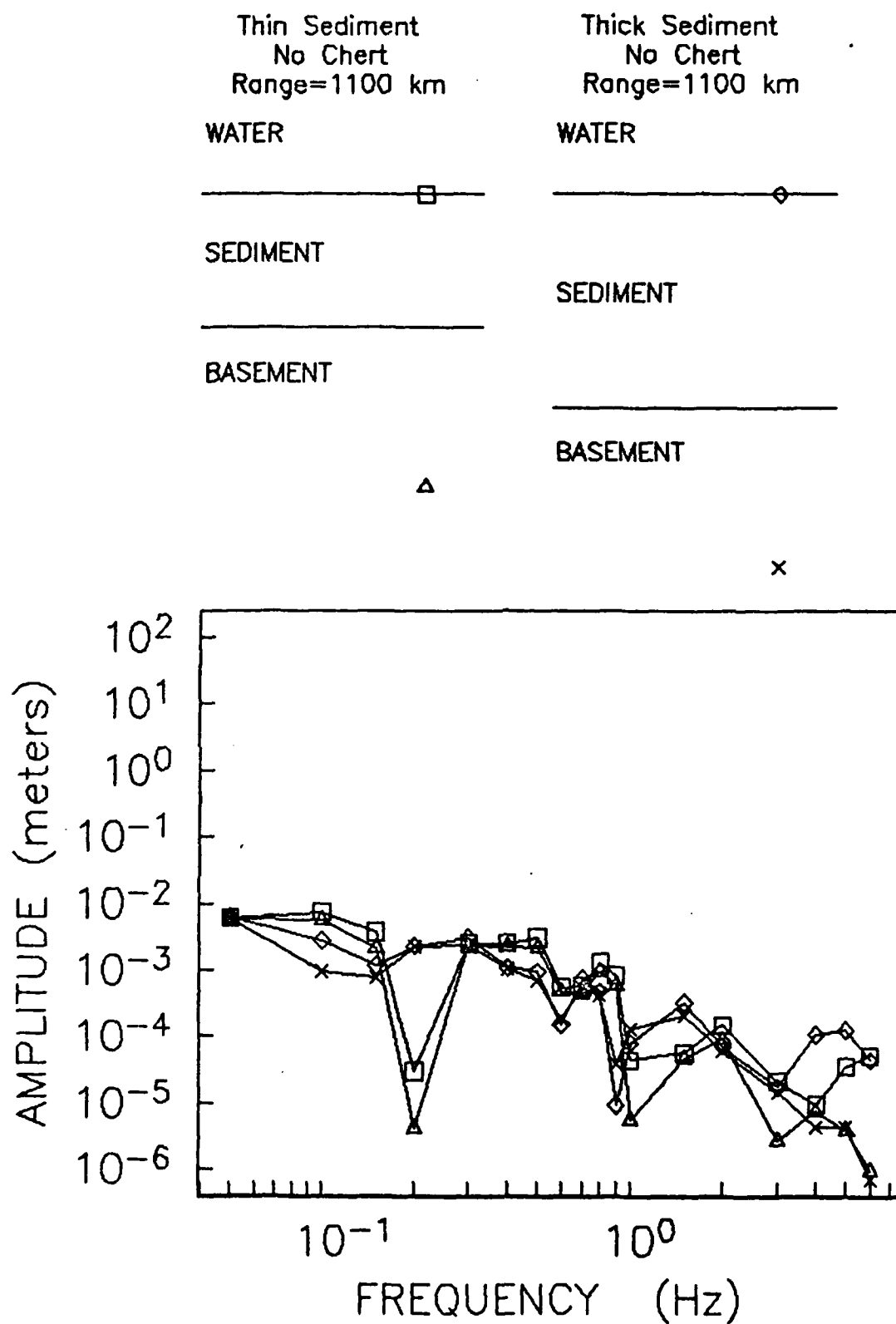
WATER

WATER

SEDIMENT

SEDIMENT

BASEMENT

BASEMENT

Figure 22. Amplitude spectra at 10 km range for two crustal models consisting of either a thick (400 m) or thin (250 m) sediment layer above a more rigid basement and below 5.4 km of fluid. The source is a vertical point force at the sea floor and receivers are at the sea floor and 200 meters into the basement.
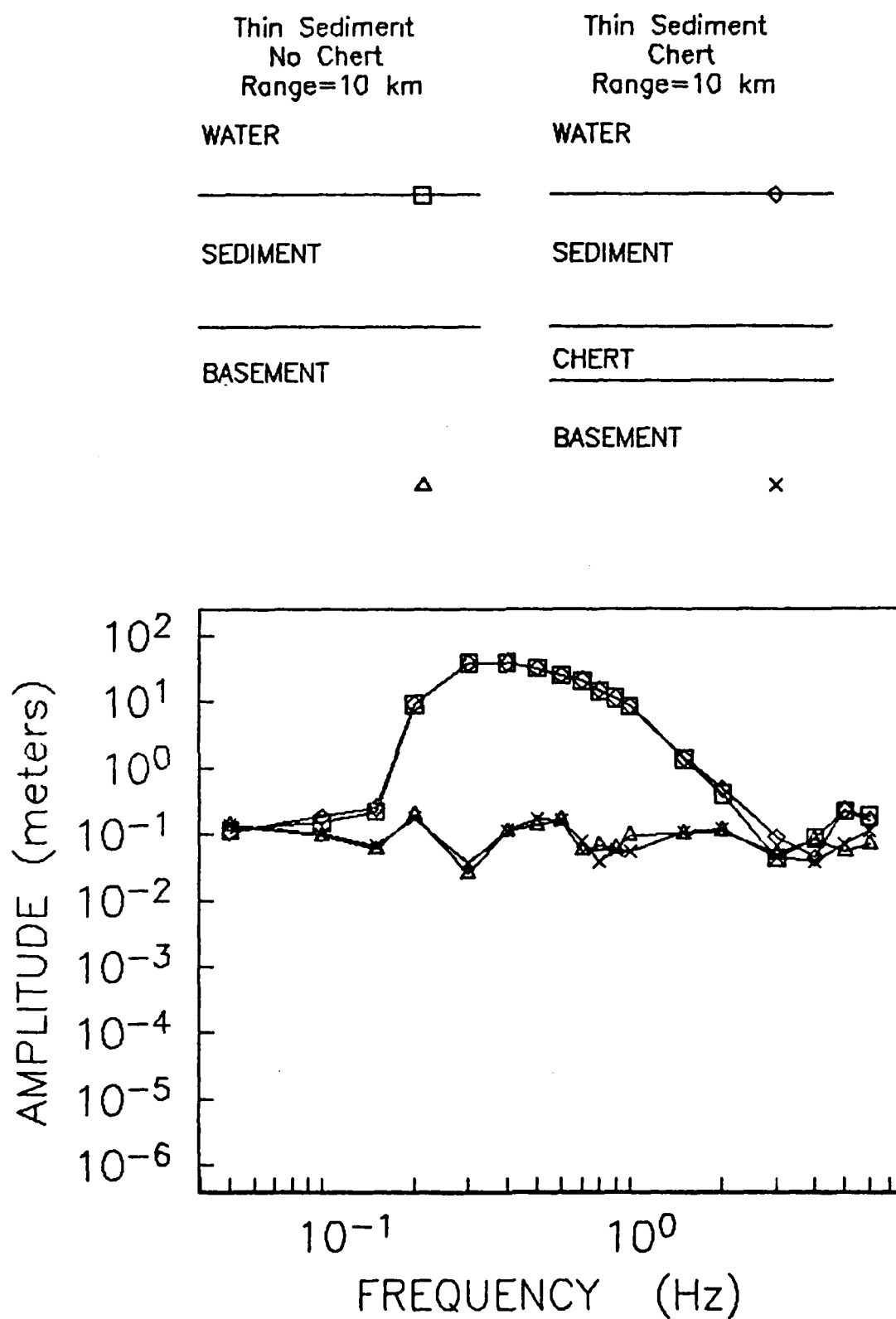
Thin Sediment
No Chert
Range=1100 km

WATER

□

SEDIMENT

BASEMENT

Thick Sediment
No Chert
Range=1100 km

WATER

◇

SEDIMENT

BASEMENT

Δ

×

Figure 23. Amplitude spectra at 1100 km range for two crustal models consisting of either a thick (400 m) or thin (250 m) sediment layer above a more rigid basement and below 5.4 km of fluid. The source is a vertical point force at the sea floor and receivers are at the sea floor and 200 meters into the basement.

Figure 24. Amplitude spectra at 10 km range for two crustal models consisting of a thin (250 m) sediment layer overlain by 5.4 km of fluid and above either a basement or 100 meters of chert and a basement. The source is a vertical point force at the sea floor and receivers are at the sea floor and 300 meters below the sediments, in the basement.
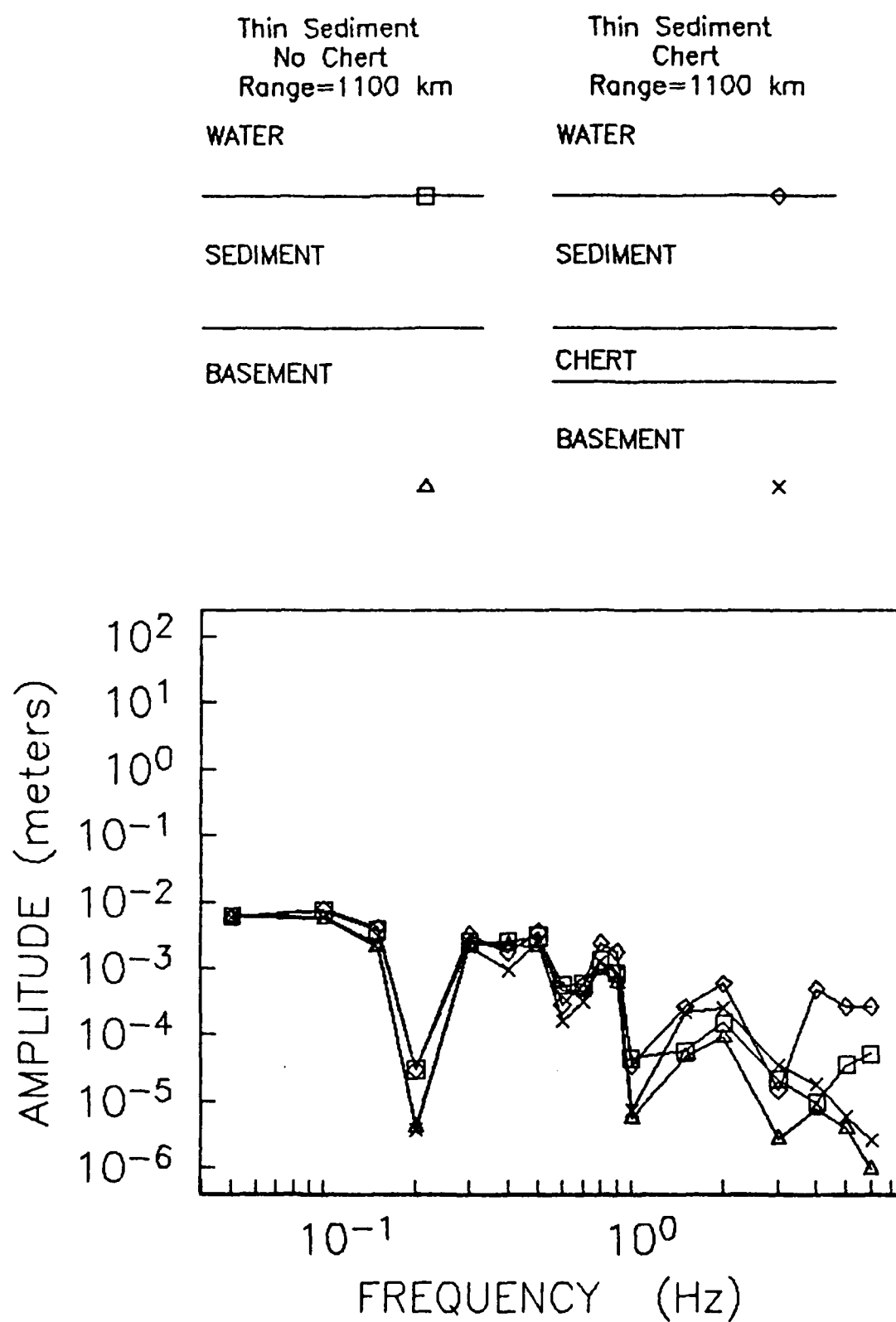
Figure 25. Amplitude spectra at 1100 km range for two crustal models consisting of a thin (250 m) sediment layer overlain by 5.4 km of fluid and above either a basement or 100 meters of chert and a basement. The source is a vertical point force at the sea floor and receivers are at the sea floor and 300 meters below the sediments, in the basement.
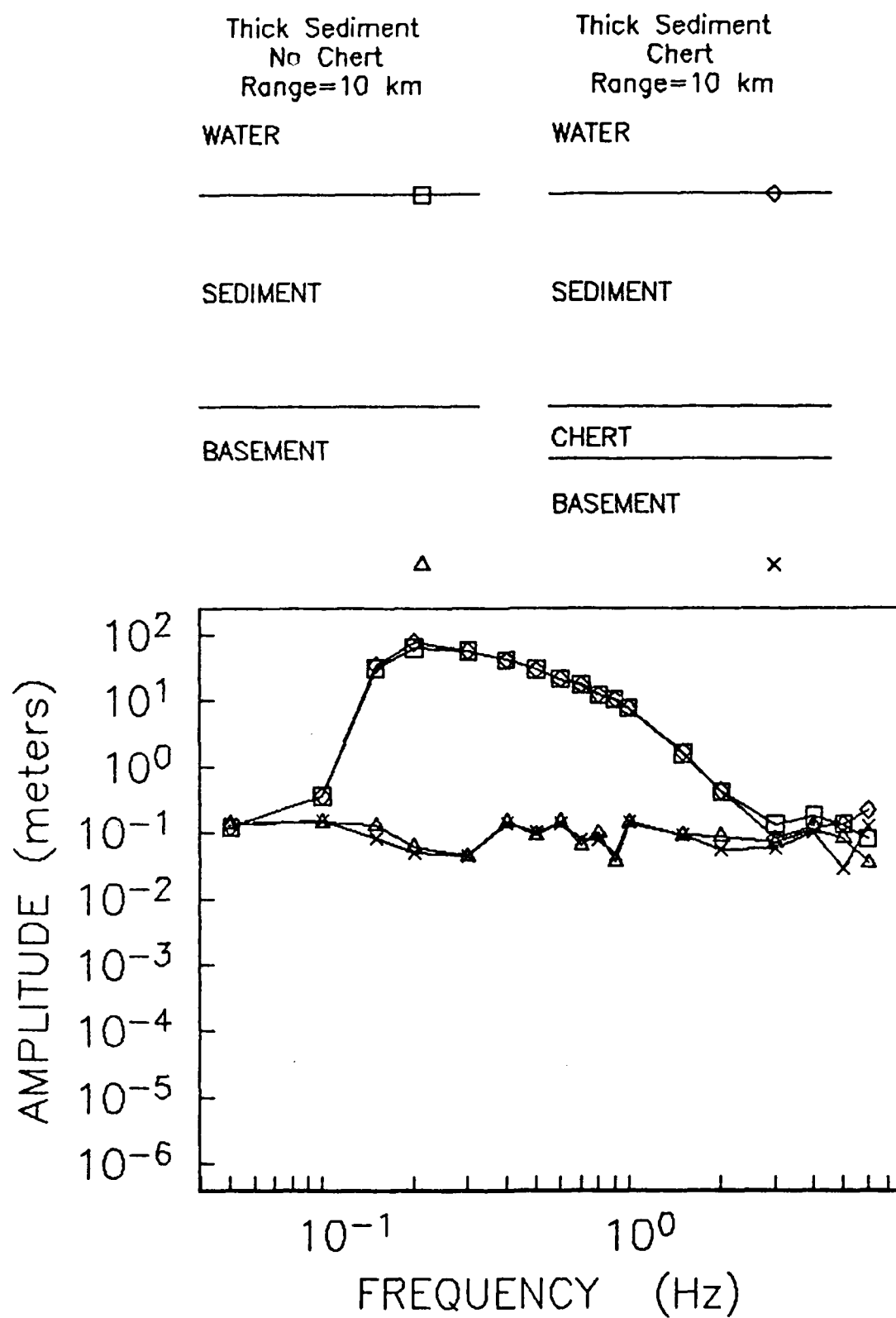
Figure 26. Amplitude spectra at 10 km range for two crustal models consisting of a thick (400 m) sediment layer overlain by 5.4 km of fluid and above either a basement or 100 meters of chert and a basement. The source is a vertical point force at the sea floor and receivers are at the sea floor and 300 meters below the sediments, in the basement.
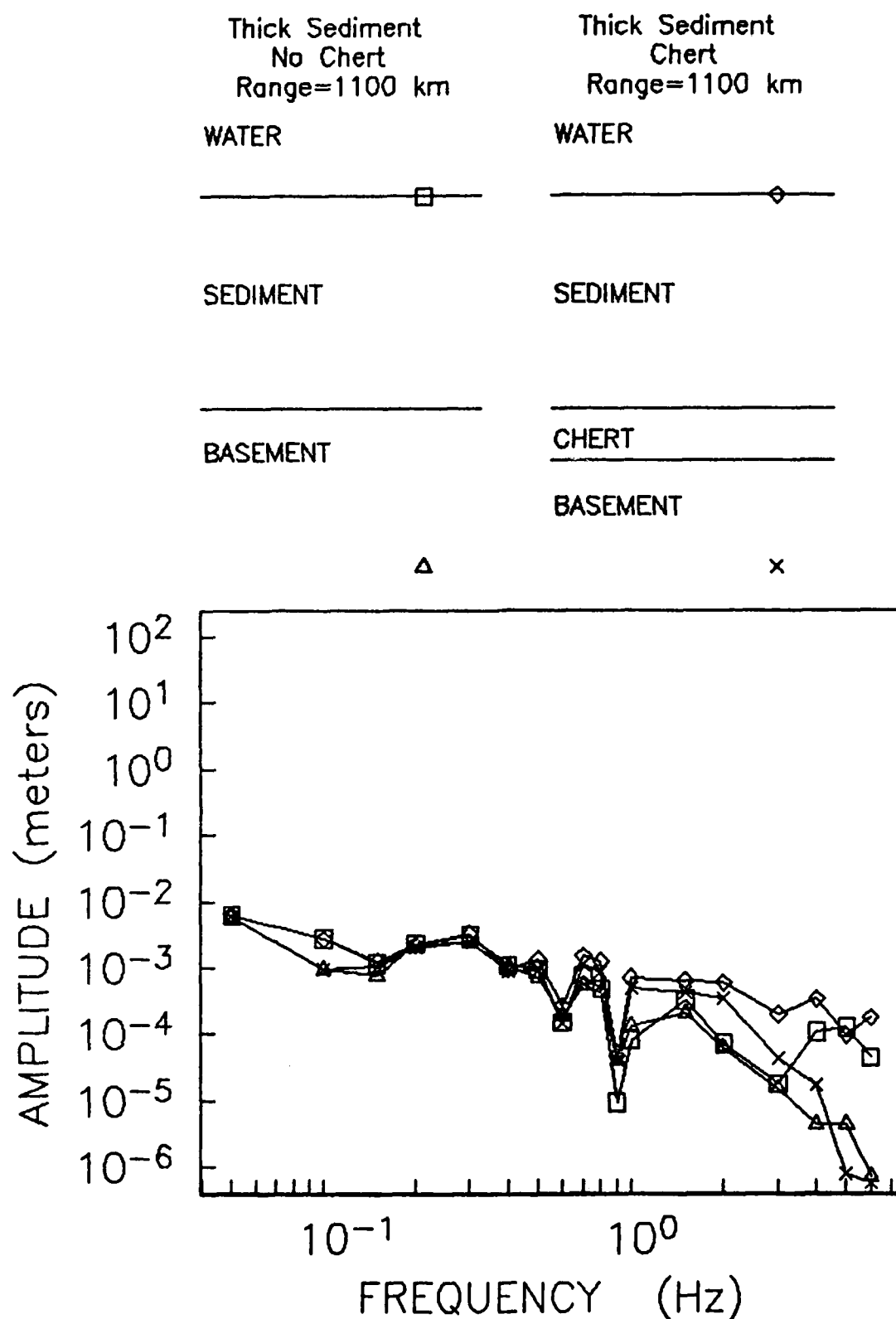
Figure 27. Amplitude spectra at 1100 km range for two crustal models consisting of a thick (400 m) sediment layer overlain by 5.4 km of fluid and above either a basement or 100 meters of chert and a basement. The source is a vertical point force at the sea floor and receivers are at the sea floor and 300 meters below the sediments, in the basement.
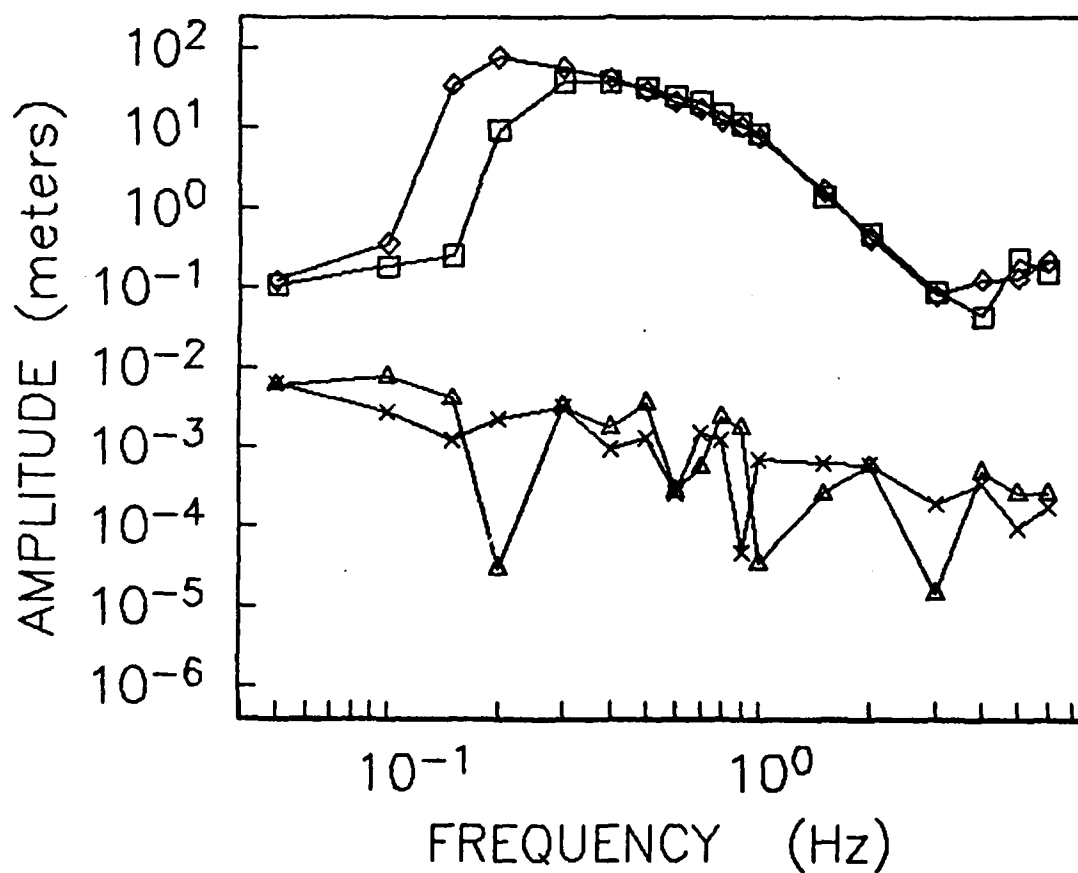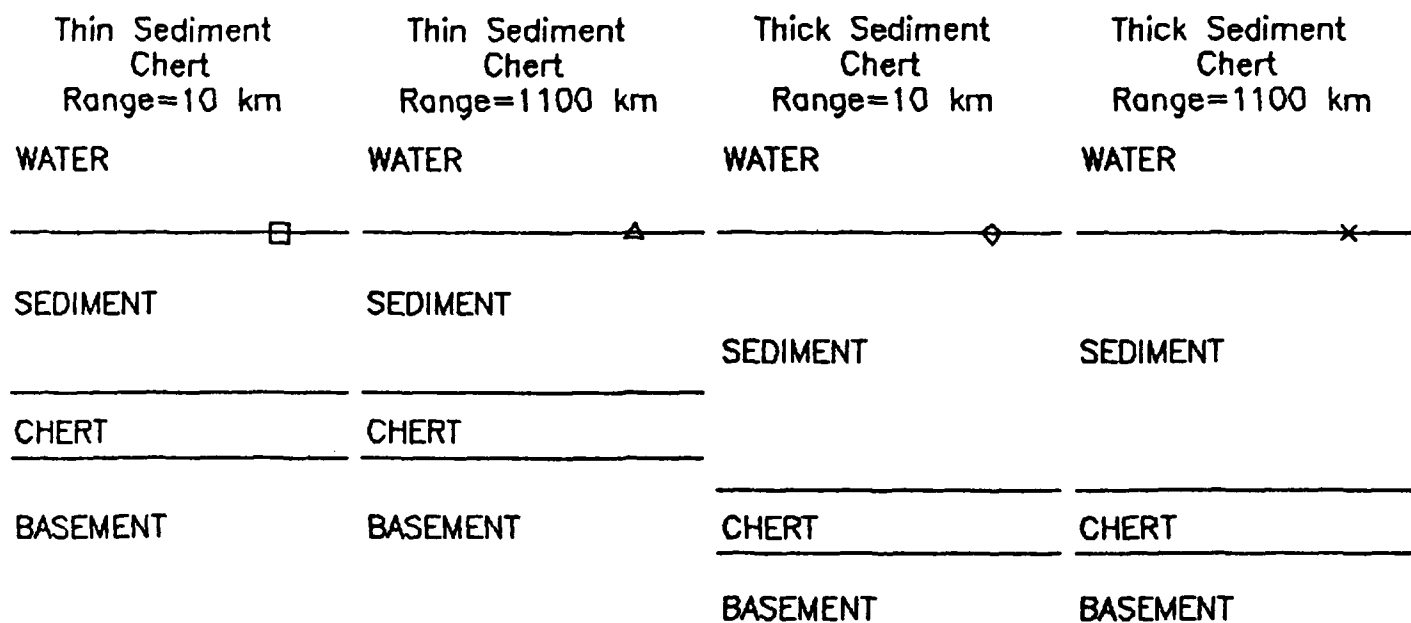
Figure 28. Amplitude spectra at ranges 10 and 1100 km for two crustal models consisting of either a thin (250 m) or thick (400 m) sediment layer overlain by 5.4 km of fluid and above 100 meters of chert and a basement. The source is a vertical point force and the receivers are at the sea floor.

Figure 29. Amplitude spectra at ranges 10 and 1100 km for two crustal models consisting of either a thin (250 m) or thick (400 m) sediment layer overlain by 5.4 km of fluid and above 100 meters of chert and a basement. The source is a vertical point force at the sea floor and the receivers are 200 meters into the basement.
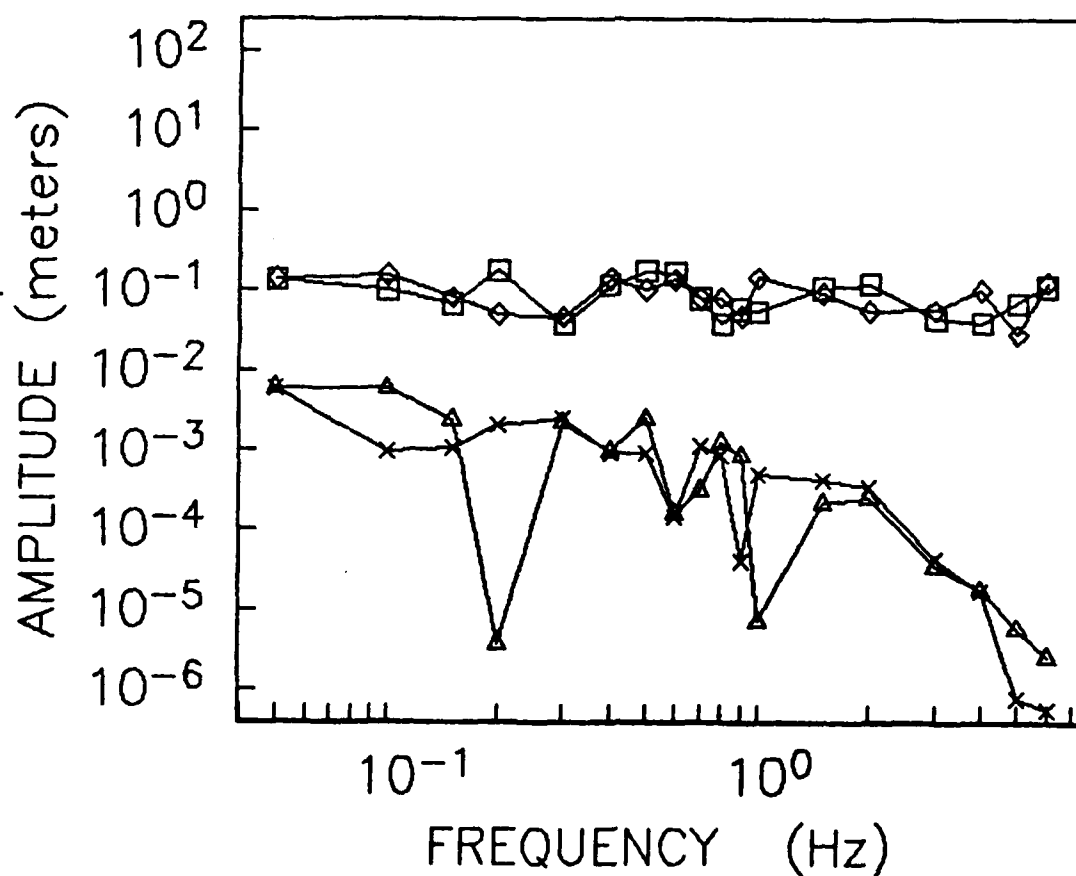
Figure 30. Amplitude spectra at ranges 10 and 1100 km for two crustal models consisting of either a thin (250 m) or thick (400 m) sediment layer overlain by 5.4 km of fluid and a basement. The source is a vertical point force and the receivers are at the sea floor.

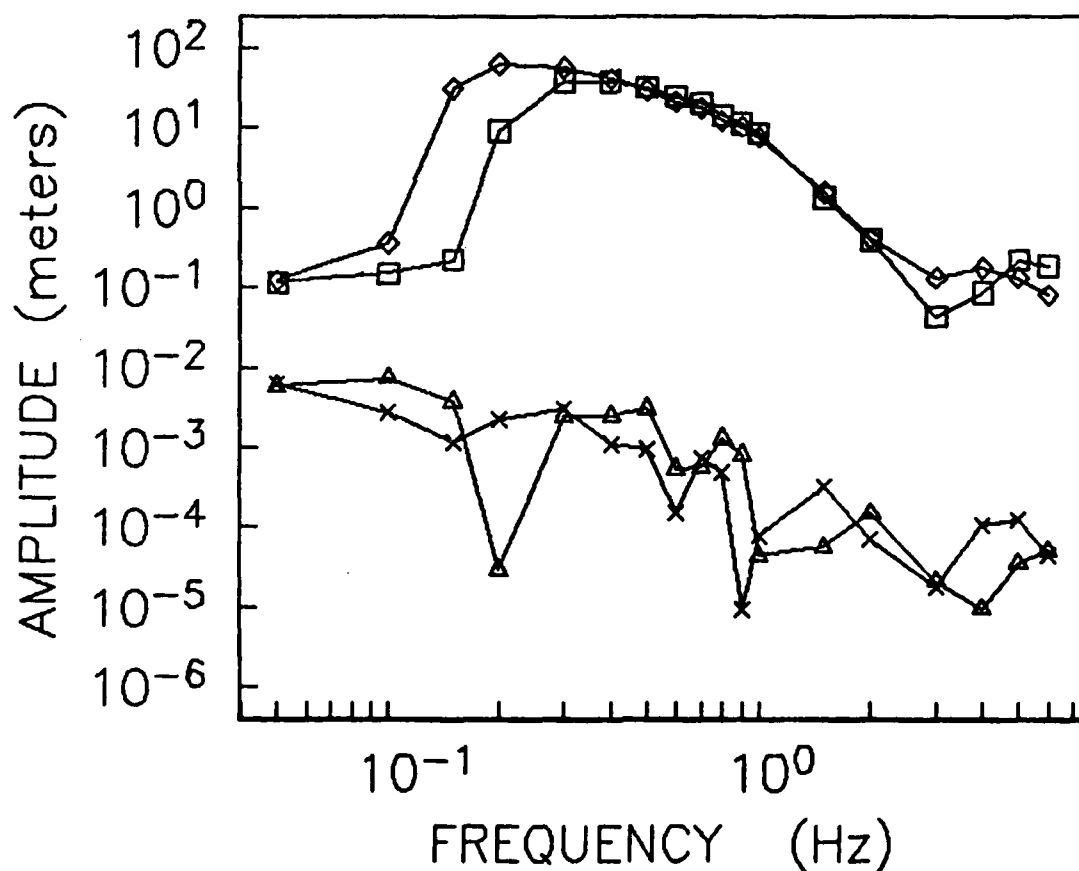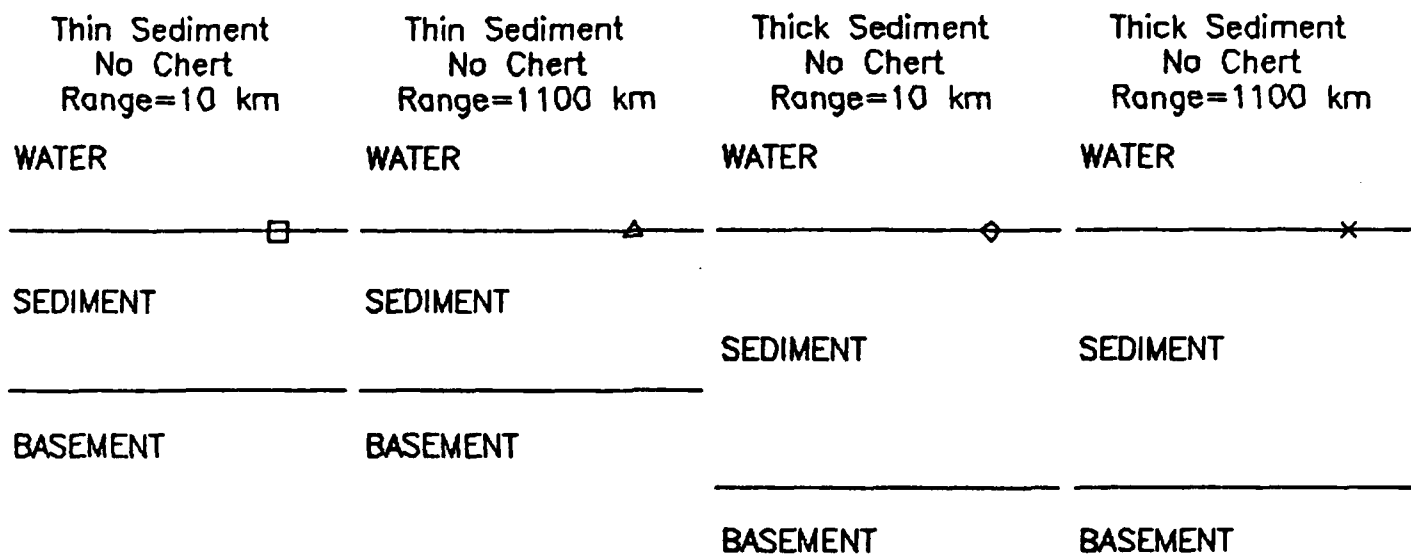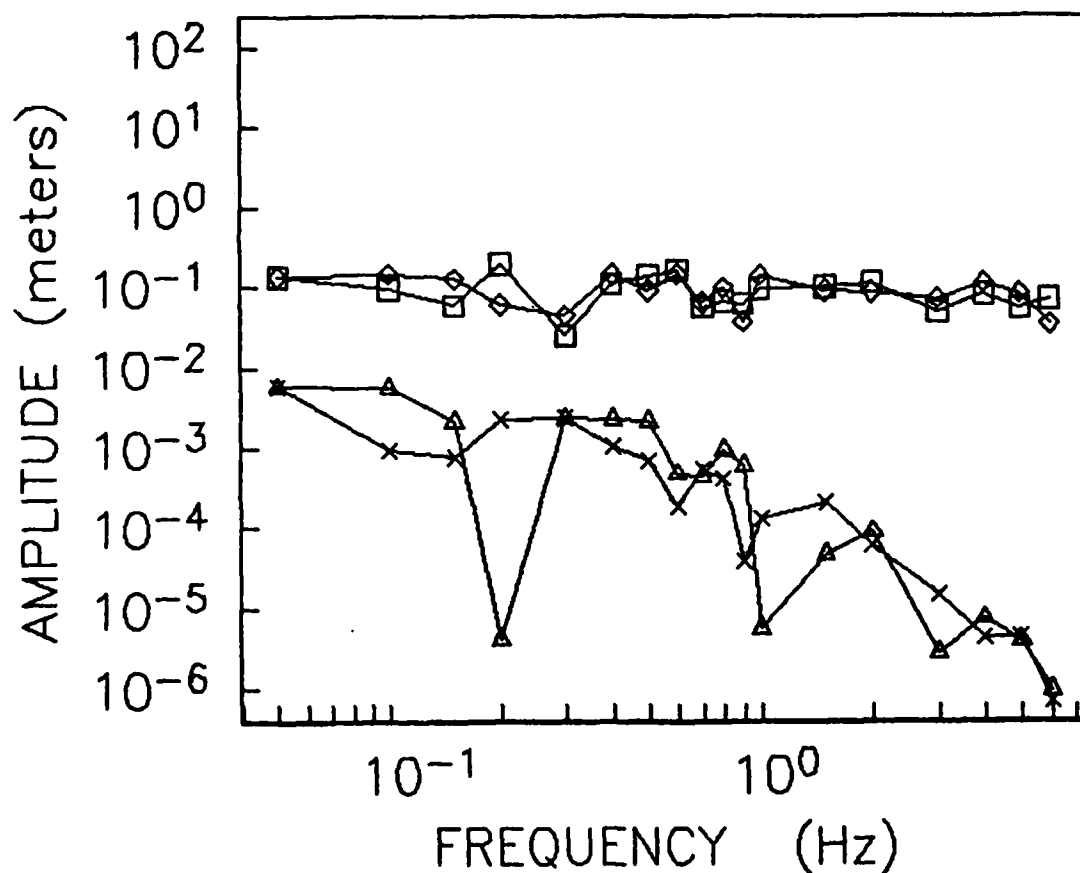| Thin Sediment No Chert Range=10 km	Thin Sediment No Chert Range=1100 km	Thick Sediment No Chert Range=10 km	Thick Sediment No Chert Range=1100 km
WATER	WATER	WATER	WATER
SEDIMENT	SEDIMENT	SEDIMENT	SEDIMENT
BASEMENT	BASEMENT	BASEMENT	BASEMENT
□	△	◇	✕

Figure 31. Amplitude spectra at ranges 10 and 1100 km for two crustal models consisting of either a thin (250 m) or thick (400 m) sediment layer overlain by 5.4 km of fluid and a basement. The source is a vertical point force at the sea floor and the receivers are 200 meters into the basement.

Thin Sediment No Chert Range=10 km	Thin Sediment No Chert Range=1100 km	Thin Sediment Chert Range=10 km	Thin Sediment Chert Range=1100 km
WATER	WATER	WATER	WATER
SEDIMENT	SEDIMENT	SEDIMENT	SEDIMENT
BASEMENT	BASEMENT	CHERT	CHERT
		BASEMENT	BASEMENT

Figure 32. Amplitude spectra at ranges 10 and 1100 km for two crustal models consisting of a thin (250 m) layer of sediments overlain by 5.4 km of fluid and above either a basement or 100 meters of chert and a basement. The source, a vertical point force, and the receivers are at the sea floor.

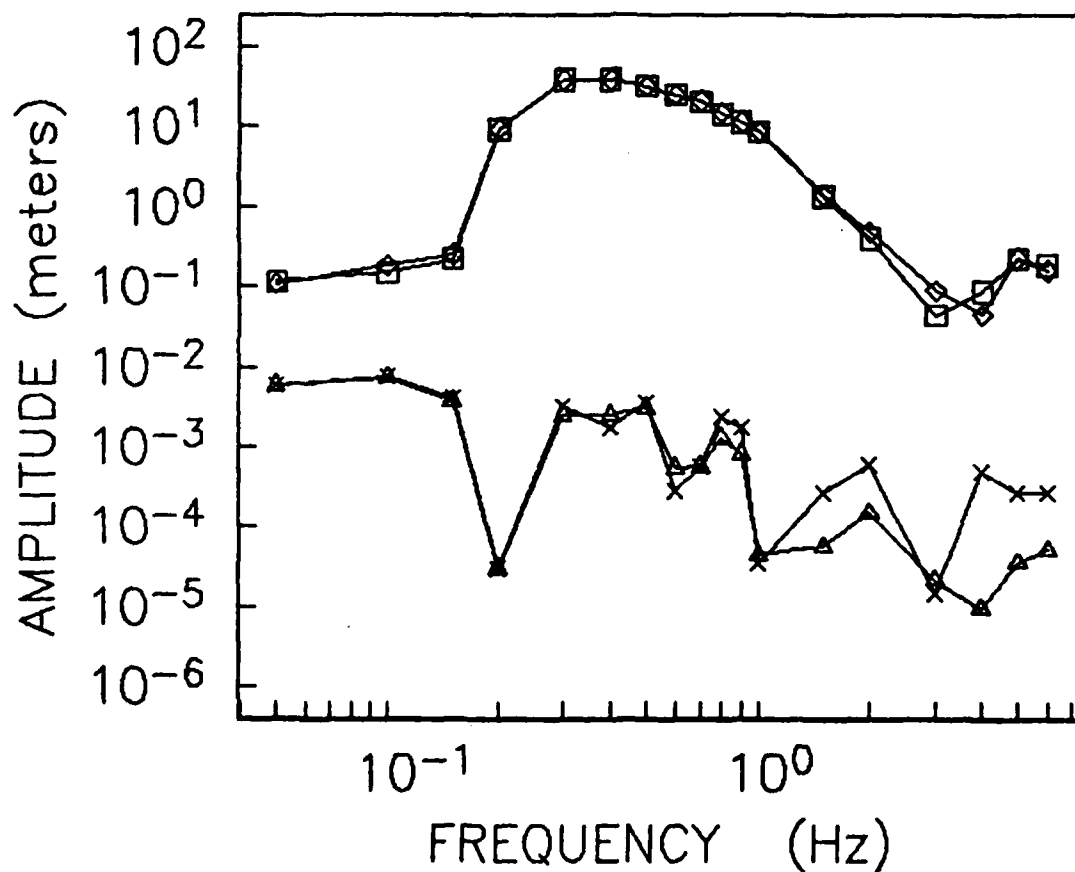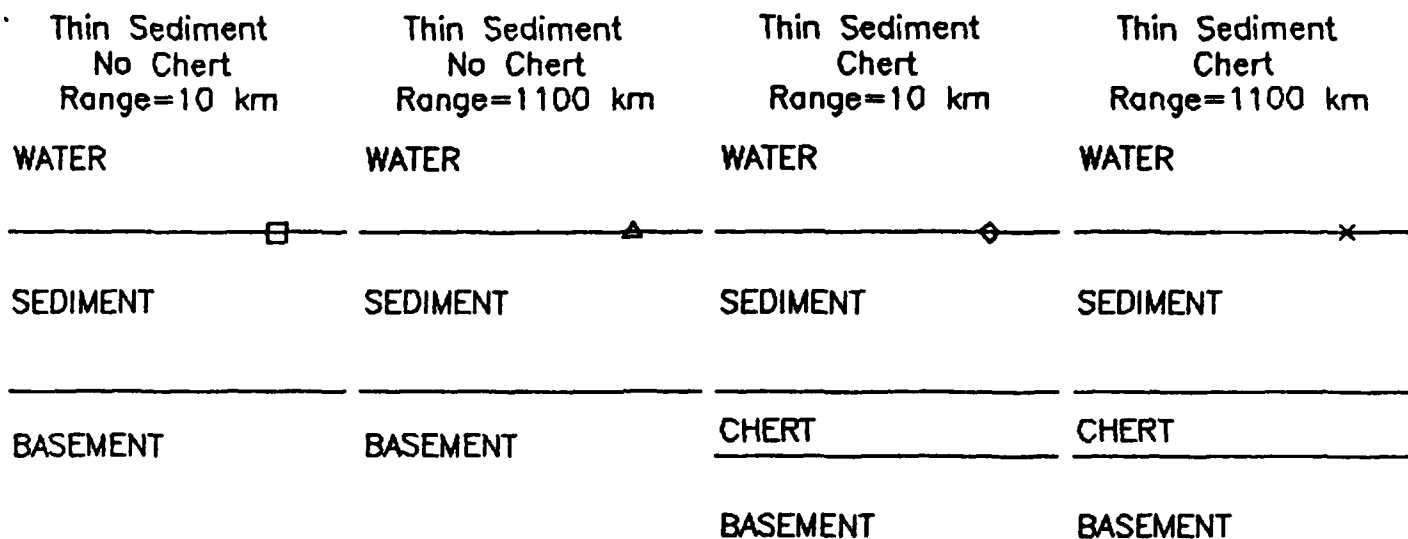| Thin Sediment No Chert Range=10 km	Thin Sediment No Chert Range=1100 km	Thin Sediment Chert Range=10 km	Thin Sediment Chert Range=1100 km
WATER	WATER	WATER	WATER
SEDIMENT	SEDIMENT	SEDIMENT	SEDIMENT
BASEMENT	BASEMENT	CHERT	CHERT
		BASEMENT	BASEMENT
□	△	◇	×

Figure 33. Amplitude spectra at ranges 10 and 1100 km for two crustal models consisting of a thin (250 m) layer of sediments overlain by 5.4 km of fluid and above either a basement or 100 meters of chert and a basement. The source is a vertical point force at the sea floor and the receivers are 300 meters below the sediments, in the basement.

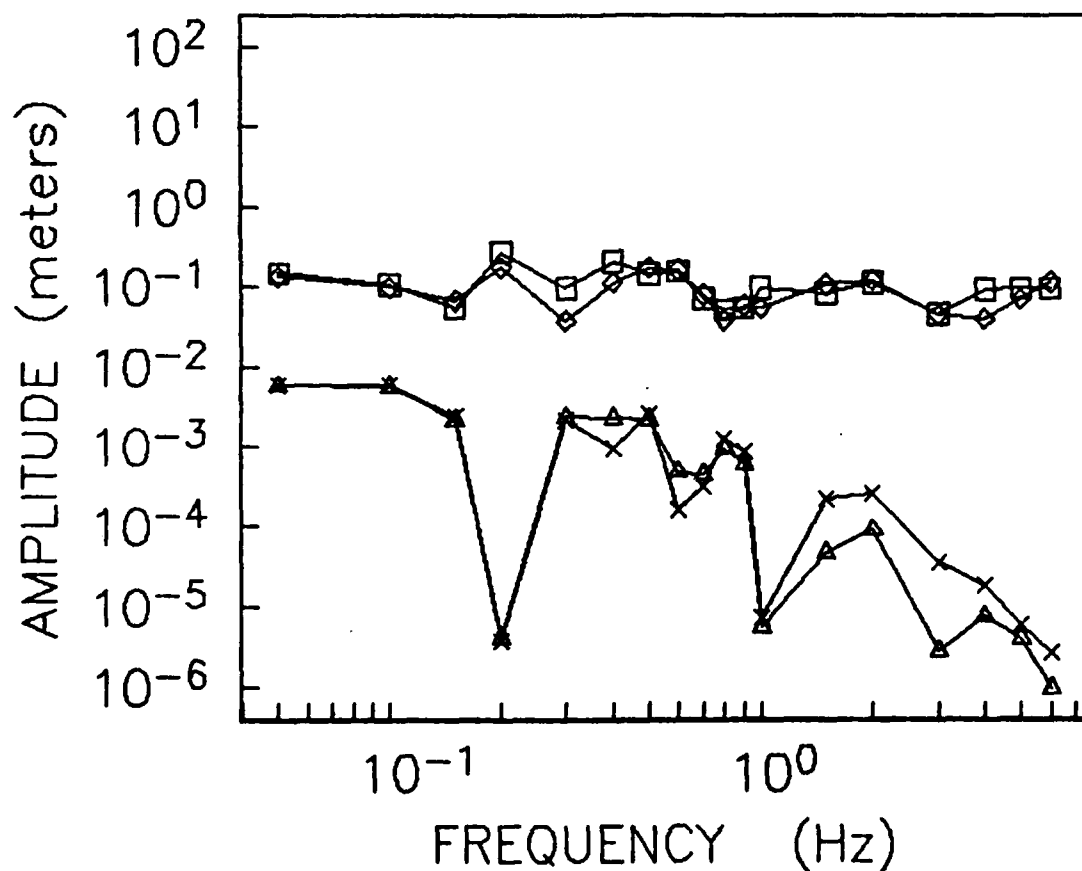| Thick Sediment No Chert Range=10 km	Thick Sediment No Chert Range=1100 km	Thick Sediment Chert Range=10 km	Thick Sediment Chert Range=1100 km
WATER	WATER	WATER	WATER
—□—	—△—	—◇—	—×—
SEDIMENT	SEDIMENT	SEDIMENT	SEDIMENT
BASEMENT	BASEMENT	CHERT	CHERT
		BASEMENT	BASEMENT

Figure 34. Amplitude spectra at ranges 10 and 1100 km for two crustal models consisting of a thick (400 m) layer of sediments overlain by 5.4 km of fluid and above either a basement or 100 meters of chert and a basement. The source, a vertical point force, and the receivers are at the sea floor.

Thick Sediment No Chert Range=10 km	Thick Sediment No Chert Range=1100 km	Thick Sediment Chert Range=10 km	Thick Sediment Chert Range=1100 km
WATER	WATER	WATER	WATER
SEDIMENT	SEDIMENT	SEDIMENT	SEDIMENT
BASEMENT	BASEMENT	CHERT	CHERT
		BASEMENT	BASEMENT

□   △   ◇   ×

Figure 35. Amplitude spectra at ranges 10 and 1100 km for two crustal models consisting of a thick (400 m) layer of sediments overlain by 5.4 km of fluid and above either a basement or 100 meters of chert and a basement. The source is a vertical point force at the sea floor and the receivers are 300 meters below the sediments, in the basement.
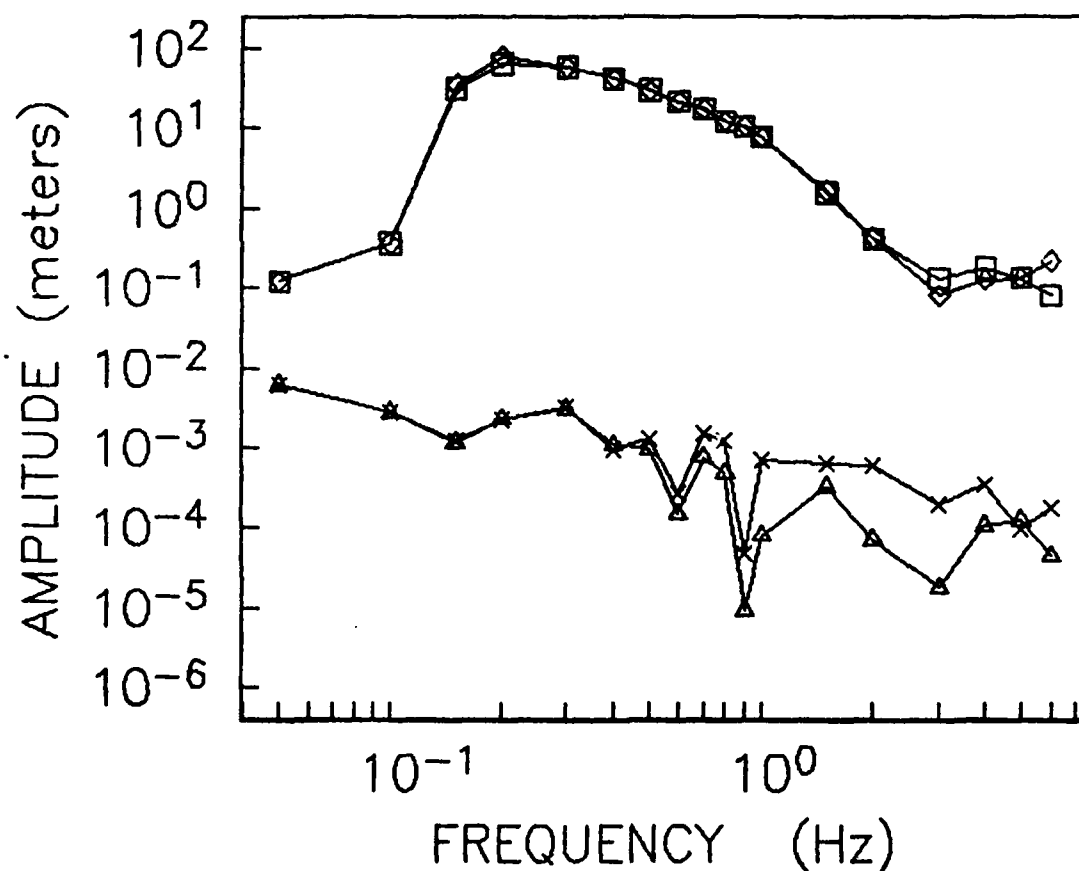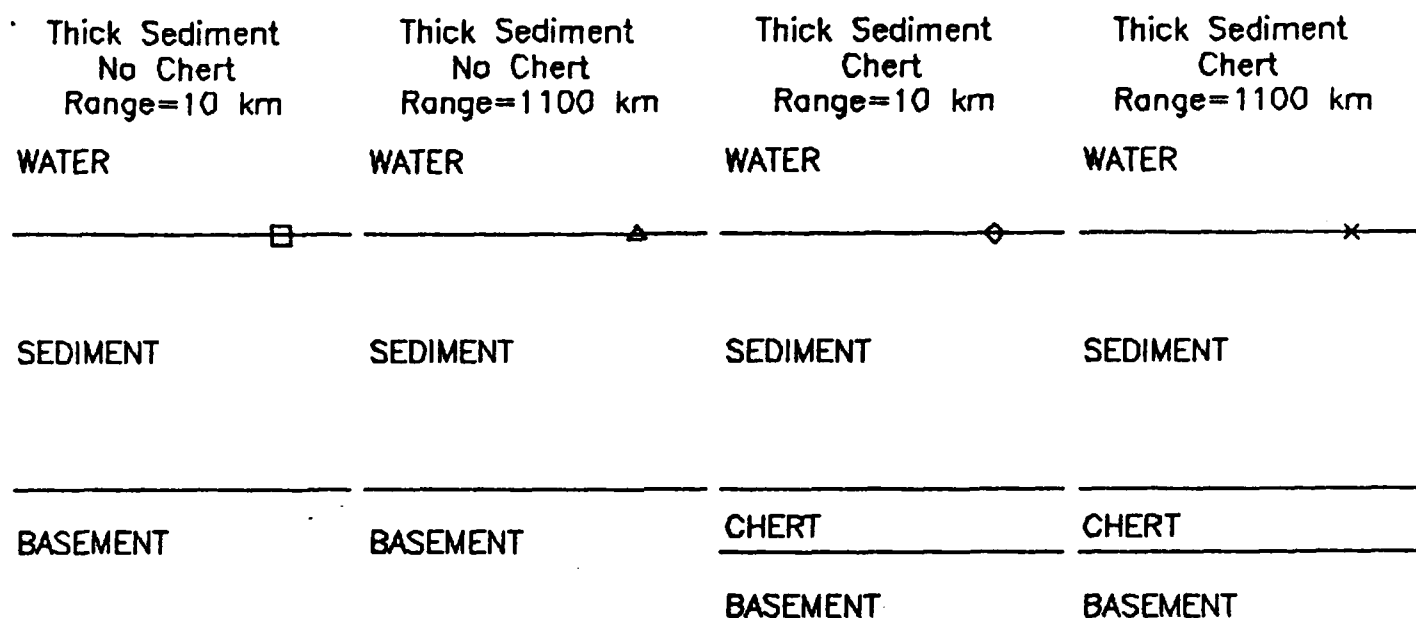
CHAPTER II

ANALYSIS OF AMBIENT SEISMIC NOISE RECORDED BY
DOWNHOLE AND OCEAN BOTTOM SEISMOMETERS ON
DEEP SEA DRILLING PROJECT LEG 78B

RICHARD G. ADAIR
JOHN A. ORCUTT
THOMAS H. JORDAN

II.1. Introduction

The measurement of ambient seismic noise near the sea floor is requisite to formulating optimal strategies for the deployment of marine seismometer systems. There are, however, no published studies of noise within the oceanic crust, and few of noise at the sea floor, especially of reliable, absolute noise levels. Most available measurements were made during the VELA Uniform Project sponsored by the Advanced Research Projects Agency in the 1960's. It was hoped that noise levels at the sea floor would be comparable to those on land (Prentiss and Ewing, 1963), but in fact they were found to be significantly higher (Bradner and Dodds, 1964; Schneider and Backus, 1964; Schneider et al., 1964; Latham and Sutton, 1966; Latham and Nowroozi, 1968). These studies suggest that the noise propagates as an evanescent wave (Stoneley wave) trapped near the ocean bottom-sea floor interface (Bradner et al., 1965; Latham and Sutton, 1966; Latham and Nowroozi, 1968), and thus reduced noise levels are expected within the oceanic crust. The technology and expertise needed to implant instruments in the sea floor has only recently developed, primarily through the Deep Sea Drilling Project (DSDP). Borehole seismometers have been used in oblique seismic experiments on several DSDP legs (Stephen, 1980; Stephen et al., 1981; Stephen, 1982), but the data are not suited for the quantitative analysis of seismic noise. A downhole seismometer system sponsored by the Defense Advanced Research Projects Agency, the Marine Seismic System (MSS), was deployed in Hole 395A (Figure 1) during Leg 78B with the intent of recording high-quality noise and seismic data. This paper presents the first quantitative characterization of ambient seismic noise within the oceanic crust. In addition, a direct comparison of noise characteristics at and below the sea floor is made using data collected on a proximate ocean bottom seismograph (OBS) (see Figure 1).

II.2. Instrumentation and Operations

The borehole instrumentation of the MSS consisted of state-of-health sensors and two vertical-component, short-period seismometers (Teledyne Geotech model S-700'), one configured approximately 50 cm below the other. Each seismometer's output was split into three channels and the gains of the resultant six channels were staggered with overlap to yield a dynamic range

of 144 dB (Figure 2). The data streams were filtered to prevent aliasing, digitized at 75 samples per second using a 10 bit digital word, and transmitted via cable to a shipboard recorder. The cable was also used to recover the borehole instrumentation package. The computed displacement response for the combined seismometer and filter stages is shown in Figure 3. The response is peaked near 11 Hz, and rolls off at 12 dB/octave towards lower frequencies and at 15 dB/octave to the Nyquist frequency.

The borehole package was lowered from *Glomar Challenger* to a depth of 609 meters in Hole 395A (517 meters within the basement), where cave-ins blocked access to the bottom 42 meters. The package was in place for 29.5 hours but data were recorded only during the final 26 hours, which included a refraction experiment (see Figure 4). Although the seismometers were not clamped in the hole, the adjacent unfractured and massive wall rock doubtlessly promoted proper coupling. (The wall rock character was inferred from caliper and acoustic reflection logs conducted earlier during Leg 78B.) Ship motions conveyed to the package were quelled with 0.7 km of slack cable payed out on the sea floor. Noise samples were recorded between refraction shots and during breaks in the refraction experiment, both intentional and unintentional (when explosives failed to detonate). The times of relevant operations and events are charted in Figure 4.

Four triaxial ocean bottom seismographs (OBS's) were dropped from USNS *Lynch* by the group from the University of Texas (UT) Institute of Geophysics. Each OBS was programmed to record 40 seconds of digital data with a sampling interval of 8.352 milliseconds during refraction shots and the intentional shooting hiatus. The OBS seismometers were 10 Hz Mark L6 geophones. The OBS displacement response (Figure 3) increases with frequency at 18 dB/octave up to 10 Hz, and 6 dB/octave thereafter. A variety of malfunctions prevented data recovery except from the vertical component of an OBS located approximately 1-2 km west of the borehole (see Figure 1 for launch point). A more precise location based on water wave arrivals is not possible because recordings of explosion signals but not of noise were severely clipped by frame resonances above 10 Hz. Eleven 34-second samples of noise were obtained from the OBS data.

II.3. Data Quality

Intrinsic earth noise was distinguished from instrument and ship noise on the basis of temporal and spectral characteristics. Spectral characteristics were determined from power densities and coherences computed in a manner described by Welch (1967). Time series were broken into segments which were 'de-meaned', tapered with a normalized Hanning window, and Fourier transformed. Auto- (power) and cross-spectra were averaged (stacked) to reduce spectral estimate variance. Stable estimates were generally achieved with stacks of eight segments, although as many as twenty-four segments were used when available.

Of the six MSS data channels (see Figure 2), only three were usable for noise analysis (L1, U2, L2); the highest-gain channel (U1) was always clipped, and the two of lowest gain (U3, L3) were dominated by least-count noise. An example of MSS data from Channel L1 is shown in Figure 5. Typically, the data were dominated by monotonous, 1-4 second energy while equally persistent high frequency energy (> 10 Hz) was of much lower amplitude. Features in Figure 5 which are attributed to instrument noise or not considered to represent ground motion are the dropped bit near 11.5 seconds; the frequent, random, unidirectional (sensor mass up) transients of variable magnitude (e.g. near 10.5 seconds); and the truncated, low-frequency peak centered at 6 seconds (a rare event). Single, dropped bits, clearly due to instrument errors, were replaced with linearly-interpolated values. High-frequency amplitudes and occurrence rates of the transients generally decreased with time, while the low-frequency amplitudes increased. Power densities of MSS data and instrument noise are shown in Figure 6. The data were eight 13.65 second samples from Channel L1 not corrected for instrument response. Electronics noise levels, available only for frequencies greater than 0.3 Hz, were estimated from RMS noise power values of one-half octave bandwidth provided by Teledyne Geotech. The least-count noise level is that expected from uniformly-distributed errors due to the representation of a continuous variable by a finite, digital word (e.g., Otnes and Enochson, 1972). Neither of these sources of instrument noise dominated above 0.3 Hz. Least-count noise became increasingly important at frequencies where the instrument response rolled off and resulted in diminished coherence of energy between the two

MSS seismometers. Power densities at frequencies below 0.16 Hz are inferred to be dominated by instrument noise on the basis of low coherence (Figure 8).

The transients seen in Figure 5 are assumed to be due either to movement of the unclamped borehole package or to pressure impulses caused by the escape of the casing gas (helium). The transients strongly resemble the MSS response to a step in displacement (Figure 7) and are taken as such for the purpose of determining power densities. The transients were modeled as a compound Poisson process (Appendix II), and their predicted power density $P(f)$ at frequency f is

$$P(f) = 2\lambda < \alpha^2 > \ |H(f)|^2$$

where λ is the mean rate of transient occurrence, $< \alpha^2 >$ is the mean squared amplitude, and $H(f)$ is the Fourier transform of a transient of unit amplitude. λ and $< \alpha^2 >$ were estimated for the data whose power densities are shown in Figure 6 and the resulting P(f) is plotted in the same figure as the curve labeled 'Transient Noise'. The remarkably close agreement between the observed and predicted noise levels implies that energy beyond the break in power density slope (near 2.2 Hz) is concentrated almost entirely in the transients.

System noise levels are not known for the OBS, nor can coherences be estimated since only the vertical component of one instrument was functional. Frequencies at which instrument noise dominated were qualitatively determined from uncorrected power densities (Figure 9). The OBS frame resonance is dominant between 10 and 25 Hz, and the essentially flat portions of the spectrum beyond 4 Hz and below 0.18 Hz imply instrumental sources of white noise. In addition, estimate stability could not be achieved below 0.18 Hz with the available time series lengths.

Ship-generated acoustic signals undoubtedly contributed to local microseismic noise. Sources aboard *Challenger* include machinery and the dynamic positioning system. The dynamic positioning system was silenced only once during the MSS deployment (0104-0120Z, 29 March), but as this was prior to the start of data recording, a quantitative assessment of its effects is not possible. Unpublished ocean bottom noise spectra estimated from data collected on Scripps Institution of Oceanography OBS's suggest that noise caused by nearby ships is significant only above

approximately 5 Hz and is typically manifested as sharp peaks at a few frequencies and several of their higher harmonics. The high noise levels above 10 Hz on the UT OBS may be, at least in part, attributed to ship noise amplified by frame resonances.

Another possible noise source of is the flow of water past the instruments (Duennebier et al., 1981). This noise is thought to be generated when current speeds are in excess of 10 cm/sec, but there is a complex dependence on body geometry. In the simple case of a cylinder, the frequency of the noise is inversely proportional to the diameter; the whip antenna on the OBS would have a flow-noise frequency of about 6 Hz for a current speed of 10 cm/sec. Near-bottom current measurements (5 meters above the sea floor) were made approximately 4 km north of the UT OBS during the period 28 March-1 April (Boyd, this volume). The average current speed was 4.4 cm/sec and the maximum was 8.9 cm/sec, so it is likely that current noise is not significant for the OBS noise observations. In the case of the MSS, temperature observations indicate that water flowed down the hole at the rate of 25 m/hr and had disappeared into the basement within 500 meters sub-bottom, 100 meters above the borehole instrument package. Also, there was no evidence for hydrothermal circulation anywhere in the hole. Hence, water flow is not thought to be a large contributor to MSS noise measurements. Thus, we feel the MSS data reliably represent intrinsic earth noise in the band 0.16-2.2 Hz, while the OBS data probably do so between 0.18 and 4 Hz.

II.4. Discussion

While stability of noise estimates computed from 44 minutes of MSS data implies quasi-stationarity on the time scale of one hour, recorded amplitudes increased enough over one day to cause clipping on the channel of highest usable gain (L1). On the time scale of ten hours, power densities, computed from Channel U2 data, were stable in shape but increased by up to 5 dB (Figure 10). Displacement spectra were peaked between 0.2 and 0.3 Hz and decreased with frequency at 80 dB/decade. The earliest of the spectra in Figure 10 had a peak value of 4×10^6 nm^2/Hz at 0.21 Hz and fell from 1×10^6 nm^2/Hz at 0.33 Hz to 1 nm^2/Hz at 1.9 Hz. A more detailed study of the temporal noise variation was conducted using integrated, uncorrected power

- 17 -

densities from Channel U2 (which was not clipped by noise) as a measure of level (Figure 11b). The power densities were computed from 13.65 seconds of data sampled at approximately 15 minute intervals; these realizations of power were smoothed with a three-point running mean. A trend of increasing noise levels is clearly discernible in Figure 11b. This variability of ocean bottom noise may be caused by changes in local sea state and/or weather (Latham and Sutton, 1966; Latham and Nowroozi, 1968). Using bi-hourly observations recorded in *Challenger's* deck log, only swell height (Figure 11a) was strongly correlated with noise level. The (nonlinear) interaction between opposing swell produces significant pressure fluctuations on the sea floor at half the swell period (Longuet-Higgins, 1950; Kadota and Labianca, 1981), and, indeed, the reported swell period of 10 - 11 seconds is approximately twice that of the spectral peak between 3 and 5 seconds (Figure 10). However, a more definite conclusion is not justified by the limited data set use here. The period of the noise peak is within the range of the so-called "microseism peak" of noise observed at the ocean bottom (Latham and Sutton, 1966; Latham and Nowroozi, 1968) and on continents (Melton, 1976), where, in the latter instance, there is ample evidence ascribing the microseism peak to the nonlinear swell interaction (Haubrich et al., 1963; Haubrich and McCamy, 1969).

The detailed, temporal behavior of noise at the sea floor during the MSS deployment cannot be reliably determined because of the paucity of appropriate OBS data. However, simultaneous noise observations were made by the two seismic systems on eleven occasions, nine of which may be used for comparison (Figure 4). Six of these were recorded over a 75-minute period scheduled specifically for noise study and afford stable, high-resolution spectral estimates (Figure 12). In the band of overlap (0.18-2 Hz), noise levels were higher at the sea floor than in the borehole by an amount which increased with frequency from 10 dB at 0.2 Hz to 28 dB at 2.2 Hz. This is consistent with the notion that, at these frequencies, microseismic noise propagates primarily as fundamental-mode Stoneley waves (Latham and Sutton, 1966; Latham and Nowroozi, 1968; Brandner and Dobbs, 1964; Bradner et al., 1965; Tuthill et al., 1981). A large acoustic-shear impedance mismatch at a fluid-solid interface results in the severe exponential decay of this wave

away from the interface, essentially trapping the seismic energy (Latham and Sutton, 1966; Tuthill et al., 1981). Site 395 is a ponded depression in the midst of rugged bathymetric relief (Figure 1), which may affect seismic amplitudes in complex ways, but if the sediments are the dominating influence at this site, Stoneley-wave amplitudes at frequencies above that of the microseismic peak should be significantly lower below the base of the sediments than at the sea floor.

The remaining five noise windows were widely spaced in time and were intended to be for explosion signals, but the shots failed to detonate; only three may be used for comparison because of excessive instrument noise on the MSS. Sea floor noise levels were 10-30 dB higher than in the borehole for these samples, as well. (The power densities of Figure 13 were of similar resolution and variance: the MSS data were eight 6.83-second samples and the UT OBS data were eight 4.28-second samples.)

Representative extrema of microseismic noise levels observed during the ten years of the Scripps Institution of Oceanography's OBS program are compared in Figure 14 with the lowest, reliable levels observed during Leg 78B. The SIO OBS's employed 1-Hz digitally recorded seismometers (Prothero, 1974; Moore et al., 1981). Power densities were computed from the vertical-component output which resided in semiconductor memory prior to being buffered to tape and thus were not contaminated by the mechanical tape-recorder noise. Data for the 'noisiest site' were fifty-one, 8-second samples collected southeast of Hawaii, and those for the 'quietest site' were thirty-four, 4-second samples collected on the East Pacifc Rise near 20° N. The extrema are separated by 20-30 dB. The UT OBS values are similar to the SIO OBS maxima while the MSS values are intermediate to low.

Continental noise observations are compared with the MSS spectrum in Figure 15. The Queen Creek data were recorded in a mine in Queen Creek, Arizona (Melton, 1976), and the Lajitas data were recorded at a site near Lajitas, Texas (Herrin, 1982). The Brune-Oliver curves represent average and high levels for continental stations, and were taken from Melton (1976), who reanalyzed Brune and Oliver's (1959) summary of published noise observations. MSS levels

the Brune-Oliver curves.

II.5. Conclusions

The noise levels observed by the MSS in Hole 595A, approximately 500 m below the sediment-water interface, were 10-30 dB lower than those recorded by the University of Texas OBS over the frequency range 0.2-2.0 Hz (Figures 12 and 13). This observation is consistent with the hypothesis that seismic noise at these frequencies propagates primarily as low-order Stoneley modes trapped at the sea floor interface (Bradner et al., 1965; Latham and Sutton, 1966; Latham and Nowroozi, 1968; Tuthill et al., 1981). The correlation of the noise levels with swell heights (Figure 11) suggests that the generation of sea-floor noise at this mid-Atlantic site is dominated by local nonlinear ocean wave interactions. To within the accuracy of the deck-log observations, the swell period was approximately twice that of the microseismic noise peak, consistent with the Longuet-Higgins mechanism and previous ocean bottom measurements (Latham and Nowroozi, 1968).

Sea floor noise levels at Site 595 were comparable to the highest values yet observed by Scripps OBS's in the Pacific (Figure 14); hence, even with the reduction achieved by placing the sensor down a borehole, the MSS noise levels are on the order of 30 dB greater that those obtained at quiet continental sites (Figure 15). If the relationship between sea floor and sub-bottom noise spectra seen in Figure 14 is maintained at quieter locations, however, then the down-hole noise levels may be reduced substantially and could compare favorably with typical continental sites.

Future deployments of the MSS using a triaxial set of seismometers and a long-term ocean bottom recording package are planned. Such a system complimented by an array of OBS's should be able to definitively answer questions concering the mode and generation mechanism of micro-seismic noise in the deep ocean.
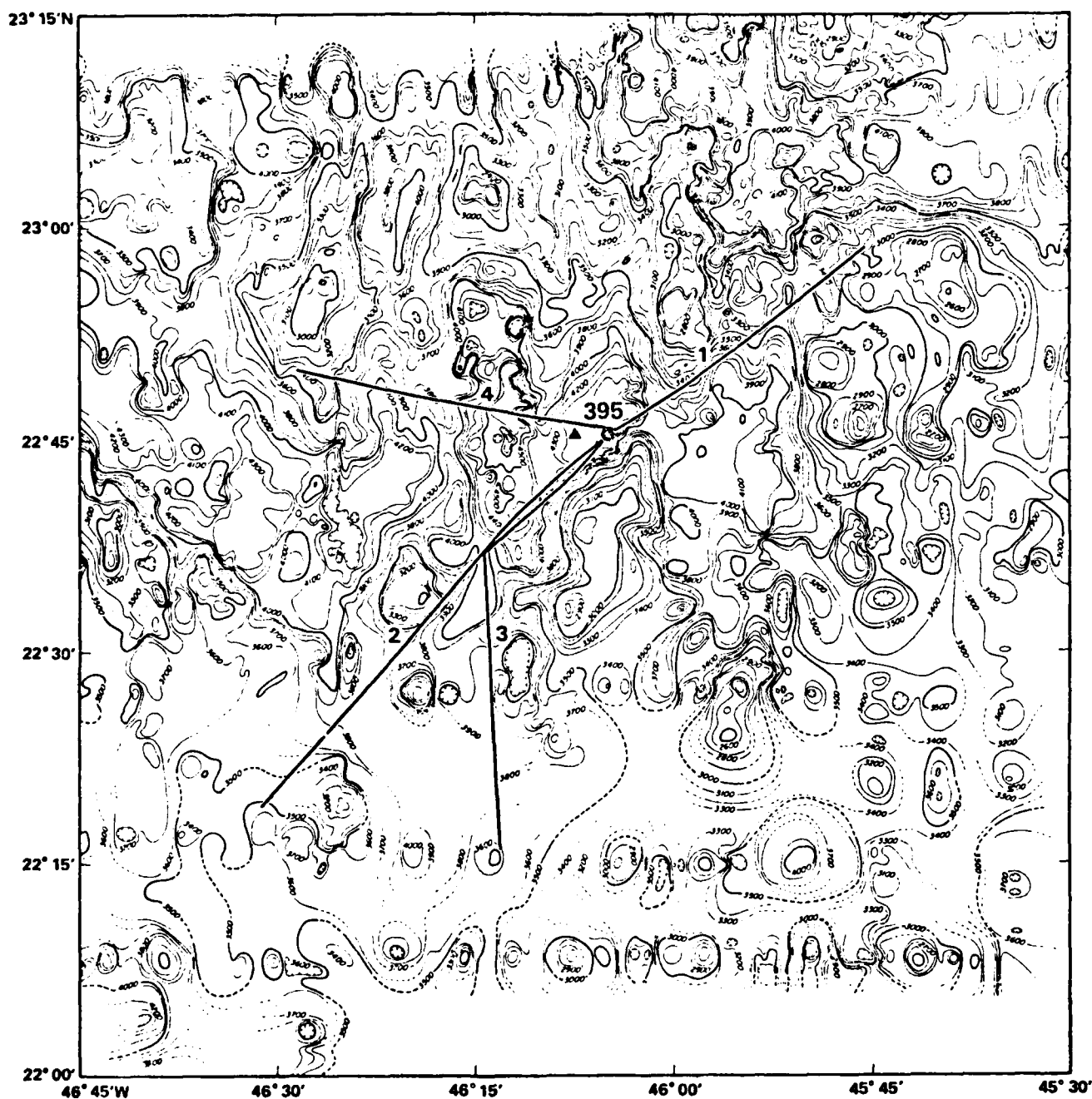
II.6. Acknowledgements

Figure 1. Location of the seismic instrumentation used in the noise experiment. The borehole instrumentation package of the Marine Seismic System (MSS) rested unclamped at the bottom of Hole 395A (22° 45.35′ N ; 46° 04.91′ W), drilled five years earlier on Leg 45. The ocean bottom seismometer (OBS), one of four deployed during Leg 78B, was approximately 1-2 km west of Hole 395A. The OBS launch point is shown (22° 45.50′ N ; 46° 05.43′ W).
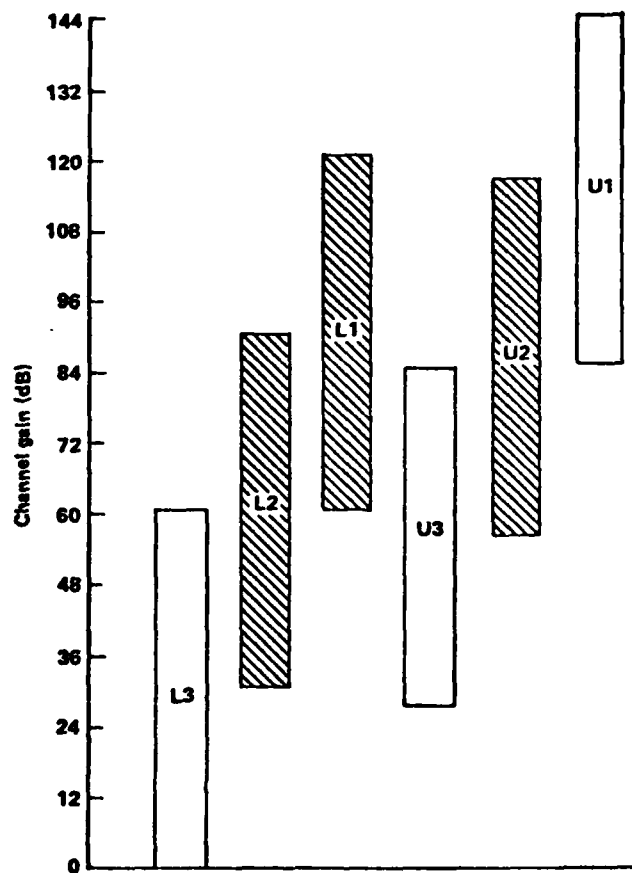
Figure 2. Schematic depiction of the MSS-data channel gains. The outputs of the two vertical-component seismometers, one configured 50 cm below the other, were split into 3 channels each, and the gains of the resultant six channels were staggered to yield 144 dB of dynamic range. 'U' and 'L' refer to the upper and lower seismometers, respectively. The use of a 10-bit, unsigned digital word resulted in a range of 60 dB for each channel. Adjacent channels of a seismometer overlapped by 30 dB and upper seismometer gains were offset from lower seismometer gains by 24 dB.
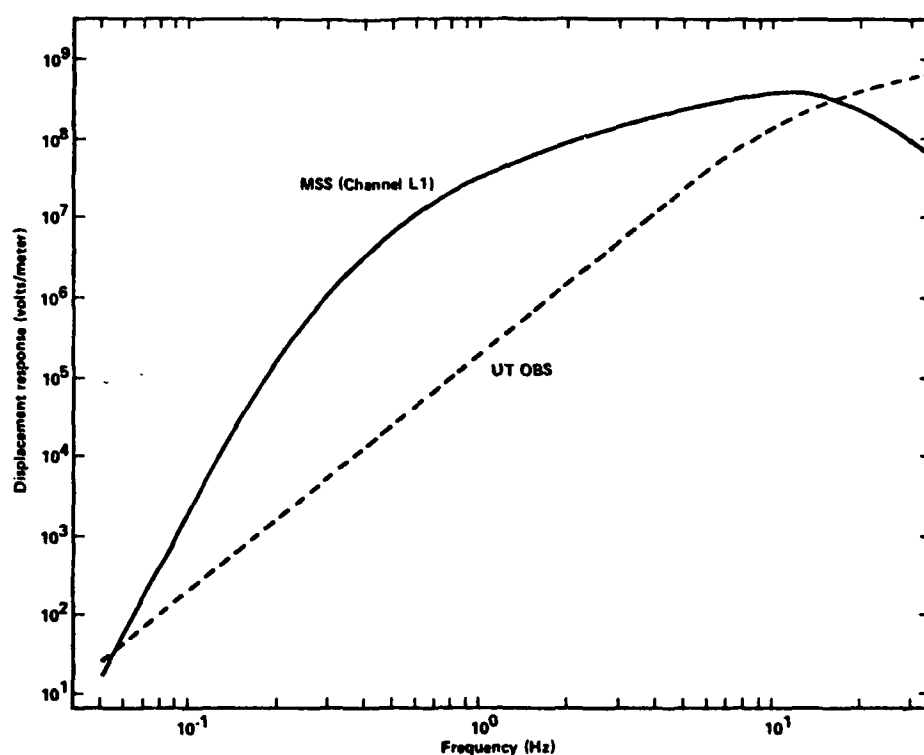
Figure 3. Displacement responses of Leg 78B seismic systems. The MSS employed two vertical-component, short-period, force-feedback, piezoelectric seismometers (Teledyne Geotech model S-700'), whose outputs were filtered to prevent aliasing and then digitized at 75 samples per second. The MSS response is peaked near 11 Hz, and falls at 12 dB/octave towards lower frequencies and at 15 dB/octave to the Nyquist frequency. The University of Texas (UT) ocean bottom seismometer system consisted of a triaxial set of critically-damped, 10-Hz, Mark L6 geophones whose outputs were sampled with an 8.352 millisecond digitizing interval. The UT OBS response increases with frequency at 18 dB/octave up to 10 Hz, and at 6 dB/octave thereafter.
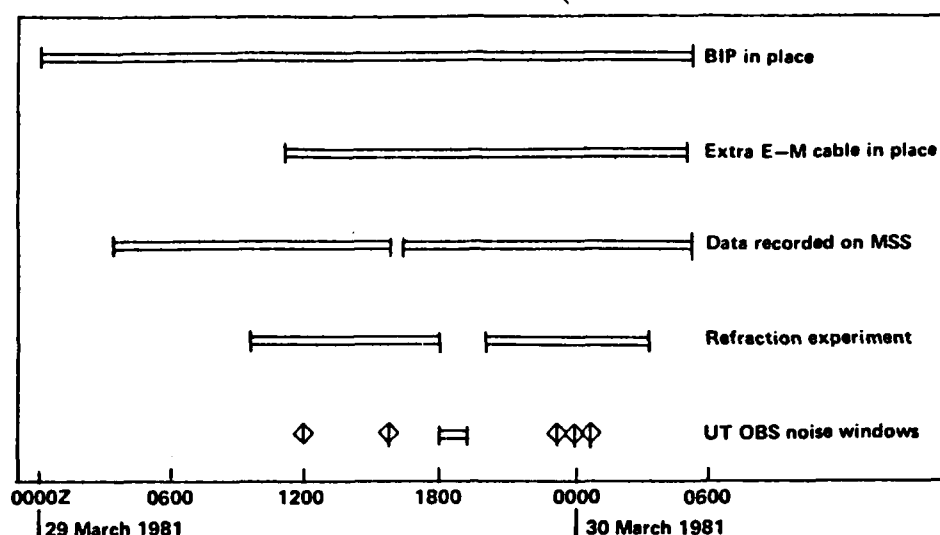
Figure 4. Times of important operations and events during the Leg 78B noise experiment. The borehole instrument package (BIP) first entered Hole 395A at 0257Z, 28 March, 81, but was not in place for the refraction and noise experiments until 0000Z, 29 March. The BIP was recovered at 0512Z, 30 March. The BIP was not clamped in the hole but was isolated from ship motions by 0.7 km of electro-mechanical (E-M) cable payed out on the sea floor at 1100Z, 29 March. Twenty-six hours of data were recorded by the MSS continuously, except for a 35-minute gap beginning at 0545Z 29 March. The refraction experiment commenced at 0925Z, 29 March, and ended at 0220Z, 30 March, and was broken by a two-hour hiatus between 1800 and 2000Z, 29 March, during which the noise experiment was performed. The University of Texas ocean bottom seismograph (UT OBS) recorded eleven 34-second noise samples, six during the noise experiment. The remaining five, denoted by diamonds, correspond to windows when refraction shots failed to explode.
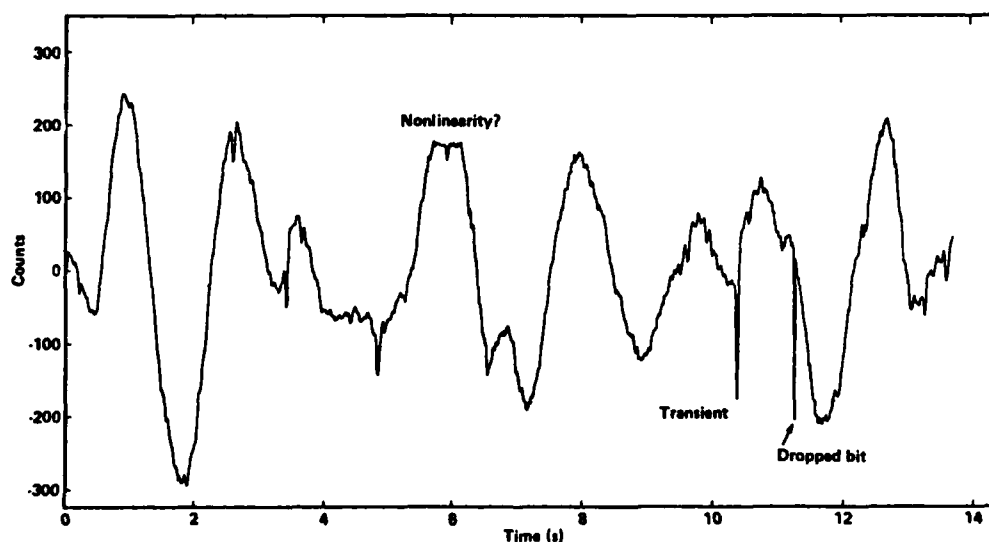

Figure 5. Sample from Channel L1 illustrating characteristics of MSS noise data. Low-frequency (0.2-0.3 Hz) energy dominates the time series. Features which contribute to noise are the dropped bit near 11.5 seconds; the frequent, random, unidirectional transients, such as the one labeled near 10.5 seconds; and the truncated low-frequency peak centered at 6 seconds, the latter possibly be due to an instrument non-linearity. Units are digital counts, and positive amplitude corresponds to upward mass movement.
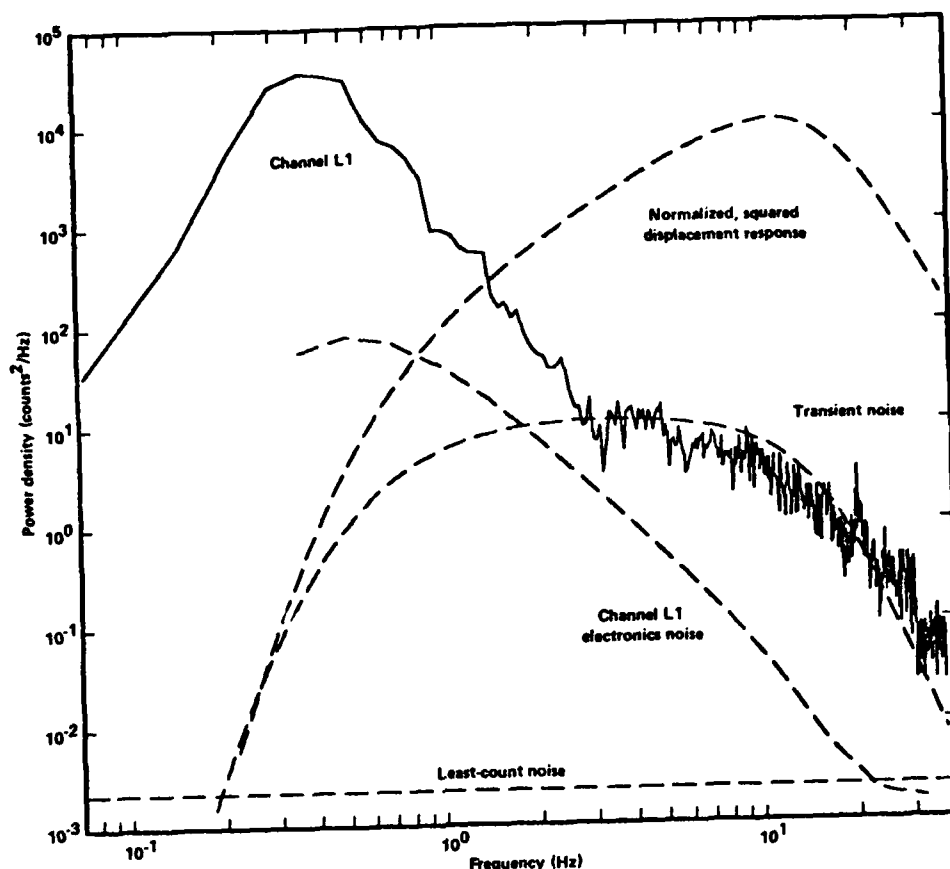
Figure 6. Power spectral densities of MSS data compared with estimates of instrument noise. The data (solid line) were computed from eight 13.65 second samples of Channel L1 with no instrument correction applied. The electronics noise was estimated from RMS noise voltages of 1/2 octave bandwidth provided by Teledyne Geotech. The least-count noise level is that expected from uniformly-distributed errors owing to the representation of a continuous quantity by a finite, digital word. The transient-noise spectrum, which is attributed to the frequent, impulsive features identified in Figure 5, was computed from equation (A24) and defines the high-frequency limit of reliable microseismic noise estimates. Also shown in this figure is the squared, normalized MSS displacement response.
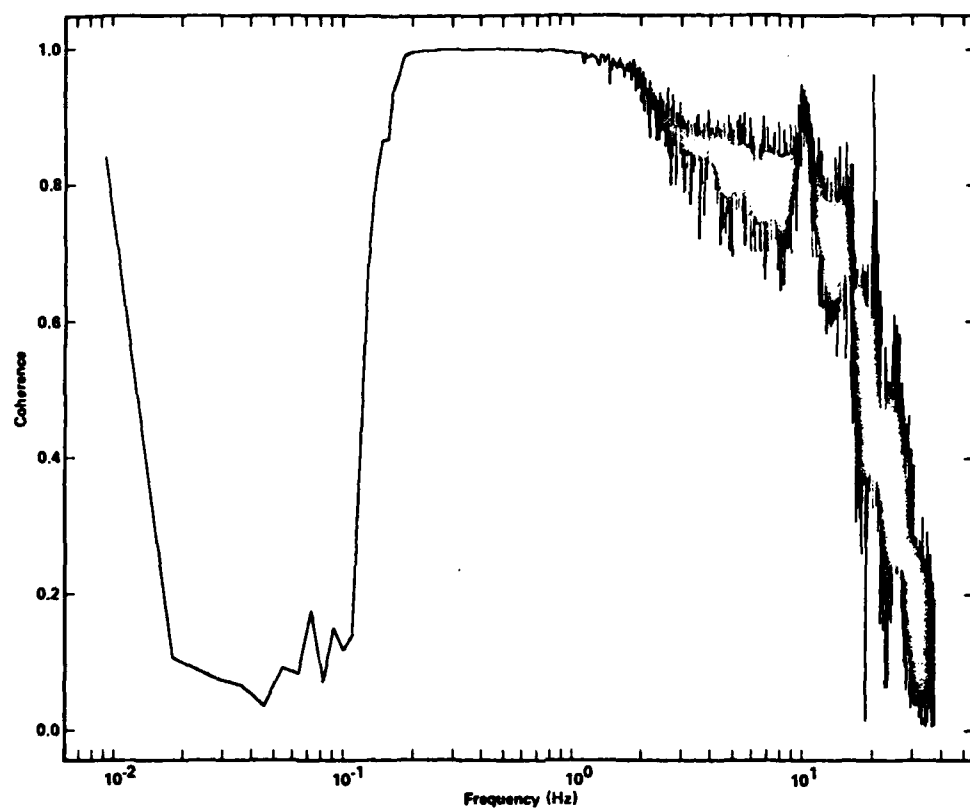
Figure 7. Transient shape compared to the MSS responses to a step and impulse in displacement. The transients observed in the MSS data resemble the former than the latter, and are taken as such for the purpose of computing the transient-noise spectrum shown in Figure 6.
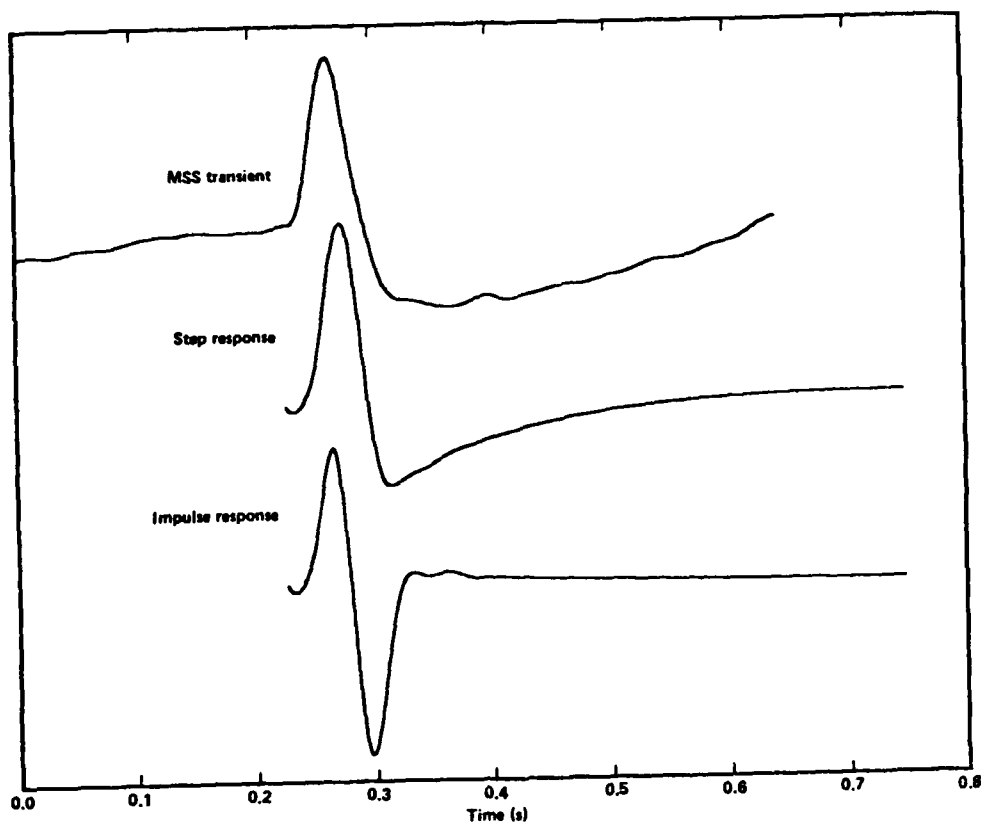
Figure 8. Coherences between the highest usable gain channels of each of the MSS seismometers (L1 and U2). The coherence spectrum was computed from twenty-four 109.2 second samples of each channel. Energy between the two seismometers is highly incoherent below 0.16 Hz, where response roll-off causes instrument noise to dominate.
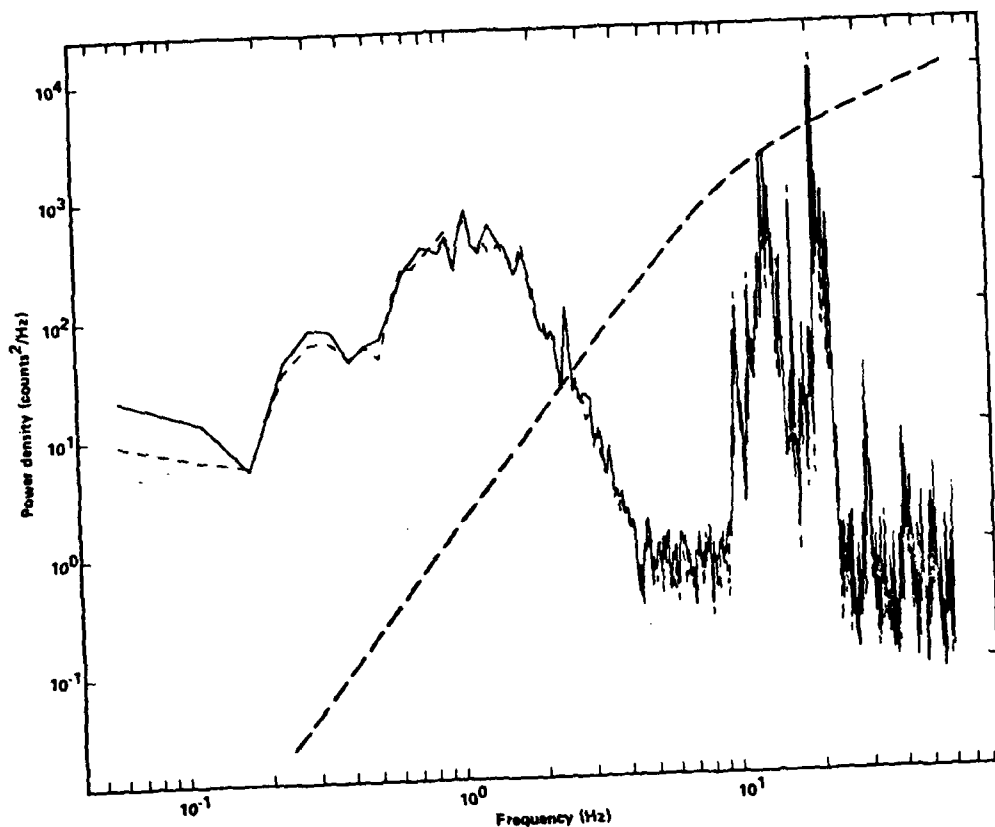
Figure 9. Uncorrected UT OBS power densities. Spectra were computed from eleven 17.1-s segments obtained from six 34.2-s noise samples recorded over a 75 minute period. The large amplitudes between 10 and 25 Hz are possibly ascribable to resonance of the OBS frame, and the flat portions above 4 Hz and below 0.18 Hz are likely imposed by instrument noise. Spectra between 0.18 and 4 Hz are thought to estimate reliably ambient noise levels on the sea floor.
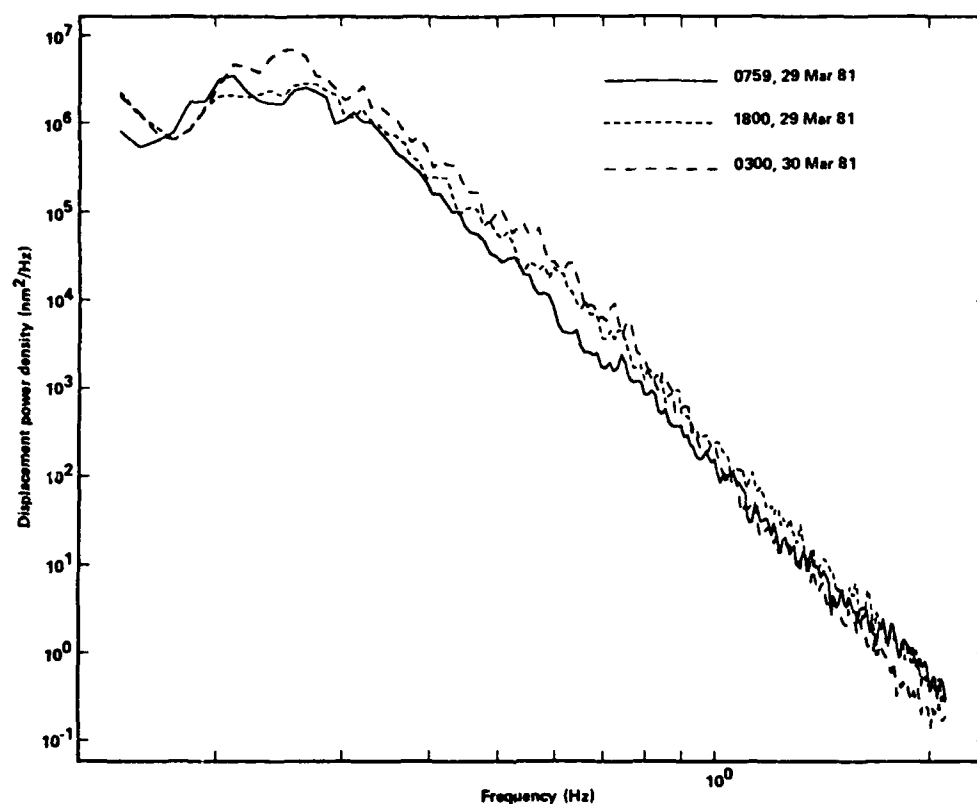
Figure 10. Displacement power densities, in nanometers squared per Hertz, in the Hole 395A at approximately 10 hour intervals. Each curve was computed from twenty-four 109.2-second samples from Channel U2. The spectral shape of the noise was stable over this period but amplitudes increased with time. Power densities fall at approximately 80 dB/decade beyond the peak at 0.2-0.3 Hz.
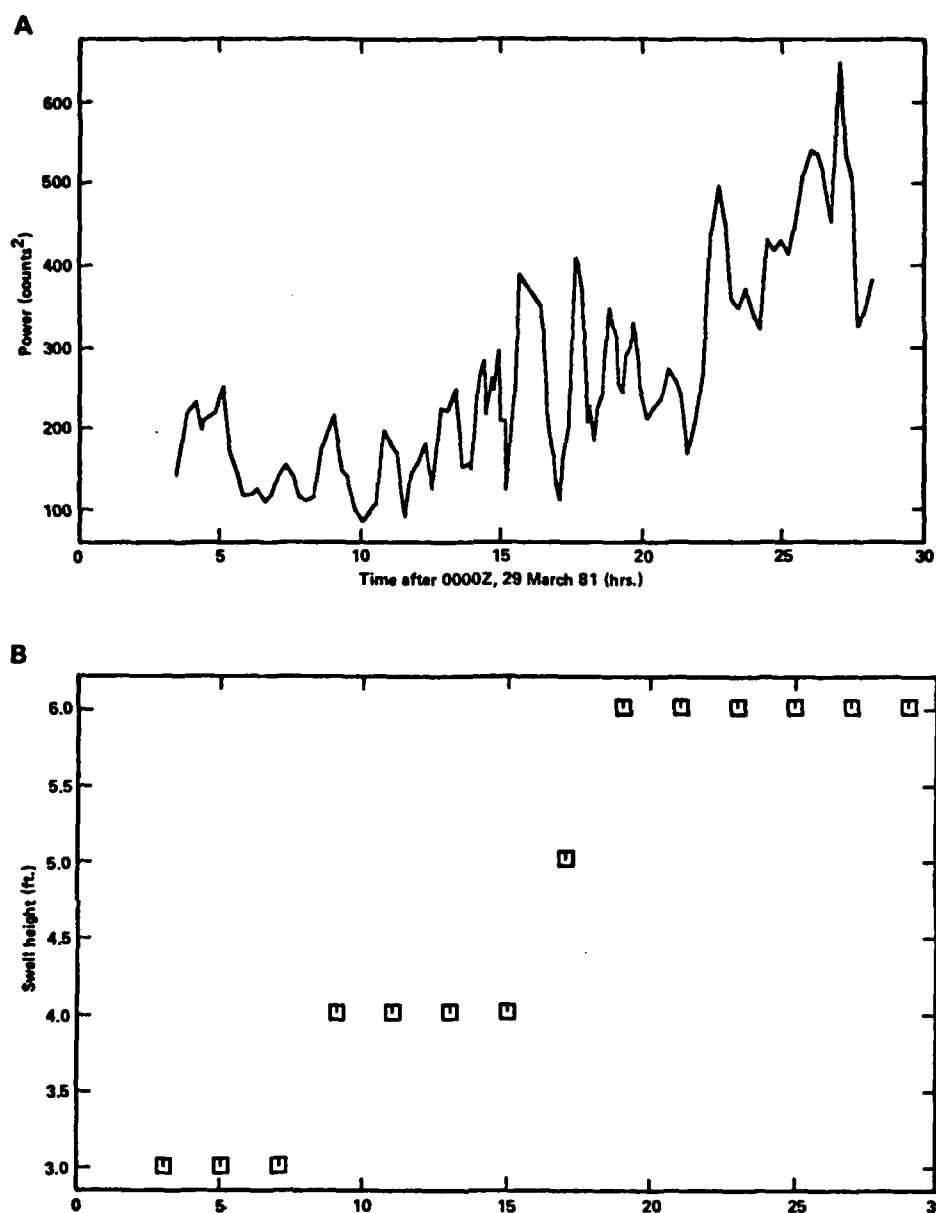
Figure 11. Temporal variation of (a) local swell height and (b) borehole noise levels. The swell height was recorded bi-hourly in the Challenger's deck log. The noise levels was estimated from integrated, smoothed power densities computed from 13.65 seconds of uncorrected Channel U2 data sampled at approximately 15 minute intervals. A three point running mean was applied to the integrated values.
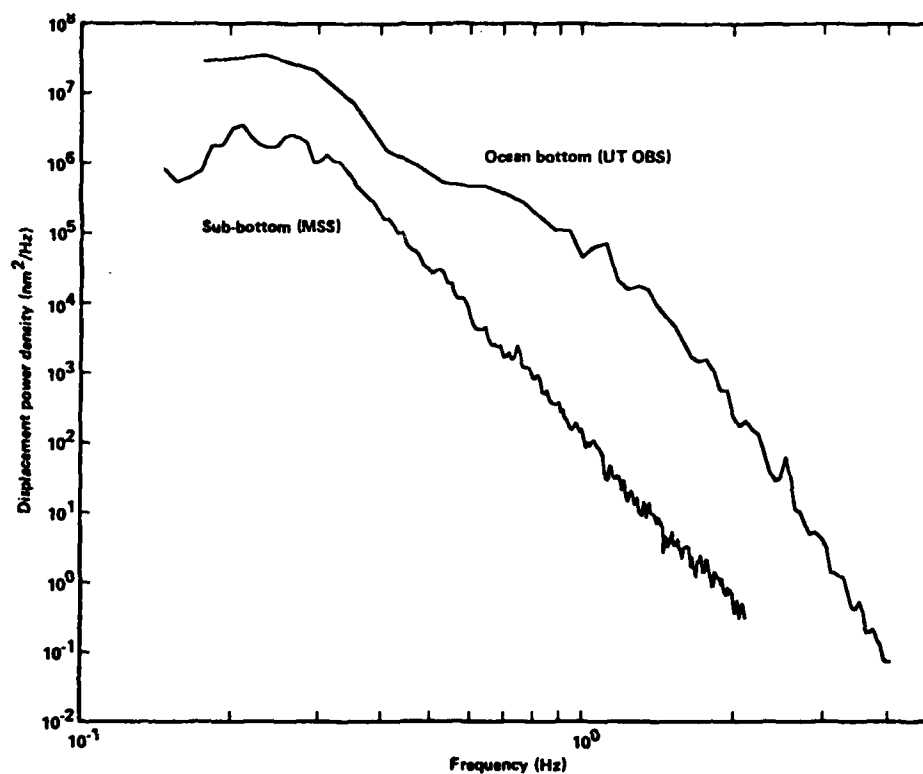
Figure 12. A comparison of ambient seismic noise at and below the sea floor using corrected UT OBS and MSS data recording during the period 1800-1900Z, 29 March, 81. The UT OBS data were six 34.2-s samples, and the MSS data were six 109.2-s samples; the former were broken into eleven 17.1-s segments, and the latter, into eleven of 54.6-s duration.
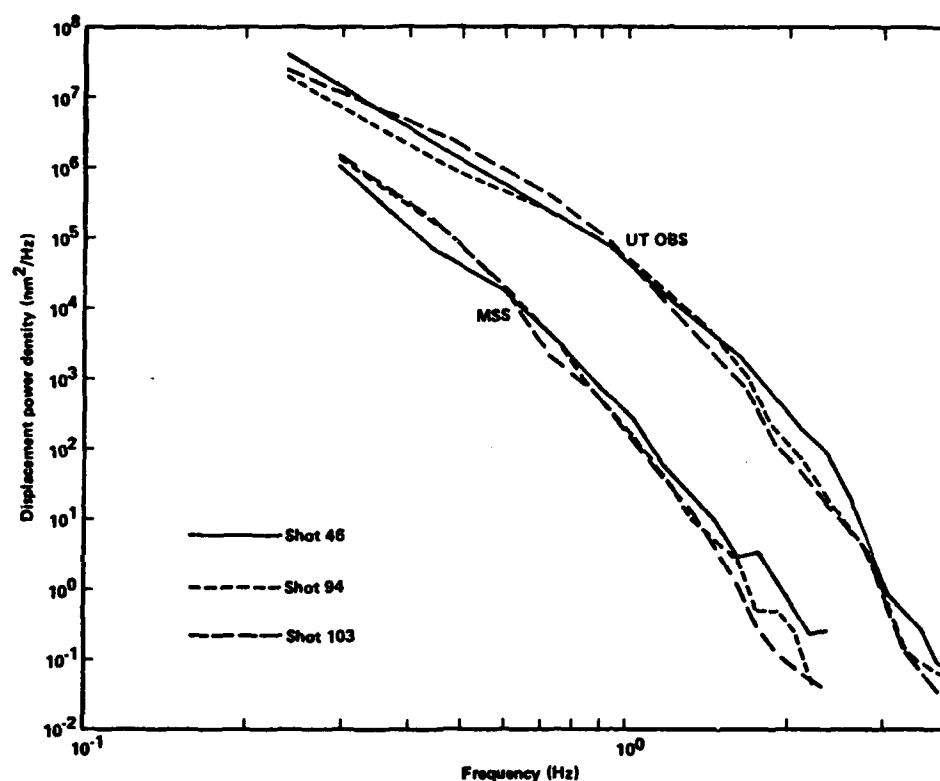
Figure 13. Comparison of corrected UT OBS and MSS noise observations recorded during refraction-experiment windows when shots failed to explode. The upper set of curves were computed from UT OBS data and the bottom from MSS data. The UT OBS was programmed to record a maximum of 40 seconds per event, but in practice only 34.2 seconds of data (4096 samples) were available for analysis. Eight segments of 512 time points are used to calculate estimates for both the UT OBS and MSS data.
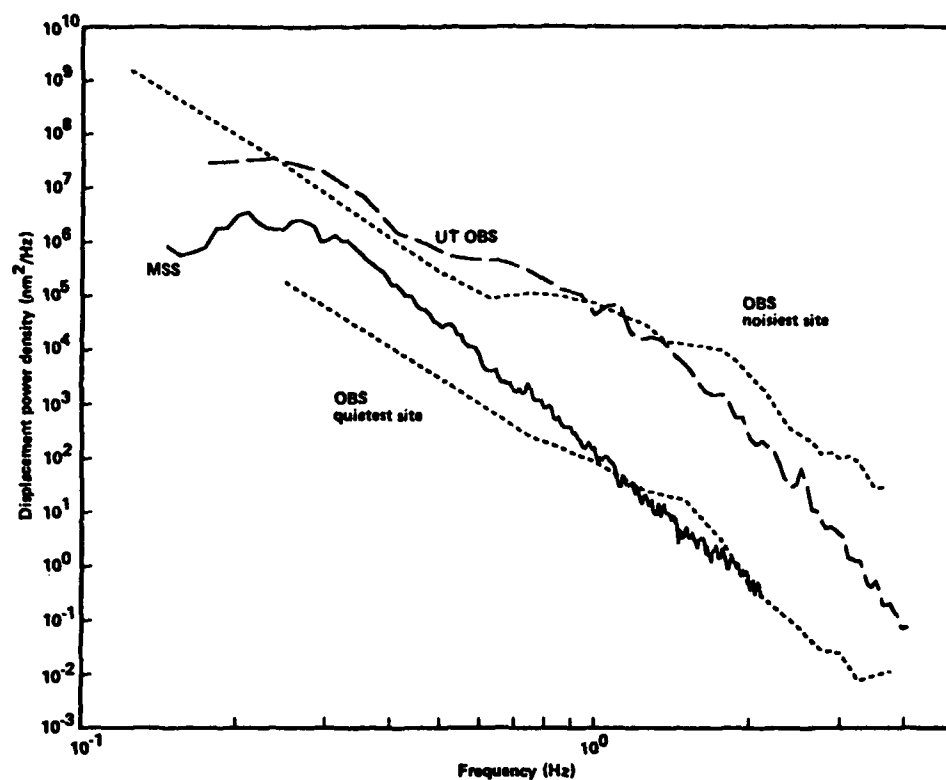
Figure 14. Comparison of Leg 78B noise spectra with OBS observations in the Pacific. The UT OBS data are the same as those in Figure 12, while the MSS data are the earliest (and, therefore, lowest) of those in Figure 10. The two dashed curves are extrema of observations made with the Scripps Institution of Oceanography OBSs. The 'Noisiest Site' was southeast of Hawaii and the data were fifty-four 8-second samples; the 'Quietest Site' was on the East Pacifc Rise and the data were thirty-one 4-second samples.

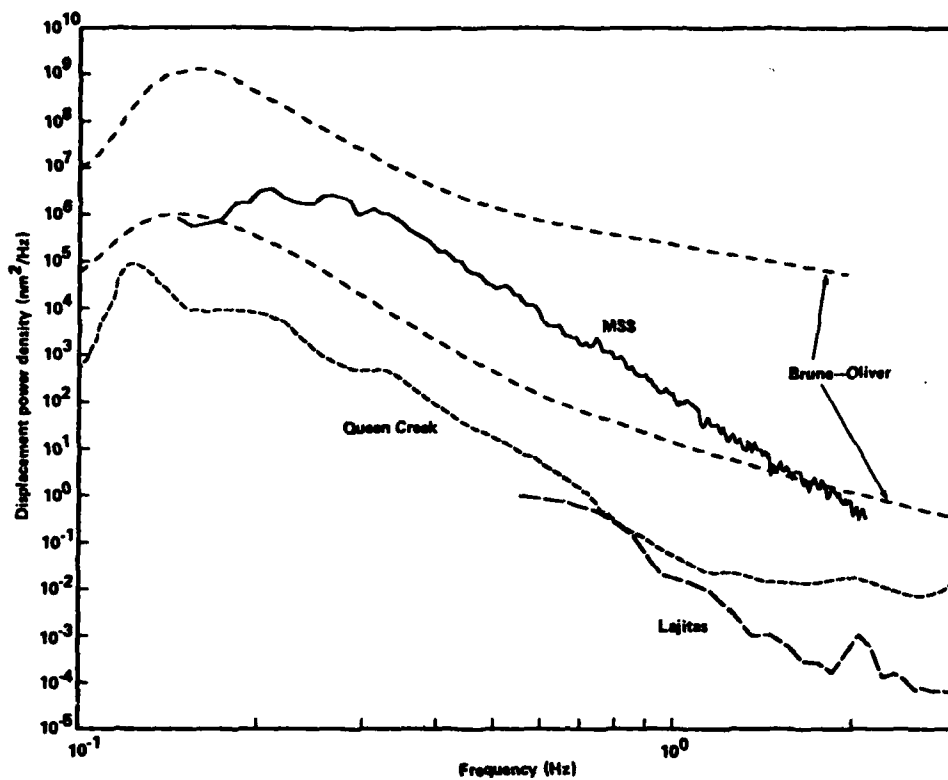Figure 15. Comparison of the sub-bottom noise spectrum at Site 395 with spectra at two quiet continental sites. The Queen Creek, Arizona, curve was taken from Melton (1977), who extracted it from Fix (1972). The Lajitas, Texas, data were recorded at an extremely quiet surface site during a time of low winds (Herrin,1982).

References

Aki, K. and P. Richards, "Quantitative seismology," W. H. Freeman and Co., 1980.

Apsel, Randy J., "Dynamic Green's functions for layered media and applications to boundary-value problems," Ph.D thesis, Univ. of California, San Diego, La Jolla, 1979.

Bracewell, Ron, 1965. *The Fourier Transform and Its Application:* New York (McGraw-Hill).

Bradner, H. and Dodds, J. G., 1964. Comparative seismic noise on the ocean bottom and on land, *J. Geophys. Res.* v. 69, p. 4339-4348.

Brandner, H., Dodds, J. G., and Foulks, R. E., 1965. Investigation of microseism sources with ocean-bottom seismometers, *Geophysics,* v. 30, p. 511-526.

Darbyshire, J., 1960. Microseisms, in: Hill, M. N. (Ed.), 1960. *The Sea,* vol. 1, p. 700-719: Wiley-Interscience.

Duennebier, F. K., Blackinton, G., and Sutton, G. H., 1981. Current-generated noise recorded on ocean bottom seismometers, *Mar. Geophys. Researches,* v. 5, p 109-115.

Feller, William, 1968. *An Introduction to Probability Theory and Its Application. Volume I:* New York (John Wiley).

Haubrich, R. A., Munk, W. H., and Snodgrass, F. E., 1963. Comparative spectra of microseisms and swell, *Bull. Seismol. Soc. Amer.,* v. 53, p. 27-37.

Haubrich, R. A. and McCamy, K., 1969. Microseisms: coastal and pelagic sources, *Rev. Geophys.,* v. 7, no. 3, p. 539-571.

Herrin, E., 1982. Seismic instruments used in treaty verification, *Bull. Seismol. Soc. Amer.,* v. 72, p. S61 - S67.

Kadota, T. T. and Labianca, F. M., 1981. Gravity-wave-induced pressure fluctuations in the deep ocean, *IEEE J. Oceanic Eng.,* v. OE-6, no. 2, p. 50-58.

Kennett, B.L.N., "Seismic waves in a stratified half space - II. Theoretical seismograms," Geophys. J. R. Astr. Soc., *61*, 1-10, 1980.

Latham, G. V., and Sutton, G. H., 1966. Seismic measurement on the ocean floor. 1. Bermuda area, *J. Geophys. Res.*, v. 71, p. 2545-2573.

Latham, G. V., and Nowroozi, A. A., 1968. Waves, weather, and ocean bottom microseisms, *J. Geophys. Res.*, v. 73, p. 3945-3956.

Longuet-Higgins, M., 1950. A theory of the origin of microseism, *Phil. Trans. Roy. Soc. London,* v. A243, p. 1-35.

Melton, B. S., 1976. The sensitivity and dynamic range of inertial seismographs, *Rev. Geophys. Space Phys.*, v. 14, p. 93-116.

Moore, R. D., Dorman, L., M., Huang, C.-Y., and Berliner, D. L., 1981. An ocean bottom, microprocessor based seismometer, *Mar. Geophys. Researches,* v. 4, p. 451-477.

Okal, E. and J. Talandier, "Dispersion of one-second Rayleigh modes through oceanic sediments following shallow earthquakes in the south-central Pacific Ocean basin," in: Bottom-interacting Ocean Acoustics, ed. by W.A. Kuperman and F.B. Jensen, Plenum Press, 345-358, 1980.

Otnes, R. K., and Enochson, L., 1972. *Digital Time Series Analysis:* New York (John Wiley).

Prentiss, D. D., and Ewing, J. I., 1963. The seismic motion of the deep ocean floor, *Bull. Seismol. Soc. Amer.*, v. 53, p. 765-781.

Prothero, W. A., 1974. Ocean bottom seismometer capsule, *Bull. Seismol. Soc. Amer.*, v. 64, p. 1251-1262.

Rice, S. O., 1944-1945. Mathematical analysis of random noise, Bell Sys. Tech. J., v. 23-24. Also in: Wax, N. (Ed.), 1954. *Selected Papers on Noise and Stochastic Processes:* New York (Dover).

Schneider, W. A., and Backus, M. M., 1964. Ocean bottom seismic measurements off the

California coast, *J. Geophys. Res.,* v. 69, p. 1135-1143.

Schneider, W. A., Farrell, P. J., and Brannian, R. E., 1964. Collection and analysis of Pacifc ocean-bottom seismic data, *Geophysics,* v. 29, p. 745-771.

Stephen, R. A., Louden, K. E., and Matthews, D. H., 1980. The Oblique Seismic Experiment on Deep Sea Drilling Project Leg 52. in: Donnelly et al., *Initial Reports of the Deep Sea Drilling Project,* v.51,52,53: Washington (U. S. Government Printing Office), p. 675-704.

Stephen, R. A., Johnson, S., and Lewis, B., 1981. The Oblique Seismic Experiment on Deep Sea Drilling Project Leg 65. in: *Initial Reports of the Deep Sea Drilling Project,* v. 65: in press.

Stephen, R. A., 1982. The oblique seismic experiment on DSDP Leg 70. in: *Initial Reports of the Deep Sea Drilling Project,* v.70: in press.

Tuthill, J. D., Lewis, B. T. R., and Garmany, J. D., 1981. Stoneley waves, Lopez Island noise, and deep sea noise from 1 to 5 Hz, *Marine Geophys. Researches,* v.5, p. 95-108.

Welch, P. D., 1967. The use of fast Fourier transform for the estimation of power spectra: A method based on time averaging over short, modified periodograms, *IEEE* Trans. Audio Electro-acoust., v. AU-15, p. 70-73.

Appendix I

The noise equation and its transformation in horizontal spatial coordinates are derived here. The result for transformed time variation is well-known and will be stated without proof.

A1.1 The Noise Equation

Denote (x,y,t) by the vector ξ; then the functional dependence of the field variables may be written as $f(\xi)$ and $u(\xi,z)$, for example. Also, the differential element $dxdydt$ will be represented by $d\xi$.

Expand C_{uu} suppressing the z-dependence:

$$C_{uu}(\xi) = <[\int d\xi_1 G(\xi_0-\xi_1)f(\xi_1)][\int d\xi_2 G^T(\xi_0+\xi_1-\xi_2)f(\xi_2)]> \tag{A1.1}$$

$$= \int\int d\xi_1 d\xi_2 G(\xi_0-\xi_1)G^T(\xi_0+\xi_1-\xi_2)<f(\xi_1)f(\xi_2)> \tag{A1.2}$$

Let $\xi_2 = \xi_1+\xi_3$. Then

$$C_{uu}(\xi) = \int\int d\xi_1 d\xi_3 G(\xi_0-\xi_1)G^T(\xi_0+\xi-\xi_1-\xi_3)C_{ff}(\xi_3) \tag{A1.3}$$

Let $\xi_4 = \xi_0-\xi_1$. Then

$$C_{uu}(\xi) = \int d\xi_3 C_{ff}(\xi_3)[\int d\xi_4 G(\xi_4)G^T(\xi_4+\xi-\xi_3)] \tag{A1.4}$$

$$= \int d\xi_3 C_{ff}(\xi_3)\Gamma(\xi-\xi_3) \tag{A1.5}$$

$$= \Gamma(\xi) * C_{ff}(\xi) \tag{A1.6}$$

i.e.

$$C_{uu}(x,y,z,t) = \int\int\int dx_3 dy_3 dt_3 \Gamma(x-x_3,y-y_3,z,t-t_3)C_{ff}(x_3,y_3,t_3) \tag{A1.7}$$

Now, because $f(x,y,t)$ and $G(x,y,z,t)$ are axisymmetric we can write $C_{ff} = C_{ff}(r,t)$ and $\Gamma = \Gamma(r,z,t)$ where $r^2 = x^2+y^2$. Then the above convolution is axisymmetric, that is $C_{uu} = C_{uu}(r,z,t)$. In plane polar coordinates, this convolution takes the form

$$C_{uu}(r,z,t) = \int_{-\infty}^{\infty} dt_o \int_0^{2\pi} d\phi_o \int_0^{\infty} r_o\, dr_o\, \Gamma(|\,r-r_o\,|,z,t-t_o)C_{ff}(r_o,t_o) \tag{A1.8}$$

where $r\cdot r_o = rr_o\cos\phi$.

A1.2 Transformation of the Noise Equation

$C_{uu}(r,z,t)$ can be expressed as the convolution of two functions $\Gamma(r,z,t)$ and $C_{ff}(r,t)$, each of which are autocorrelations. The integral expression for C_{uu} simplifies considerably if we transform it over both time and horizontal distance.

The Fourier transform pair $h(t)$ and $H(\omega)$ is defined as

$$H(\omega) = \int_{-\infty}^{\infty} dt \ e^{i\omega t} h(t) \qquad (A1.9)$$

$$h(t) = \frac{1}{2\pi} \int_{-\infty}^{\infty} d\omega \ e^{-i\omega t} H(\omega) \qquad (A1.10)$$

The convolution of $f(t)$ and $g(t)$ has transform $F(\omega)G(\omega)$; their correlation has transform $F(\omega)G^{\dagger}(\omega)$, where the dagger denotes the complex conjugate.

A similar result holds for the (zeroth order) Bessel transform. Define the transform pair $h(r)$ and $H(k)$ as

$$H(k) = \int_{0}^{\infty} r dr J_o(kr) h(r) \qquad (A1.11)$$

$$h(r) = \int_{0}^{\infty} k dk J_o(kr) d(k) \qquad (A1.12)$$

The convolution $h(r)$ of $f(r)$ and $g(r)$ is:

$$h(r) = \int_{0}^{2\pi} d\phi_0 \int_{0}^{\infty} r_o dr_o f(|\mathbf{r}-\mathbf{r}_o|) g(r_o) \qquad (A1.13)$$

and their cross-correlation $s(r)$ is:

$$s(r): \int_{0}^{2\pi} d\phi_o \int_{0}^{\infty} r_o dr_o \ f(|\mathbf{r}+\mathbf{r}_o|) g(r_o) \qquad (A1.14)$$

The transform of $h(r)$ can be written as

$$H(k) = \frac{1}{2\pi} \int_{0}^{2\pi} d\phi_o \int_{0}^{\infty} r_o dr_o g(r_o) \left[\int_{0}^{2\pi} d\phi \int_{0}^{\infty} r dr e^{i\mathbf{k}\cdot\mathbf{r}} f(|\mathbf{r}-\mathbf{r}_o|) \right] \qquad (A1.15)$$

where the integral representation $J_o(kr) = \frac{1}{2\pi} \int_{0}^{2\pi} e^{i\mathbf{k}\cdot\mathbf{r}} d\phi$ has been used, with $\mathbf{k}$ defined such that $k = |\mathbf{k}|$ and $\mathbf{k}\cdot\mathbf{r} = kr\cos\phi$. Convert the bracketed expression in equation (A1.15) to

Cartesian coordinates, and make the substitution $\mathbf{R} = \mathbf{r} - \mathbf{r}_o$, $R = |\mathbf{R}|$, $X = x - x_o$, $Y = y - y_o$. Then

$$H(k) = \frac{1}{2\pi} \int_0^{2\pi} d\phi_o \int_0^{\infty} r_o \, dr_o \, g(r_o) \left[2\pi \, e^{i\mathbf{k}\cdot\mathbf{r}_o} F(k) \right] \qquad \text{(A1.16)}$$

$$= 2\pi F(k) \left[\frac{1}{2\pi} \int_0^{\infty} r_o \, dr_o \, g(r_o) \int_0^{2\pi} e^{i\mathbf{k}\cdot\mathbf{r}_o} d\phi_o \right] \qquad \text{(A1.17)}$$

$$= 2\pi F(k) G(k) \qquad \text{(A1.18)}$$

Thus, $H(k) = 2\pi F(k) G(k)$.

Proceeding as above, $S(k)$ may be reduced to

$$S(k) = 2\pi F(k) \left[\frac{1}{2\pi} \int_0^{\infty} r_o \, dr_o \, g(r_o) \int_0^{2\pi} e^{-i\mathbf{k}\cdot\mathbf{r}_o} d\phi_o \right] \qquad \text{(A1.19)}$$

But $J_o(kr) = J_o(-kr)$, so

$$S(k) = 2\pi F(k) G(k) = H(k) \qquad \text{(A1.20)}$$

A1.3 The Transformed Noise Equation

Using the results above, we can write

$$\mathbf{C}_{uu}(k,z,\omega) = \mathbf{\Gamma}(k,z,\omega) C_{ff}(k,\omega) \qquad \text{(A1.21)}$$

where

$$(\mathbf{\Gamma}(k,z,\omega))_{ij} = G_i^{\dagger}(k,z,\omega) G_j(k,z,\omega) \qquad \text{(A1.22)}$$

As a specific example, $\Gamma_{zz}(k,z,\omega) = G_z^{\dagger}(k,z,\omega) G_z(k,z,\omega)$, so

$$[\mathbf{C}_{uu}(k,z,\omega)]_{zz} = |G_z(k,z,\omega)|^2 C_{ff} \qquad \text{(A1.23)}$$

Appendix II

In this appendix we model the transient noise observed in the MSS data as a compound, stationary Poisson process (Feller, 1968) and derive an expression for its power spectral density function on the time interval $0 \leqslant t \leqslant T$. We define the process

$$S_N(t) = \sum_{k=1}^{N} X_k(t) \tag{A2.1}$$

where $\{X_k\}$ is a sequence of identically distributed, independent, stochastic variables, and N has a stationary Poisson probability distribution

$$P(N=n) = \frac{e^{-\lambda T}(\lambda T)^n}{n!} \quad . \tag{A2.2}$$

The expected value of N is

$$<N> = \sum_{n=0}^{\infty} n \; P(N=n) \tag{A2.3}$$

$$= \lambda T \quad , \tag{A2.4}$$

so that the constant λ may be interpreted as the mean rate of event occurrence.

The $\{X_k\}$ are assumed to have the form

$$X_k(t) = \alpha_k h(t-t_k) \quad , \tag{A2.5}$$

where h(t) is the transient shape, and $\{\alpha_k\}$ and $\{t_k\}$ are the transient amplitude and occurrence times, respectively. N, $\{\alpha_k\}$, and $\{t_k\}$ are assumed to be mutually independent random variables; in particular, the $\{t_k\}$ are assumed to be uniformly distributed over the time of observation, T.

We wish to find the power spectral density function $P_S(f)$ of $S_N(t)$ at frequency f. P_S is the Fourier transform of the autocovariance function $R_{SS}(\tau)$ of S_N:

$$P_S(f) = 2 \int_{-\infty}^{\infty} R_{SS}(\tau) e^{-i2\pi f \tau} d\tau \quad , \tag{A2.6}$$

$$R_{SS}(\tau) = < (S_N(t) - < S_N(t)>) (S_N(t+\tau) - < S_N(t+\tau)>) > \quad . \quad\quad (A2.7)$$

The factor of 2 in equation (A2.6) is due to our normalization of $P_S(f)$, in which the total power per Nyquist bandwidth is equal to the variance of the time signal (the energy of the negative frequencies is folded into the positive).

Note that since S_N is stationary, $< S_N(t)>$ is independent of t, and equation (A2.7) is equivalent to

$$R_{SS}(\tau) = < S_N(t) S_N(t+\tau)> - < S_N >^2 \quad . \quad\quad (A2.8)$$

We will evaluate the two terms of this equation separately. The mean value of S_N is

$$< S_N > = \sum_{n=0}^{\infty} P(N=n) < \sum_{k=1}^{n} X_k > = \sum_{n=0}^{\infty} P(N=n) n < X_k > \quad . \quad\quad (A2.9)$$

Since N, $\{\alpha_k\}$, and $\{t_k\}$ are mutually independent,

$$< S_k > = < N > < X_k > \quad , \quad\quad (A2.10)$$

where for each X_k,

$$< X_k > = < \alpha_k h(t - t_k)> = < \alpha > \frac{1}{T} \int_0^T h(t - t_k) dt_k \quad\quad (A2.11)$$

where we have used the assumption that the $\{\alpha_k\}$ are identically distributed and therefore have the same mean $< \alpha >$. We assume that the interval of observation T is much larger than the transient duration, so that, approximately,

$$< X_k > = < \alpha > \frac{1}{T} \int_0^{\infty} h(t) dt \equiv < X > \quad\quad (A2.12)$$

and thus, using equation (A2.4),

$$< S_N > = \lambda < \alpha > \int_0^{\infty} h(t) dt \equiv < S > \quad . \quad\quad (A2.13)$$

We now consider the bivariate moment in equation A8:

$$< S_N(t)S_N(t+\tau)> \; = \; \sum_{n=0}^{\infty} P(N=n) < \sum_{k=1}^{n} X_k(t) \sum_{m=1}^{n} X_m(t+\tau)> \qquad . \qquad (A2.14)$$

The mutual independence of the $\{X_k\}$ implies

$$< \sum_{k=1}^{n} X_k(t) \sum_{m=1}^{n} X_m(t-\tau)> \; = \; n < X_k(t)X_k(t+\tau)> \; + \; n(n-1)< X>^2 \qquad . \qquad (A2.15)$$

The bivariate moment of X_k at lag τ is

$$< X_k(t)X_k(t+\tau)> \; = \; < (\alpha_k h(t-t_k))(\alpha_k h(t-t_k+\tau))> \qquad (A2.16)$$

$$= \; < \alpha^2> \; \frac{1}{T} \int_{t_k}^{T} h(t')h(t'+\tau)dt' \qquad (A2.17)$$

$$\approx \; < \alpha^2> \; \frac{1}{T} \; h \; * \; h(\tau) \qquad (A2.18)$$

where ' $*$ ' denotes cross-correlation. Collecting these results,

$$< S_N(t)S_N(t+\tau)> \; = \; < N> < \alpha^2> \; \frac{1}{T} \; h \; * \; h(\tau) \; + \; < N(N-1)> < X>^2 \qquad . \qquad (A2.19)$$

From equation A2 we find that

$$< N(N-1)> \; = \; (\lambda T)^2 \qquad . \qquad (A2.20)$$

Thus, from equations A12 and A13,

$$< S_N(t)S_N(t+\tau)> \; = \; \lambda < \alpha^2> \; h \; * \; h(\tau) \; + \; < S>^2 \qquad , \qquad (A2.21)$$

so, finally,

$$R_{SS}(\tau) \; = \; \lambda < \alpha^2> \; h \; * \; h(\tau) \qquad . \qquad (A2.22)$$

It is now a simple matter to determine $P_S(f)$ using equations A7 and A22. A well-known result from Fourier analysis (Bracewell, 1965) is that

$$\int_0^\infty h * h(\tau) e^{-i2\pi f \tau} d\tau = |H(f)|^2 \quad . \tag{A2.23}$$

where H(f) is the Fourier transform of h(t). Hence,

$$P_S(f) = 2\lambda <\alpha^2> |H(f)|^2 \quad . \tag{A2.24}$$